Surface compositions of clean materials for solid oxide electrochemical cells

Andersen, Thomas

Publication date:
2011

Document Version
Publisher's PDF, also known as Version of record

Surface compositions of clean materials for solid oxide electrochemical cells

Ph.D. Dissertation

by

Thomas Andersen

Center for Individual Nanoparticle Functionality

Technical University of Denmark

January 2011

Preface

This thesis is submitted in partial fulfillment of the requirements for obtaining the Ph.D. degree from the Technical University of Denmark (DTU). The presented work has been carried out from 1st of November, 2007 to the 31st of January, 2011 at the Center for Individual Nanoparticle Functionality (CINF), Department of Physics, DTU, and the Fuel Cells and Solid State Chemistry Division, Risø National Laboratory for Sustainable Energy, DTU, under the supervision of Professor Ib Chorkendorff, CINF, Research Professor Mogens Bjerg Mogensen, Risø DTU, and Senior Scientist Karin Vels Hansen, Risø DTU. Financial support by the Programme Commission on Sustainable Energy and Environment, The Danish Council for Strategic Research, via the SERC project, contract no. 2104-06-0011 is greatfully acknowledged.

First of all I would like to thank my supervisors for many fruitful discussions, being patient with me and always answering questions no matter how trivial they were. Ib has has been an encouraging supervisor and has always had an open door policy for both small and large problems when UHV science was uphill work. His extensive knowledge of surface science and UHV has been of great value to me. I would also like to thank Mogens for sharing his experience in the field of solid state chemistry and electrochemistry. His ideas and large insight into solid oxide cell components is gratefully acknowledged. I thank Karin for her encouragement and enabling me to keep the perspective.

I would also like to thank the mechanics at the institute work shop Dan and Peter for helping me rebuild the UHV setup. Without their ideas and

know-how the project would not have come far.

A thank also goes to John Larsen for this time helping me learn the setup when I was totally new to UHV. His help and experience with UHV is greatly appreciated.

Working daily at CINF as a Ph.D. student has been a great time for me. Everyone has contributed to a good working environment whether this was coffee time, office smalltalk or discussion of practical problems regarding scientific issues.

Last but not least I would like to thank my girlfriend Kristine Lund Knudsen for her support and encouragement during my time as a Ph.D. student to keep my spirits high when things looked the darkest.

Thomas Andersen
Kgs. Lyngby, January, 2011

Abstract

This thesis presents the results obtained in the efforts to remove trace bulk impurities i yttria stabilized zirconia (YSZ). A segregation study, two different cleaning methods and electrochemistry on the Ni/YSZ interface are presented.

YSZ single crystals are annealed in a furnace at 1100 °C for 10 hours and subsequently studied by Angle Resolved X-ray Photoelectron Spectroscopy (ARXPS). The surfaces of the YSZ crystals are enriched with silicon after annealing. The silicon content on the surface increases in the temperature range of 500–1100 °C.

A strontium zirconate getter is applied to the surface of YSZ single crystals. The crystals with powder applied are heat treated at 1450 °C in 0.15 atm water vapor. After heat treatment regularly distributed ball-sectioned features are observed on the surface by atomic force microscopy (AFM) and scanning electron microscopy (SEM). A mean height of 522 nm and a mean diameter of 6.9 μm is found from the AFM images. The features are shown to contain 10–12 at.% of silicon and aluminium by energy-dispersive X-ray spectroscopy (EDX). From transmission electron microscopy (TEM) images the features are shown to be confined to the surface of the YSZ crystals.

YSZ single crystals are annealed in UHV. An experimental setup where heating of the YSZ crystal can be applied has been designed and build. The heating of the crystal is achieved by an applied a.c. voltage using the ionic conductivity of YSZ. After annealing at 1100 °C for 10 hours in UHV no silicon enrichment is observed on the surface of the YSZ single crystal. Only in partial pressures of oxygen (>25 mbar) or water vapor (10 mbar) silicon

enrichment is observed. The silicon free surfaces after annealing under UHV conditions or low partial pressures of oxygen or water vapor are attributed to the electrochemical reduction of silicon dioxide on the surface of the crystal. The silicon dioxide decomposition on the surface of the crystal and subsequent desorption from the crystal is shown by silicon enrichment of a gold foil placed behind the YSZ single crystal while annealed. The volatile silicon species from the decomposition on the YSZ surface is adsorbed on the gold foil which acts as a cold finger compared to the hot YSZ single crystal.

Electrochemical impedance spectroscopy (EIS) at 850 °C in a wet hydrogen atmosphere (3% H_2O/H_2) measured on two single crystals after vacuum annealing is compared to two reference crystals. The vacuum annealed samples have a lower polarization resistance compared to the polarization resistance for the reference crystals at the experiment end. From XPS mapping by a focused X-ray source on reference and vacuum annealed crystals after electrochemical experiment silicon is found on all electrolyte surfaces. The findings suggest that the cleaning time by vacuum annealing has been to short to remove all silicon from the YSZ crystals but suggests a positive effect of the vacuum annealing.

Resumé

Denne afhandling præsenterer resultaterne i bestræbelserne på at fjerne urenheder i yttria-stabiliseret zirconia (YSZ). Et segregeringstudie, to forskellige rensningsmetoder og elektrokemiforsøg på Ni/YSZ-grænsefladen vil blive præsenteret.

YSZ-enkeltkrystaller er blevet udglødet i en ovn ved 1100 °C i 10 timer og efterfølgende karakteriseret ved vinkelopløst røntgen fotoelektron spektroskopi (ARXPS). Overfladen af YSZ-krystallerne er beriget med silicium efter udglødningen. Silicium-mængden påoverfladen er stigende med udglødningstemperaturer fra 500–1100 °C.

Strontium zirconat blev påført overfladen af YSZ-enkeltkrystaller. Krystallerne med pulver på overfladen blev varmebehandlet ved 1450 °C i 0.15 atm vanddamp. Efter varmebehandlingen blev homogent fordelte kuglekalotter observeret på overfladen ved hjælp af atomar kraftmikroskopi (AFM) og sekundær elektronmiskroskopi (SEM). En middelhøjde på 522 nm og en middeldiameter på 6.9 μm blev fundet fra AFM-billederne. Kuglekalotterne indeholdt 10–12 at.% silicium og alumiminium som er blevet bestemt af energydispersivt røntgenspektroskopi (EDX). Fra transmissionselektronmikroskopi (TEM) blev kuglekalotterne vist til at befinde sig på den yderste overflade af YSZ-krystallerne.

YSZ-enkeltkrystaller blev varmebehandlet i ultra højt vakuum (UHV). En eksperimentel opstilling, hvor YSZ-krystaller kunne opvarmes er blevet designet og bygget. Opvarmningen af krystallerne foretages via en påført vekselspænding, der anvender ionledningen i YSZ. Efter udglødning ved 1100 °C i 10 timer i UHV blev silicium ikke observeret på overfladen af YSZ enkeltkrys-

tallerne. Kun i høje partialtryk af ilt ($\geq$25 mbar) eller vanddamp ($\geq$10 mbar) blev silicium observeret på overfladen af YSZ-krystallerne. De silicium-frie overflader efter udglødning under UHV-forhold eller i lave tryk af ilt eller vanddamp blev forklaret med en elektrokemisk reduktion af silicium dioxid på overfladen af krystallen. Silicium dioxid-dekomponeringen på overfladen af YSZ-krystallen blev vist ved silicium-berigelse af et guldfolie placeret bag ved krystallen, mens den blev udglødet. De flygtige silicium-arter fra dekomponeringen på YSZ-overfladen er adsorberet på guldfoliet, der virker som en fælde for silicium-arterne i forhold til det varme YSZ krystal.

Elektrokemisk impedansspektroskopi ved 850 °C i våd brint (3% H_2O/H_2) blev målt på to enkeltkrystaller efter vakuumudglødning og sammenlignet med to referencekrystaller. De vakuumudglødede krystaller havde lavere polarisationsmodstand sammenlignet med referencekrystallerne ved eksperimentets afslutning. Ved hjælp af XPS med en fokuseret røntgenkilde blev silicium fundet på både referencekrystallerne og de vakuumudglødede krystaller. Resultaterne foreslår, at rensningstiden ved vakuumudglødning af krystallerne har været for kort til at fjerne al siliciumen fra YSZ-krystallerne, men at der er en positiv effekt af vakuumrensningen.

Contents

Chapter 1

Introduction

The world's current population is just below 7 billion people. With an estimated growth of 1 % per annum the worlds population will reach 7.6 billion in year 2020. The growth of not only population on the Earth but also the rapid industrial progress made by developing countries is reflected in the increasing energy demand of the world. From 1980 to 2006 the power consumption increased from 9.5 TW to 15.8 TW [1]. In 2006, 86 % of this energy was produced by oil, gas or coal. The large increase in energy demand and the associated increase in the use of carbon containing fuels have resulted in an increase in carbon dioxide emissions into the atmosphere [2]. Using alternative energy sources such as solar energy or wind power has during later years attracted greater interest not only due to environmental concerns but also due to the finite supply of fossil fuels.

Future energy supplies should be inherently clean, efficient and with renewable energy sources. However, the two major carbon-free energy sources of wind and solar are not constantly available with time. A need for storage of energy and subsequent consumption when the energy is needed is necessary. Once the the solar energy or wind power has been stored in chemical fuels a fuel cell, discovered in 1839 by Sir William Grove [3], can be used to convert the energy in chemical bonds in the fuel directly into electricity.

The solid oxide cell (SOC) is one of the technologies that can be run both as a Solid Oxide Electrolyzer Cell (SOEC) producing chemical fuels by

electricity and as a Solid Oxide Fuel Cell (SOFC) where the supplied fuel is oxidized producing electricity. SOCs can hence be used to store energy when it is available and subsequently produce energy when needed.

1.1 Solid oxide fuel cells

SOFCs is one of the promising technologies for creating a low (potentially zero) carbon dioxide emission society. The cell is characterized by the use of a solid oxide as electrolyte and operating temperatures above 500 °C. This is in contrast to the other intensively studied Proton Exchange Membrane Fuel Cell (PEMFC) or Direct Methanol Fuel Cell (DMFC) which conducts protons through a polymer electrolyte membrane and operates at temperatures between 50–100 °C.

SOFCs have a number of attractive advantages compared to other fuel cell types. The cell is CO tolerant, which is an advantage with the current hydrogen production route. Hydrogen is typically produced by steam reforming of natural gas to syngas which is subsequently water gas shifted to produce more hydrogen [4]. Hydrogen will hence typically contain small amounts of CO orginating from the syngas. SOFCs have no need for water management and the components are all solid state giving large stability.

Unlike many other fuel cells SOFCs can have multiple geometries. Currently the planar fuel cell design and the tubular design are the most prominent. The planar design has the advantage compared to tubular cells of a wider range of manufacturing processes giving larger control of parameters of optimization. Also, the the planar design is more compact yielding higher obtainable power densities. The tubular design, on the other hand, has the advantage of smaller induced stresses during startup and shutdown of the cell giving larger robustness.

1.1.1 Solid oxide fuel cell principle of operation

A single SOFC consists of mainly three components. The anode, electrolyte and cathode. During operation oxygen is reduced at the cathode to oxygen

ions. These ions are then conducted to the anode side of the SOFC through the electrolyte and used as an oxidant. The electrolyte ensures not only oxygen ion transport from cathode to anode but also serves as electrical insulation between the two sides of the cell.

Considering the Gibbs free energy the resulting voltage difference across a cell can be calculated

$$\Delta G + nF\varepsilon = 0 \tag{1.1}$$

where ΔG is the Gibbs free energy of the reaction, n is the number of electrons (4), F is the Faradaic constant (96485.3 C/mol) and ε is the voltage at open circuit voltage (OCV). Calculating the voltage at OCV typically gives a value around 1 V. This means for large power applications the cells will need to be serially connected known as stacking.

The main advantages of the fuel cells is the direct conversion of energy stored in chemical bonds to electricity. The fuel cells are hence not limited by the Carnot cycle and has theoretical efficiency of 60 % which can be increased to 80 % using the waste heat. Also, SOFCs have a modular build meaning constant price per kW installed and equivalent efficiency and low noise level.

1.2 Solid oxide fuel cell materials

SOFCs are composed of primarily three components; an anode, an electrolyte and a cathode. Additionally, for large power applications an interconnect between cells is used for stacking several cells obtaining larger total power output.

1.2.1 Anode

The anode layer must be porous to allow for flow of fuel and product gas in and out of the cell. Furthermore, the anode must both be electronically and ionically conductive to contact external circuits and supply oxygen ions for oxidation of the fuel. The material most often employed is a cermet of nickel and yttrium oxide (yttria) stabilized zirconium oxide (zirconia) (YSZ). Nickel is used as a catalyst for the dissociation of fuel at the elevated operating

temperatures of SOFCs due to its low price and good catalytic properties at SOFC conditions as shown in a recent theoretical paper [5]. The nickel also provides an electrical contact to the outer circuit while YSZ acts both as a backbone supporting the nickel particles keeping them from agglomerating and providing oxygen ions to the reaction sites.

Preparation of the anode is usually done by mixing NiO and YSZ in a predetermined ratio. When the anode is exposed to reducing conditions the NiO is reduced to metallic nickel which serves as percolation path of the electrons from the fuel oxidation. Porosity in the anode is obtained by the volume decrease associated with NiO to Ni reduction which is on the order of 40 % [6]. The large volume expansion or decrease during reduction or oxidation, respectively, also introduces stresses in the anode which can ultimately break the cell.

1.2.2 Electrolyte

The most commonly used electrolyte in SOFCs is YSZ. Zirconia has a monoclinic crystal structure at room temperature which transforms to tetragonal and cubic structures at higher temperatures. To stabilize zirconia in the cubic structure at room temperature and improve the ionic conductivity the oxide is often doped with different trivalent oxides. Typically yttria is chosen in the case of SOFC applications. YSZ has excellent mechanical and chemical stability at SOFC operating temperatures making it the most widely used electrolyte in SOFCs [7, 8].

1.2.3 Cathode

In the air electrode, or cathode, oxygen molecules are dissociated to oxygen ions. Strontium doped Lanthanum Manganite (LSM) mixed with YSZ is commonly used for high temperature applications while Lanthanum Strontium Cobaltite Ferrite (LSCF) which is a mixed ionic and electronic conductor is used for low temperature applications.

1.2.4 Interconnect

To obtain larger voltages and hence generate more power SOFCs are often employed as a stack, i.e. coupled in series. The interconnect, used to separate on each other following cathode and anode, is exposed to both oxidizing and reducing atmospheres at high temperatures which places demands on the stability of the material used. Typically, doped lanthanum chromites or a 95Cr-5Fe alloy is used.

1.3 The anode/electrolyte interface

The anode/electrolyte interface is of great importance to oxidation of the fuel (eg. hydrogen) into electrons and byproduct. In the case of SOFCs using hydrogen as a fuel, nickel is used to dissociate the hydrogen molecule which subsequently recombines with the oxygen ions diffused through the electrolyte to form water and electrons. The overall reaction can be described as

$$H_2 + O^{2-} \rightarrow H_2O + 2e^- \tag{1.2}$$

where the electrons are driven through an outer circuit to perform work.

It is evident that the performance of the anode/electrolyte interface is dependent on the amount of sites where porosity, electronic conductive catalyst and ion-conducting electrolyte meet, i.e. oxygen ions from the ion conductive material is present, fuel and product gas can diffuse due to porosity in the anode and electrons can be transported to the external circuit. This boundary, known as the triple phase boundary (TPB), is defined as areas where porosity, fuel dissociation catalyst and ion-conduction electrolyte meet.

1.4 Bulk impurities in yttria stabilized zirconia

The anode/electrolyte of a SOFC is highly complex. Performance of the anode depends on several things including properties of the constituent phases, porosity, percolation of the network etc. Within the last decade is has been found that the best SOFC anodes have unexpectedly high overpotentials

[9, 10]. Experiments indicate that impurities segregated from the YSZ bulk to the surface and hence the TPB at elevated temperatures may be the cause of this [11–15]. Consequently, investigators have found segregation of impurities from the bulk YSZ to the surface when using the appropriate tools to look for them including X-ray Photoelectron Spectroscopy (XPS) [16, 17], Low-Energy Ion Scattering (LEIS) [18], Time-of-Flight Secondary Ion Mass Spectrometry (TOF-SIMS) [19] and electron microscopy [20, 21].

Bulk impurities, such as silicon dioxide (silica) and aluminium oxide (alumina), typically found in ppm levels in the raw YSZ materials commercially available, have a high tendency to segregate to the external surface of YSZ at elevated temperatures. The segregated impurities change the external surface composition of the electrolyte at elevated temperatures. Reactions occurring at the TPB is hence through a poorly conductive foreign phase consisting of impurities segregated from the bulk YSZ electrolyte.

The driving force of bulk to surface segregation of impurities in YSZ is believed to be due to the high free surface energy of the unrelaxed YSZ surface. The mechanical energy release rate by fast fracture of YSZ, which is believed to be equal to the free surface energy [10], for 8YSZ (8 mol% Y_2O_3 in ZrO_2) has been determined to 3–4 J/m^2 [22, 23]. The high surface free energy of YSZ gives a large driving force for impurities in the bulk material to saturate dangling bonds at the surface hence lowering the surface free energy.

The trace bulk impurities in YSZ can be traced back to the starting raw materials used to produce YSZ. Zirconium is found in nature as different minerals. Zircon ($ZrSiO_4$) is by far the most important source of zirconium and is typically the starting material from which high purity zirconium metals are refined. Baddeleyite, ZrO_2, is another source of zirconium. Typically baddeleyite contains large amounts of hafnium impurities. Zirconium may also be found in zirconolite ($CaZrTi_2O_7$) but is, however, less common than zircon and baddeleyite. Common for all the sources of zirconium is the content of small amounts of impurities in the starting material.

The bulk impurities in YSZ segregates to the surface at high temperatures block the TPB boundary as illustrated in Figure 1.1. In the presence of the

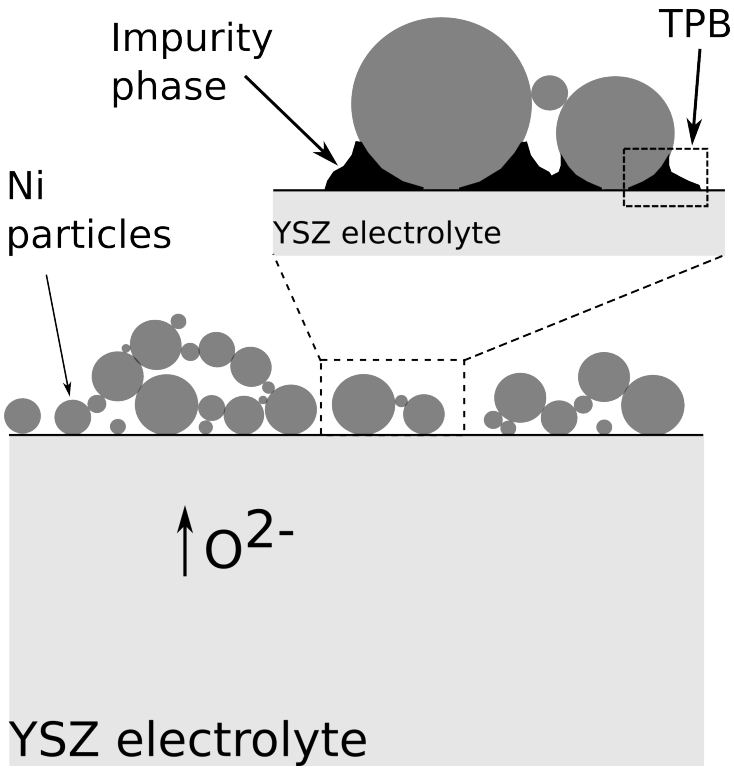

Figure 1.1: Illustration of a simplified anode/electrolyte interface after annealing at high temperatures. The segregated impurities from the YSZ bulk form a layer blocking the TPB through or around which reactions would have to occur.

impurity phase, formed after segregation of impurities from the YSZ bulk, it is clear that the electrochemical reactions involved in the oxidation of the supplied fuel would have occur either through the impurity phase or around it. The mobility of different species on or in the impurity phase is not known but is, however, expected to be very different from that of a clean YSZ interface.

1.5 Dissertation objective

The main purpose of this thesis is to study the surface composition of YSZ single crystals and clean them from typical segregating impurities. The YSZ

crystals will after cleaning procedures be characterized and compared to reference crystals by Electrochemical Impedance Spectroscopy (EIS).

1.6 Dissertation overview

Following the introduction the main experimental equipment is presented in Chapter 2. The bulk analysis of the YSZ crystals and the segregation of impurities in single crystal YSZ have been studied by annealing in atmospheric air. The results from the glow discharge mass spectrometry (GDMS) bulk analysis and the surface composition after annealing determined by XPS is presented in Chapter 3. The first of two cleaning studies namely using strontium zirconate is presented in Chapter 4. Here YSZ single crystals were annealed with strontium zirconate powder at high temperatures for prolonged periods of time. The second cleaning approach uses annealing of YSZ single crystals in Ultra High Vacuum (UHV). Here a new heating method of YSZ crystals was developed along with an UHV setup for treatment of the crystals. The results from the annealing under controlled atmosphere and pressure is presented in Chapter 5. Finally, in Chapter 6, results from electrochemical measurements of the Ni/YSZ interface is presented.

Chapter 2

Experimental setup and methods

This chapter describes the primary experimental setups which have been used during the project. High temperature treatments (>1400 °C) in furnaces and electrochemical impedance spectroscopy were performed at the Fuel Cells and Solid State Chemistry Division, Risø DTU while surface characterization and annealing of YSZ single crystals under controlled atmosphere and pressure were performed at Center for Individual Nanoparticle Functionality (CINF), DTU. Microscopy were performed at Center for Electron Nanoscopy (CEN), DTU.

2.1 Ultra high vacuum setup

Most surface science studies have been performed in the UHV chamber depicted in Figure 2.1. The setup consists of an analysis chamber, a fast-entry lock and a preparation chamber.

For surface science studies both XPS and Auger Electron Spectroscopy (AES) are available in the analysis chamber which has a base pressure below $2{\cdot}10^{-10}$ mbar as measured by an ionization gauge. The chamber is pumped by an ion pump and a turbomolecular pump. In daily use the chamber is only pumped by the ion pump as the turbomolecular pump is used to pump the fast-entry lock. A titanium sublimation pump is also fitted on the chamber which is used with regular intervals. The fast-entry lock allows for quick

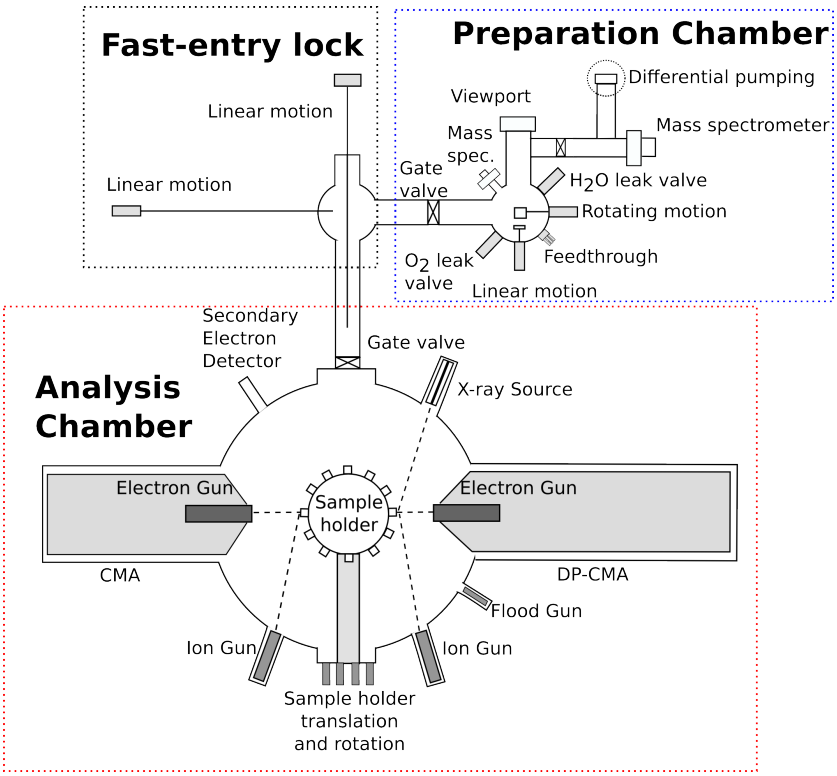

Figure 2.1: Schematic topview of the UHV chamber. Samples are pumped to vacuum in the fast-entry lock. The two perpendicular linear motions on the fast-entry lock allow for transportation of the sample between the analysis chamber and the preparation chamber without exposing the sample to air.

shuffling of samples in and out of the analysis and preparation chamber. When new samples are introduced the fast-entry lock is vented by nitrogen gas. The fast-entry lock is pumped by a turbomolecular pump backed by a roughing pump to achieve vacuum.

Samples are mounted on special designed sample holders which are compatible with the linear motions used for moving samples in vacuum. With the current setup two samples can be inserted simultaneously into the fast-entry lock giving large flexibility. From the fast-entry lock the sample can either be parked in the analysis chamber for surface analysis (XPS or AES) or in the preparation chamber depending on experiment.

The separation of preparation chamber, analysis chamber and fast-entry

lock by gate valves also allows for treatment of a sample in the preparation chamber while analyzing with XPS or AES on a different sample in the analysis chamber.

2.1.1 Analysis chamber

The analysis chamber is fitted with two Cylindrical Mirror Analyzers (CMA). For AES analysis a single pass CMA (PHI 25-110) is used while for XPS analysis a double-pass CMA (DP-CMA) (PHI 25-260AR) is used. Both analyzers are controlled by a PHI 20-805 controller. The X-Ray gun on the chamber is fitted with a magnesium and aluminium dual anode (PHI 04-500) and is controlled by a PHI 32-095 controller. With the current setup the analysis area is determined by geometry of the chamber and is approximately 5x5 mm^2. Electron emission from the two electron guns in separate ends of the chamber used for either imaging for orientation on the samples or excitation of core electrons for spectroscopies are performed by a lanthanum hexaboride crystal or a tungsten filament. The chamber is furthermore fitted with two identical ion guns (PHI 04-303A) for cleaning purposes. Both of these are controlled by PHI 11-065 controllers and are feed with scientific quality argon gas through separate leak valves. When sputtering is performed the ion guns are differentially pumped by a turbomolecular pump. A flood gun has also been installed near the DP-CMA to compensate for charging effects of non-conducting samples during X-ray exposure.

2.1.2 Preparation chamber

The cube, which makes up the main part of the preparation chamber (top right corner of Figure 2.1) is pumped by two turbomolecular pumps. One turbomolecular pump is used for direct pumping on the cube while the other is used for differential pumping of a mass spectrometer also fitted on the preparation chamber. The base pressure of the cube is $4{\cdot}10^{-10}$ mbar as measured by an ionization gauge. By closing the gate valves above the turbomolecular pumps the cube can be sealed off pumping. This can be done to reach high

pressures (up to 1000 mbar) by backfilling the chamber with gas. After high pressure experiments the cube is pumped by a roughing pump until the gate valves to the turbomolecular pumps can opened.

The preparation chamber is fitted with a rotating drive on a side flange such that the sample fixed in the sample holder can be rotated around the center point of the cube. Electrical contacts to the sample in the preparation chamber are provided through both ends of the ceramic sample stage connected by wires to a feedthrough, cf. Figure 2.2 and 2.3. This allows for biasing of the sample compared to chamber ground.

The preparation chamber is equipped with two gas lines connected directly to the cube of the preparation chamber. A scientific grade oxygen bottle is connected to the cube by a leak valve. Millipore water vapor is supplied from a water reservoir held at room temperature through a leak valve. The pressure of oxygen and water in the preparation chamber is monitored by the total pressure in the system as measured by an ionization gauge or a Baratron capacitor gauge depending on pressure range.

2.1.2.1 Mass spectrometers in the preparation chamber

Mass spectrometers can be used to measure the ratio of mass-to-electric charge (m/q) of a molecule or atom. The molecules or atoms are upon entry in the mass spectrometer ionized by electrons released by a hot filament. The now charged molecules or atoms are then separated according to their mass-to-electric charge by a quadrupole mass filter. The signal is finally amplified by a secondary electron multiplier (SEM) by approximately a factor of 10^6 and subsequently recorded.

Two Balzers QMA 125 is fitted on the preparation chamber. Both mass spectrometers are equipped with cross beam ionization sources[1].

The mass spectrometer on a side flange to the cube (global mass spectrometer) shown in the top right corner of Figure 2.1 is used to monitor the gas composition in the preparation chamber. On the top flange of the cube

[1]Cross beam as compared to axial in this context refers to the geometrical placement of filament compared to the longitudinal axis of the mass filter

another Balzers QMA 125 mass spectrometer (local mass spectrometer) is mounted.

The mass spectrometers are connected to respective Balzers QME 125 electronics which are interfaced to PC with homebuilt electronics. Software for control of the mass spectrometers is implemented in LabView.

2.1.3 Sample holders and interfaces

Integrating the preparation chamber with the analysis chamber, fast-entry lock and the sample handling system was a cumbersome task. The idea was to use the fast-entry lock as an intermediate placeholder between the parking stations in the preparation chamber and analysis chamber, respectively. To transfer the sample from the preparation chamber to the analysis chamber two perpendicular linear motions was necessary as seen in Figure 2.1. The

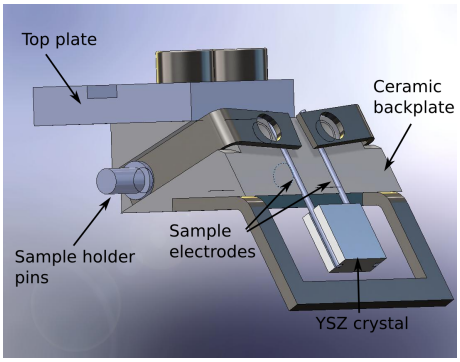

Figure 2.2: A redesigned sample holder. The YSZ crystal is hanging freely in two electrodes which provide electrical contact to the sample and sample holder pins. A ceramic based backplate sample holder is used to avoid short-circuiting the sample.

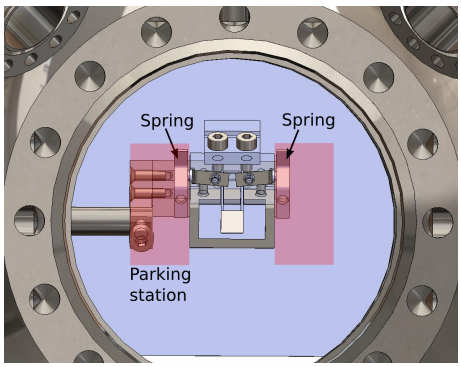

Figure 2.3: A sample parked in the preparation chamber's ceramic sample holder (top view). Electrical contacts to the feedthrough are made via two molybdenum springs which presses against two pins of the sample holder.

original sample holders of metal compatible with the carousel in the analysis chamber had to be redesigned. This was necessary to be able to bias the

electrodes on the YSZ single crystals compared to chamber ground. A sample holder were the crystal is held by two electrodes fixed to a ceramic back plate was designed which fitted the purpose. An illustration of the sample holder is shown in Figure 2.2 while the sample holder in the preparation chamber parking station is shown in Figure 2.3.

For transportation of the sample holder between the different compartments of the UHV setup a linear motion with a custom designed end is used to grip the sample holder's top plate. When opening the gate valve between fast-entry lock and preparation chamber the sample can be moved forth and back between the two chambers. The sample holder with sample mounted is parked in the ceramic socket by rotating the socket and retracting the linear drive. Electrical contact is provided by two molybdenum springs pressed against the pins on each side of the sample holder pins as shown in Figure 2.3. The springs both ensure electrical contact to the sample and fixes the sample holder in the socket such that a 360° rotation around the center axis of the cube is possible.

The design had be be redesigned somewhat during initial testing as sample holders was dropped during rotation in the cube. This was due to the permanent deformation of the springs when delivering or retracting a sample from the parking station in the preparation chamber. The deformation meant the springs were not able to apply enough force on the sample holders' two pins resulting in samples being dropped in the chamber. This was fixed by mounting two additional springs on the backside of the ceramic parking station in the chamber. These springs ensured that the sample holder could not fall out the holder avoiding dropped samples in the chamber. This, however, meant that the rotation of the sample was restricted to 180°.

2.1.4 Heating and temperature measurements in the preparation chamber

Segregation of impurities in YSZ is typically observed at elevated temperatures. It is of course imperative to find the most suitable heating technique for heating the YSZ single crystals in the preparation chamber. For im-

plementation in UHV a local heating method of only the YSZ crystal and not the entire chamber capable of heating the crystal to or above 1100 °C is desireable. YSZ cannot be heated by simple ohmic heating as it is an electrical insulator. Laser heating of the crystal is also difficult due to the low absorption of photons with wavelength from 0.4 μm to 6 μm [24, 25].

It was attempted to heat the crystal by a current loop of platinum wire around the crystal. A platinum wire was inserted into grooves made on three sides of the crystal effectively creating a current loop around the crystal. Heating of the crystal was then achieved by the ohmic heating of the platinum wires and subsequent transfer from the hot wire to the crystal. It was found, however, after experiments in atmospheric air and UHV that high enough temperatures could not be reached before the platinum electrodes melted.

Instead of using a current loop around the crystal it was decided to utilize the ionic conductivity of YSZ. By applying an alternating electric field across the crystal the oxygen ions in the crystal is set into motion with the applied frequency. A tone generator (Topward Function Generator 8102) was used to generate a 18 kHz tone which was amplified by a standard HiFi amplifier (LD Systems PA1000). The frequency of 18 kHz signal was determined by the upper limit of the amplifier used in the setup.

For the heating to work, a sufficiently high ionic conductivity of YSZ is required. The ionic conducitivity of YSZ at room temperature is very low [26–28]. To obtain an appreciable ionic conductivity and start the heating the YSZ single crystal was preheated by a Philips 6958/10H 250 W halogen lamp operated at 10 A and 22 V which was moved to a distance of 1 mm from the YSZ sample surface by a linear drive on the preparation chamber. While heating the crystal by the halogen lamp the a.c. voltage across the crystal was increased slowly from 0 V_{rms} to approximately 15 V_{rms} as measured by a Tektronix 2012B oscilloscope. While the voltage was ramped the current through the crystal increased from 0 A_{rms} at room temperature to approximately 1 A_{rms} at 1100 °C. When the current through the crystal exceeded 0.3 A_{rms} the halogen lamp was turned off and retracted using the linear drive. Heating by a.c. voltage allowed for control of temperature by the supplied voltage and the heating could be sustained for several days. An image of a

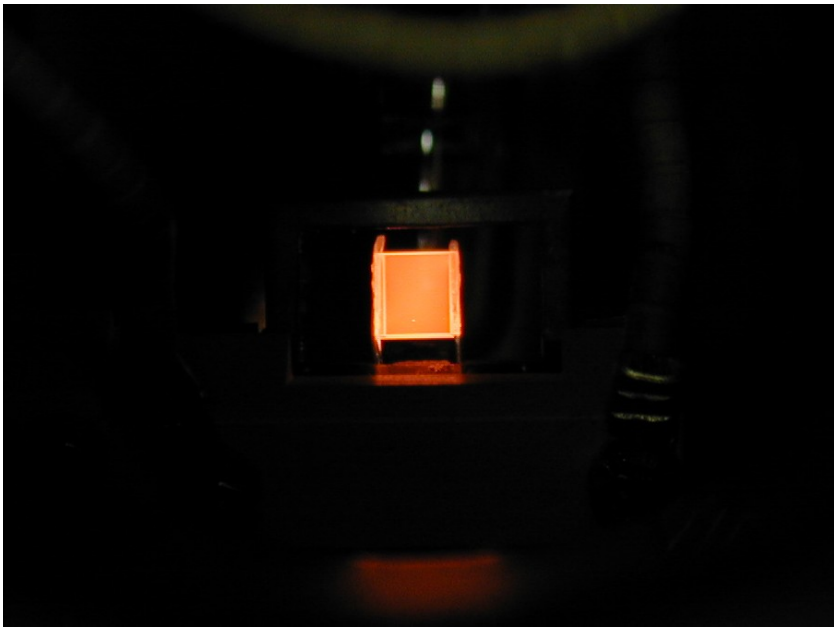

Figure 2.4: A YSZ crystal mounted in the sample holder heated by the applied a.c. voltage in the preparation chamber. The two platinum electrodes can be seen on each side of the crystal.

hot YSZ single crystal can be seen in Figure 2.4.

A schematic showing the heating setup is shown in Figure 2.5. A variable resistor is inserted in series with the crystal to avoid current runaway of the crystal while initiating heating. The shunt resistor (0.1 Ω) in series with the crystal is used to measure the current flow through the circuit.

The ionic conductivity of YSZ is exponentially dependent on temperature [27, 28]. This strong dependence of the ionic conductivity on temperature can be used to make an indirect measurement of the crystal temperature. However, the ionic conductivity varies with the yttria dopant concentration with maximum ionic conductivity around 8 mol% yttria in zirconia [29]. Since the doping concentration of the crystals is not exactly known from the manufacturer the conductivity had to be measured for the used crystals. In this case a single representative crystal was measured.

To mimic the heating setup a crystal is painted with platinum paste on two opposite sides of the crystal. A three-electrode setup was used where

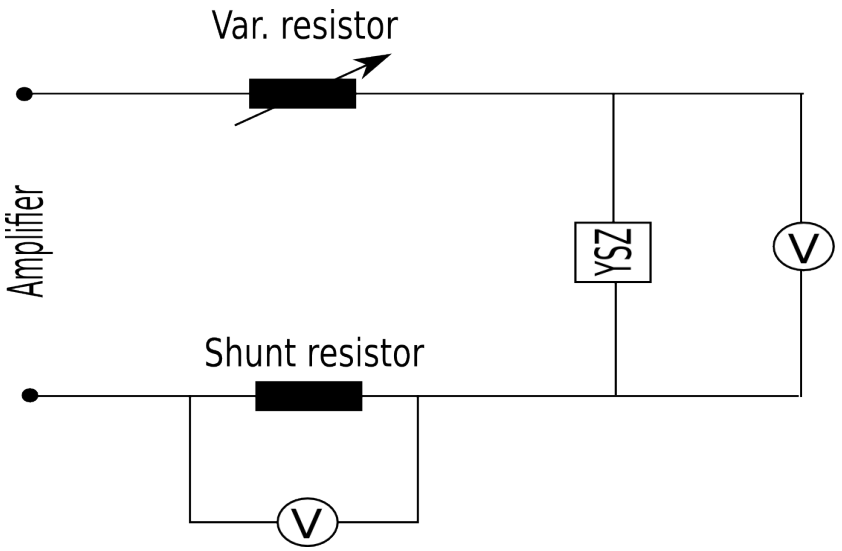

Figure 2.5: Schematic of electrical setup for heating a YSZ single crystal. A variable resistor in series with the crystal is used to avoid current runaway while initiating heating. The shunt resistor is used to measure the current flow through the circuit.

the platinum painted sides are the working and counter electrode. A third platinum wire is positioned on the sample as a reference electrode. The three-electrode setup is inserted into a furnace allowing heating of the entire system. The temperature range in which the ionic conductivity can be measured is determined by the maximum temperature of the furnace and a lower temperature limit determined by apparatus limitations for high resistance measurements. With the furnace used in this experiment the upper temperature limit was 925 °C.

The measurements of the ohmic resistance at 32 MHz at all recorded temperatures is plotted in Figure 2.6.

Figure 2.6 can be used as an indirect measure of the YSZ crystal temperature. By measuring the voltage across and current driven through the sample while heating using a.c. voltage, the ohmic resistance of the crystal can be calculated and the temperature of the crystal can be determined using Figure 2.6.

To verify the temperature estimated from the ohmic resistance of the

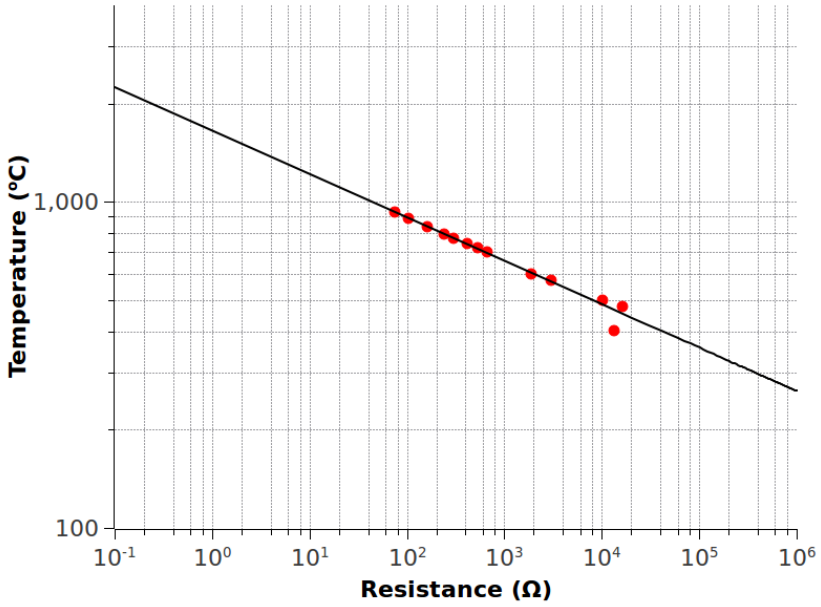

Figure 2.6: The electrolyte temperature as as a function of ohmic resistance measured at 32 MHz. Measurement of the ohmic resistance while heating by a.c. current can be used to estimate the temperature of the crystal.

YSZ crystal while heated a pyrometer was used. The pyrometer measured the temperature of the YSZ crystal through the viewport of the preparation chamber.

2.2 Ultra high vacuum chamber for angle resolved XPS

Angle Resolved X-ray Photoelectron Spectroscopy (ARXPS) was used to determine the surface composition of YSZ crystals as a function of depth. The spectra were acquired using a Thermo Scientific Theta Probe instrument. The X-ray source is monochromatized Al K_α (1486.7 eV) and the analyzer entrance accepts electrons emitted between 20° and 80° to the surface normal. The beam can furthermore be focused down to a 10 μm spot on the sample. Focusing of the X-ray beam was for example used to perform mapping of

YSZ single crystals surfaces.

2.3 Electrochemical impedance spectroscopy measurements and setup

EIS was used to characterize the YSZ single crystals under realistic SOC operating conditions. In EIS a small amplitude a.c. voltage is applied across the system. The response, i.e. the voltage and phase change, as a function of frequency is recorded. The response of the system can subsequently be analyzed and can reveal information of the losses associated with, for example, the electrochemical reactions of the electrode/electrolyte interface. EIS was performed under OCV meaning the system was run both under SOEC and SOFC mode depending on the phase of the applied a.c. voltage.

As a model system of the highly complex anode/electrolyte interface and to simulate the TPB a nickel electrode was pressed against the YSZ crystal surface as illustrated in Figure 2.7.

Before performing electrochemical experiments the rig without samples were cleaned. First the furnace tube and rig was baked in technical air (21 mol% O_2 in N_2) at 1000 °C for 24 hours. Following the baking in air the furnace tube and rig was baked in 3 % H_2O in 9% H_2/N_2. Before entering the hydrogen to the rig and samples the hydrogen was cleaned for trace sulfur impurities in the gas feed. This was done by insertion of a Ni/YSZ powder in the gas stream before entering the furnace tube. The powder is heated to a temperature 100–200 °C below the rig temperature in a alumina furnace tube. This ensures both sufficient activity of the Ni/YSZ powder and additional adsorption of sulfur on the powder.

A two electrode setup was used with a nickel wire as the working electrode (WE) and a platinum mesh as a reference (RE) and counter electrode (CE). The platinum mesh was adhered to the YSZ crystal by platinum paste which was painted on one side of the crystal.

The nickel wires were pressed against the YSZ surface by copper weights (305 g each). The weights were positioned upstream from the gas inlet, see

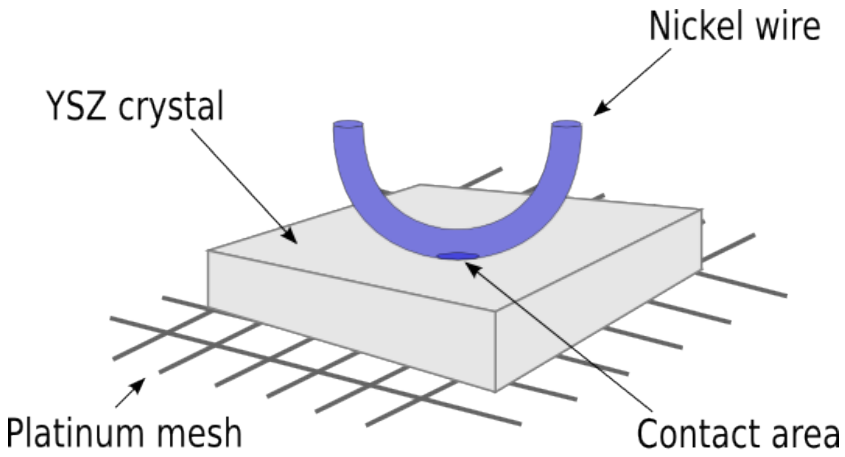

Figure 2.7: Schematic of the model system used for electrochemical measurements. A nickel wire is pressed against the YSZ electrolyte as a model of the TPB in a SOFC anode. As a counter and reference electrode a platinum mesh was used.

Figure 2.8, to minimize contamination from the copper and held by high temperature sintered alumina rods. The weights were used to avoid mechanical instability of the nickel wire and YSZ crystal interface due to vibrations and thermal expansion during ramping of temperature. A rig with four samples mounted in the setup is shown in Figure 2.8.

To minimize the creep of nickel electrodes during ramping of temperature and at measurement temperatures a flattening of the nickel electrodes was performed before they were placed on the YSZ crystal. This was done by taking a clean YSZ single crystal and dropping the nickel wire while held by the alumina rods in the rig on the surface following the approach taken by [30]. In this way a large contact area between the nickel wire and YSZ crystals have been created before applying heat to the system and creep should be minimized. After flattening of the electrodes on the reference crystal the electrodes were placed on the electrolyte for electrochemical measurements.

A frequency response analyzer (Solartron 1255b) in combination with a

potentiostat (Solartron 1287) was used to record impedance spectra. Typically a 30 mV excitation and 12 points per decade was used. The frequency was scanned from approximately 64 kHz to 0.1 Hz.

The YSZ crystals were mounted in the rig in a laminar air flow bench (>99.999% efficiency against particles of $\geq 0.3\,\mu$m) with gloves to minimize contamination from the surroundings. After mounting the crystals in the air flow bench the rig was transported to the furnace tube and secured. After the electrochemical experiments the demounting of the crystals were also performed in the laminar air flow bench from were they were transported for further analysis. The rig can hold up to four electrodes and has an YSZ

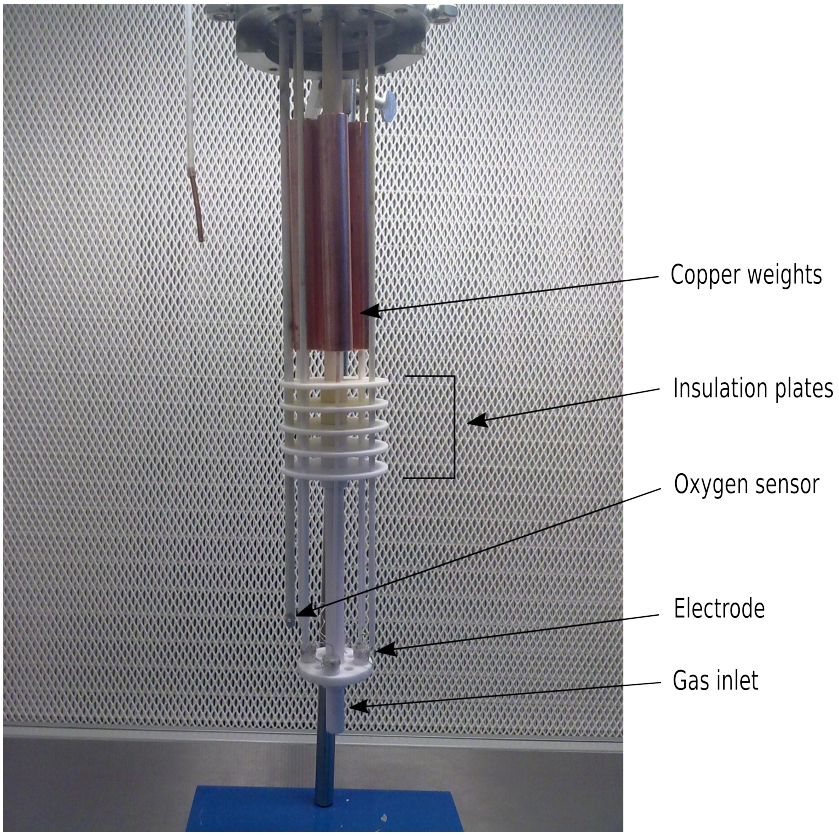

Figure 2.8: Illustration of the rig used for electrochemical measurements. Copper weights are used to press the nickel wire against the YSZ surface as a model system of the TPB in a SOC anode. The entire rig is put in a furnace tube when performing electrochemistry.

based oxygen sensor attached. The software Elchemea was used to control both a multiplexer to switch between the four samples in the rig, control the frequency response analyzer and potentiostat and collect data from the rig. The electrodes have individual platinum leads connected to the multiplexer.

2.4 Logging of data

Data acquired during this project, that being pressures, temperatures, voltages, currents etc., has primarily been logged via LabView to a MySQL database which allows for central storage of large amounts of data. Furthermore, PHP scripts have been written that allow visualizing of data stored in the database in a web browser allowing easy access to acquired data.

2.5 Additional experimental equipment

Several other techniques in other experimental setups have been employed in this project for characterization. Secondary Electron Microscopy (SEM) in combination with Energy-dispersive X-ray Spectroscopy (EDX), Transmission Electron Microscopy (TEM), X-ray diffraction (XRD) and atomic force microscopy (AFM). These methods will, however, not be described in detail in this thesis. For elaboration of these techniques the reader is referred to [31–34] and references therein.

Chapter 3

Segregation of impurities in YSZ single crystals

Experimentally it has been observed that grain boundaries in polycrystals or the external surface of YSZ single crystals is covered with an impurity phase after annealing at elevated temperatures [12, 16, 17, 35–38].

For this project YSZ single crystals (100) were purchased from MTI Corp. The crystals have a stated purity from the manufacturer of 99.99 %. The yttria doping level is 9 mol% yttria in zirconia, i.e $Zr_{0.84}Y_{0.16}O_{1.92}$, which is close to where YSZ has optimum ionic conduction [27, 29]. The crystals are 5x5x2 mm^3 which were chosen from basis of both handling capabilities and lateral resolution of analysis equipment. Each crystal has two 0.5 mm deep grooves on each side of the crystal where electrodes can be inserted for heating. The crystals are from the manufacturer two side polished ending with a silica and alumina slurry which gives a surface roughness of $\leq$5 Å according to specifications.

The crystals have from the manufacturer received a RCA (Radio Corporation of America) clean. The RCA cleaning procedure has three major steps used sequentially. First an organic clean with removal of insoluble organic contaminants with a 5:1:1 H_2O:H_2O_2:NH_4OH solution is applied. Next an oxide strip using a diluted 50:1 H_2O:HF solution is performed. Finally an ionic clean using a solution of 6:1:1 H_2O:H_2O_2:HCl is used.

3.1 Bulk analysis

The bulk impurity content in the crystals was determined by GDMS performed by Evans Analytical Group (EAG). The impurity content of elements determined from GDMS is shown in Table 3.1. In GDMS two electrodes are

Table 3.1: GDMS analysis of selected elements of an as-received YSZ single crystal. X denote element columns while Con. denotes concentration columns. Unit is ppm by weight.

X	Con.	X	Con.	X	Con.	X	Con.	X	Con.
Zn	<0.05	K	0.12	Se	<0.5	Cs	<0.5	Lu	0.22
Y	Matrix	Ba	0.1	Hf	1.7 wt.%	B	0.01	Cr	1.4
Ta	<5	O	Matrix	Mn	0.27	Nb	<0.5	Ce	1.2
Fe	5.5	Mo	0.31	Pr	10	Re	<0.5	Na	0.72
Ir	<0.5	F	<0.5	Mg	1.5	Ni	0.18	Rh	<0.5
Al	3.5	Cu	0.39	Pd	<5	Eu	3	Pt	<1
Sr	<0.1	Gd	<0.5	Au	<5	P	<0.01	Ga	<0.05
Hg	<0.5	S	0.12	Ge	<1	In	Binder	Dy	2.9
As	<5	Sn	2.9	Ho	0.55	Pb	<0.05	Ca	12
Er	2.1	Bi	<0.05	Cl	0.36	Rb	<0.5	Te	<0.5
Be	<0.05	Zr	Matrix	W	0.45	Co	0.33	Sm	0.48
Si	**18**	Cd	<200	Tl	<0.1	Br	<0.5	Tm	0.06

inserted in a chamber filled with argon gas with a total pressure of ∼1 mbar. The sample, which acts as the cathode, is bombarded with Ar^+ ions resulting in erosion of the outer atomic layers of the sample. The sputtered atoms and molecules are ionized in the plasma created from the potential difference between the sample and the anode. Typically this voltage is around 1 kV. The atoms and molecules are after ionization in the plasma accelerated to a mass spectrometer where they are separated according to their mass-to-charge ratio and subsequent analyzed by a photomultiplier or channeltron. The result of GDMS is a mass spectrum where individual peaks are used for quantification.

A silicon impurity content of 18 ppm in the bulk is found which corresponds to approximately 110 monolayers in the crystal (see Equation 5.16). Aluminium, which is also known to segregate to the surface of the YSZ crystal is present with 3.5 ppm and can hence not be expected to form a complete overlayer. The amount of sodium in the crystal is very low only contributing to the total amount of impurities by 0.72 ppm.

By summing the individual impurity contributions determined from GDMS a total purity of the as-received crystal can be estimated. Neglecting hafnium which is a heavy element and known not to segregate to the surface of YSZ, the total impurity sum gives approximately 300 ppm by weight. This corresponds to a puri ty of 99.97 % which is close to the quoted 99.99 % by the manufacturer.

3.2 Segregation of impurities in atmospheric conditions

Impurity segregation in the YSZ single crystals were studied by furnace annealing in atmospheric air. The as-received single crystals were annealed 10 hours in a ceramic furnace in atmospheric air and subsequently studied by ARXPS.

Surface analysis with surface sensitive spectroscopies can after heat treatment reveal information about segregation of impurities. A surface sensitive spectroscopy tool suitable for YSZ single crystals is XPS. Furthermore, ARXPS can by tilting the analyzer (or, in principle, the sample) give surface concentrations as a function of depth by decreasing or increasing the effective mean free path of the escaped photoelectrons. ARXPS can hence provide information of surface concentrations as a function of depth.

The data obtained from ARXPS of reference samples heated in atmospheric air is presented in Figure 3.1. Data obtained at 20° with respect to the surface normal has the lowest surface sensitivity while data acquired at 80° with respect to the surface normal measurements have the highest surface sensitivity. As seen from Figure 3.1 the silicon concentration in the surface

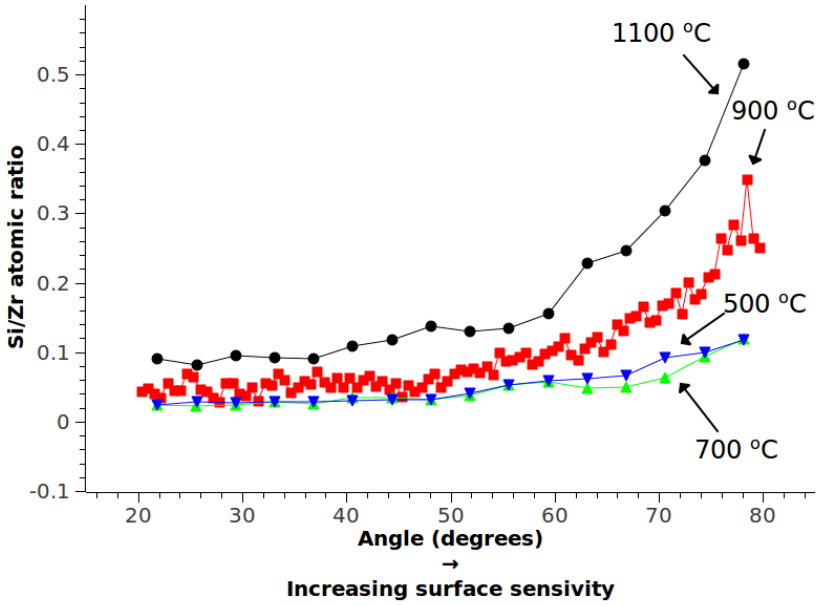

Figure 3.1: Si/Zr ratio determined by ARXPS of YSZ single crystals annealed in a range of temperatures for 10 hours in air. The angle is defined relative to the surface normal meaning higher surface sensitivity with higher angle. A clear enrichment of silicon in the outermost surface layers is seen for all annealing temperatures.

layers increased as a function of temperature. At 500 °C a very low silicon to zirconium ratio was found indicating low segregation rate. It is observed that the silicon to zirconium ratio is increased with temperature from 500 °C to 1100 °C. Furthermore, the angle resolved data show a clear enrichment of silicon in the outermost surface layers of the YSZ single crystal. Here the silicon to zirconium ratio is increased from 0.1 with an analyzer angle of 20° to 0.5 with an analyzer angle of 80° after annealing at 1100 °C. The segregation of silicon and the silicon to zirconium ratio on the surface after annealing agree well with data obtained by Hughes [16]. He found a silicon to zirconium ratio of approximately 0.25 after 200 minutes annealing at 1100 °C using an analyzer entrance angle of 70° with respect to the surface normal. In the present study the ratio was 0.28 at 70°.

Using ARXPS data a depth profile of elements can be constructed. An example of a depth profile calculated from ARXPS data is shown in Figure 3.2. The area under each component measured as a function of angle (and hence depth) is processed and weighted giving a depth-profile as shown in Figure 3.2. For the processing of the ARXPS data silicon, sodium, yttrium,

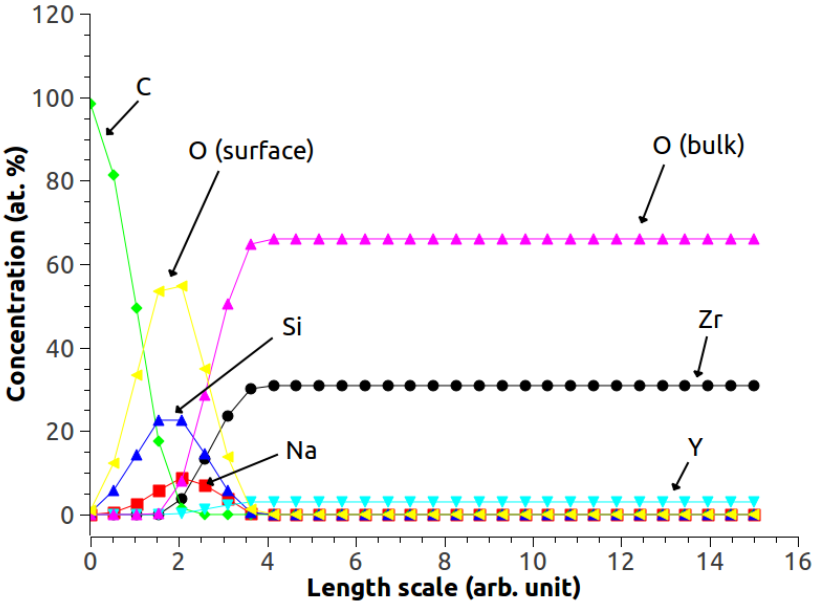

Figure 3.2: Example of a reconstruction of surface composition as a function of depth from ARXPS data. Here shown for single crystal annealed at 900 °C for 10 hrs in atmospheric air.

zirconium, carbon and oxygen were considered. A pronounced should on the oxygen 1s peak in the XPS spectrum was found suggesting two different bindings of oxygen to other surface elements. O(surface) is more prominent at the outermost surface and is presumably bonded to carbon, silicon and sodium which also enriches the surface. The O(surface) component is about 1 eV higher in binding energy in the XPS spectra compared to the O(bulk) which is the oxygen component attributed to oxygen bonded to zirconium and yttrium.

The presence of silica and sodium oxide on the outermost surface is not

surprising after annealing and agrees well with literature data [17, 40]. The large amount of carbon present on the outermost surface of the crystal is attributed to a cleaning of the crystal with ethanol before ARXPS analysis.

In Figure 3.2 the depth plot is shown for a single crystal annealed at 900 °C. Depth profiles were, however, also calculated for the single crystals annealed at 500 °C, 700 °C and 1100 °C. The depth profiles of these spectra gave the same trend as observed in Figure 3.2. No sodium was, however, observed after annealing at 1100 °C which was attributed to the decomposition of sodium oxide at this temperature.

Chapter 4

Removal of impurities in YSZ single crystals by strontium zirconate

The impurities segregated to the external surface of a YSZ single crystal in atmospheric conditions at elevated temperatures are difficult to remove since the driving force for their segregation is a lowering of the surface free energy. This implies a large energy penalty for removing the species bound to the outermost surface of the YSZ single crystal. Annealing the crystal at very high temperatures to vaporize off impurities from the surface will typically not be possible with the impurity oxides found in YSZ due to the high decomposition temperatures of these impurity oxides.

The typical impurities segregated to the surface of YSZ at elevated temperatures are silica and alumina. Removal of silica and alumina from the YSZ surface by water vapor volatilizing [41, 42] has been suggested [43].

Silica is well known to form volatile hydroxides in water vapor at elevated temperatures [41]. The reaction of solid silica with water occurs as described in Equation 4.1 at high temperatures and water vapor pressures.

$$SiO_2(s) + 2H_2O(g) = Si(OH)_4(g) \tag{4.1}$$

Hydroxides of alumina can also be formed by the reaction scheme shown in

Equation 4.2

$$\frac{1}{2}Al_2O_3(s) + \frac{3}{2}H_2O(g) = Al(OH)_3(g) \tag{4.2}$$

The relative rates of volatility of these oxides in water vapor can, as an approximation, be compared by comparing partial pressures of the primary volatile species as a function of temperature [42]. Comparison of these thermodynamic data[1] show that silicon hydroxide ($Si(OH)_4$) has a much higher partial pressure (several orders of magnitude) than aluminum hydroxide ($Al(OH)_3$) in the temperature range of 700–1500 °C [42].

Høgh [43] performed a series of experiments were YSZ crystals were heated in 8 % water in H_2/N_2 at 1450 °C with varying treatment times. XPS spectra after treatment showed that silica were continuously removed from the surface by volatile hydroxide formation. However, the XPS results also showed an increase in the alumina concentration on the surface which could be explained by the low partial pressure of aluminium hydroxide compared to silicon hydroxide. The surface was, as a result of the partial pressure difference, enriched by aluminium instead of silicon. Furthermore, the volatilization of silica from the surface proved to be a very slow and inefficient way of removing silica from the external surface of YSZ [43].

Another more plausible method of removing the impurities continuously from the surface as they segregate is to react them off the YSZ surface. This requires a compound on the surface of the crystals which reacts with the impurities on the surface as they segregate and forms a more stable compound than in its original form, i.e. a getter.

In the present study silica is reacted off the surface by providing a thermodynamically favorable reaction for the segregated silica on the surface with a getter. As getter several candidates have been suggested [44] for the removal of SiO_2. Calculations of Gibbs free energies of the reaction between silica and strontium zirconate ($SrZrO_3$), calcium zirconate ($CaZrO_3$) and barium zirconate ($BaZrO_3$) in a wide temperature window (500–1500 °C) suggest the formation of strontium, calcium and barium silicate and zirconium oxide (ZrO_2) as a byproduct to be energetically favorable at elevated tempera-

[1] Initial total pressure of 1 atm: 0.5 atm O_2, 0.5 atm H_2O

tures. At high temperatures these zirconates will tend to form silicates in the presence of silica. The formed silicates can, if the getter was applied to the external surface of the crystal, be removed by e.g. polishing. In the present study $SrZrO_3$ will be used due to its reactivity with alumina [45] and low solubility of strontium in YSZ.

4.1 Strontium zirconate powders

Two different strontium zirconate powders were used. A strontium zirconate powder from Sigma Aldrich was used as-received. The size distribution is quoted by the manufacturer to be $\leq 10\,\mu$m. A SEM image of the as-received powder can be seen in Figure 4.1. A synthesis of strontium zirconate powder

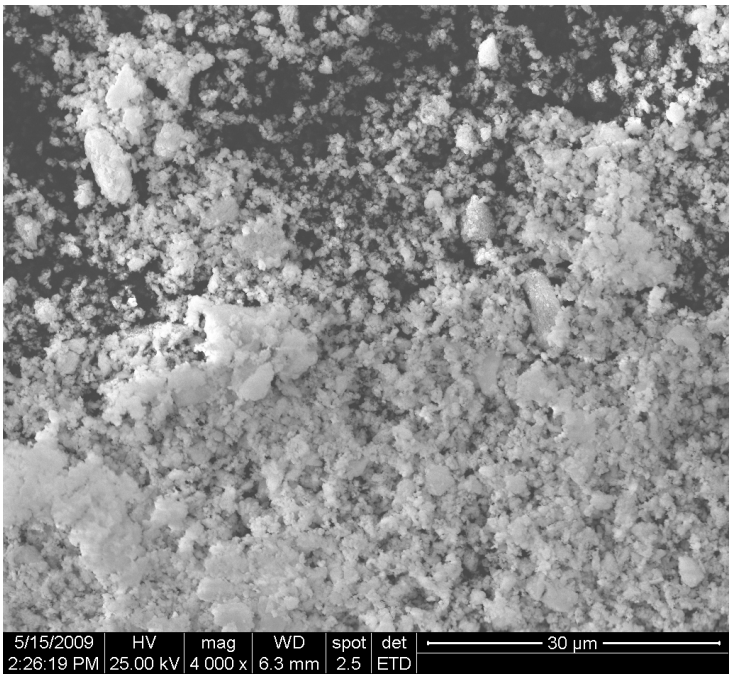

Figure 4.1: SEM image of the as-received $SrZrO_3$ from Sigma Aldrich. A wide size distribution is seen from the SEM image.

was also performed. To produce a powder with a narrow size distribution a modified synthesis by [46] was used. Here $\geq$99.5 % $ZrOCl_2{\cdot}8H_2O$, $\geq$99.0 % $Sr(NO_3)_2$, $\geq$99.5 % $C_6H_8O_7$ (citric acid) and $\geq$69 % HNO_3 (nitric acid) were

purchased from Sigma Aldrich. NH_4OH 24 % was purchased from Bie & Berntsen. A typical synthesis consists of mixing 6.446 g zirconium oxychloride, 4.232 g $SrNO_3$, 8.4 g Citric acid, and 400 ml Millipore water (18.2 MΩ·cm resistance) in a 3 l beaker. 189.4 ml NH_4OH and 76.3 ml HNO_3 was added to adjust pH to 7. The molar oxidant (nitric acid) to fuel (citric acid) ratio was kept at 18, i.e. twice the required 9 for full combustion to CO_2 and N_2.

By continuous heating the beaker is under magnetic stirring brought to 250 °C. When the liquid gets very viscous the stirring is stopped and the beaker capped with a fine sieve secured by tape. This allows escape of gases evolved but retains the formed particles. After a few minutes the solution turns brown and syrupy thereafter continued heating makes it form a hard foam. Continuing the heating approximately 10–15 min. the brown foam self-ignite. After the combustion a white powder is obtained. To verify the

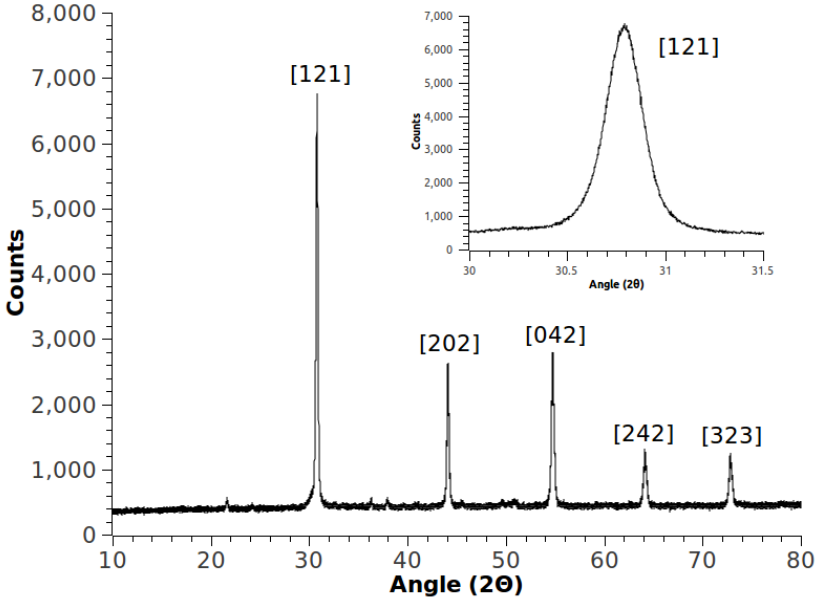

Figure 4.2: XRD of the synthesized $SrZrO_3$ powder. The major reflections are indicated. For crystallite size determination the [121] reflection shown in the inset was used.

powder was strontium zirconate XRD was performed. The XRD spectrum

of the synthesized powder is shown in Figure 4.2. All of the peaks in the spectrum can be ascribed to strontium zirconate [46–48].

Using the width of the peaks in the XRD spectrum the size of the crystallites in the powder can be calculated from the Scherrer equation [49]

$$\tau = \frac{K \cdot \lambda}{\beta \cos(\theta)} \tag{4.3}$$

where K is the shape factor, λ is the X-ray wavelength, β is the full line width at half maximum intensity (FWHM) in radians and θ is the Bragg angle. Using the [121] reflection from the XRD spectrum shown in Figure 4.2 a mean crystallite size of approximately 80 nm in the synthesized powder was determined.

4.1.1 Application of strontium zirconate to the YSZ crystals and heat treatment

The strontium zirconate powder was suspended in ethanol to achieve the most homogeneous coverage before applying the powder to the external surface of crystals. An example of a crystal surface after application of the $SrZrO_3$ suspension is shown on the left hand side in Figure 4.3. After application of the suspension to the YSZ single crystals they were placed in a clean dense alumina tube furnace where controlled heating could be applied. Each experiment had a blank sample which was used as reference. All crystals were placed on a 99.99 % pure platinum foil to avoid contamination from the furnace tube.

To accelerate the reaction between the impurities and strontium zirconate the temperature in the furnace was kept constant at 1450 °C. Furthermore, for some treatments a water vapor flow of 3 l/h during heat treatment was used. Water was supplied by a reservoir held at 70 °C corresponding to water vapor pressure of 0.15 atm. Annealing time was 100 hours. Heating ramps (up/down) were held constant at 3 °C/min. After heat treatment the samples were removed from the furnace and transported in a plastic beaker for analysis.

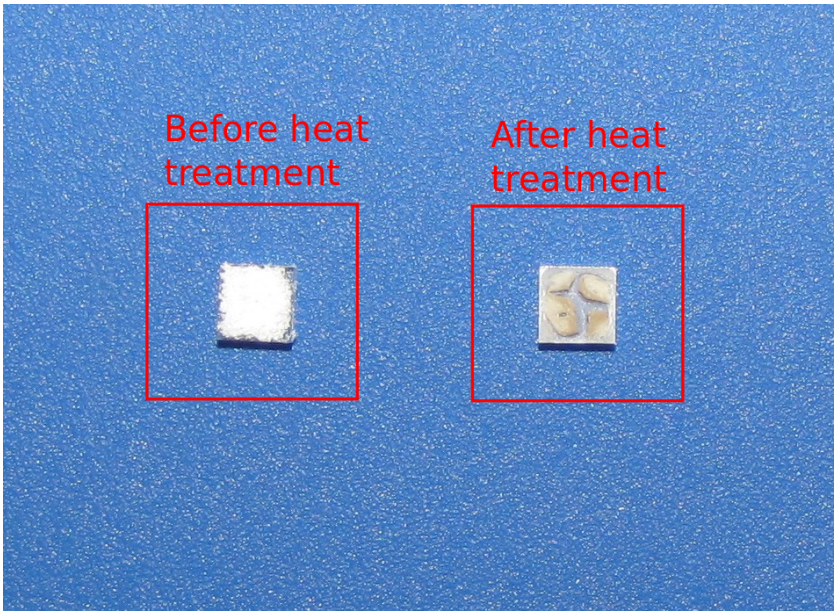

Figure 4.3: Illustration of two crystal surfaces with $SrZrO_3$ applied. On the left hand side a crystal with suspension applied is shown while a crystal with suspension after heat treatment is shown on the right hand side.

After treatment the crystals were cleaned by both ethanol and acetone. The powder residue left on the external surface of the YSZ single crystal after heat treatment, see right hand side of Figure 4.3, could not be removed by either ethanol or acetone in a ultrasonic bath. To remove the powder residue an ethanol soaked cloth was swiped across the surface. This light polishing of the surface was able to remove the powder residue from the surface. The polishing itself did not pose any damage to the YSZ crystals surface as observed on the length scale of an optical microscope.

4.2 Surface structure after heat treatment

Due to charging of the crystals when exposed to the electron beam in the microscope the crystals were coated with a carbon layer. Typically the crystals were coated with approximately 7 nm carbon and adhered to the sample holders by carbon tape to connect the sample surface to electrical ground

of the chamber. A SEM image taken directly after removal of the powder residue by swiping an ethanol soaked cloth across the surface is shown in Figure 4.4. The surface structures observed by SEM was confirmed by additional images acquired by AFM shown in Figure 4.5. A regular pattern of

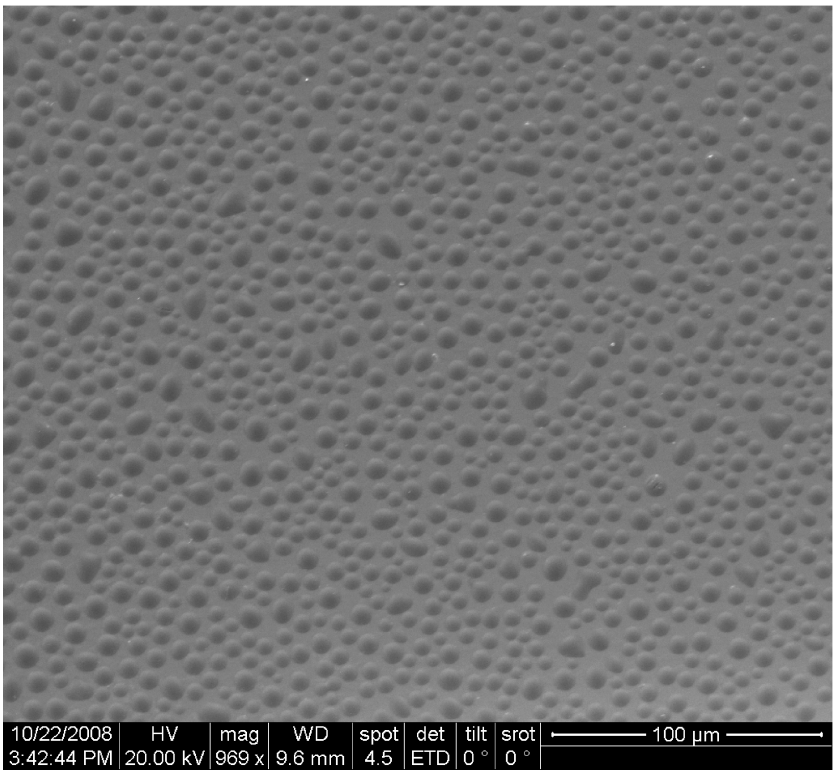

Figure 4.4: Low magnification SEM image acquired by secondary electrons showing bumps over a large area. The bumps are homogeneous in both size and height and covers 38 % of the total surface area.

ball sectioned features (bumps) was seen from both AFM and SEM evenly distributed across the surface. From Figure 4.5 the height and diameter distribution was calculated. These distributions are presented in Table 4.1. Here both the bump diameter and the height distribution was determined. From Table 4.1 the mean diameter of the bumps is 522.5 nm. The coverage of bumps on the surface is determined to 38% of the total surface area.

The bumps formed on the surface are homogeneously distributed and has a narrow size distribution. This is believed to be a property of the YSZ

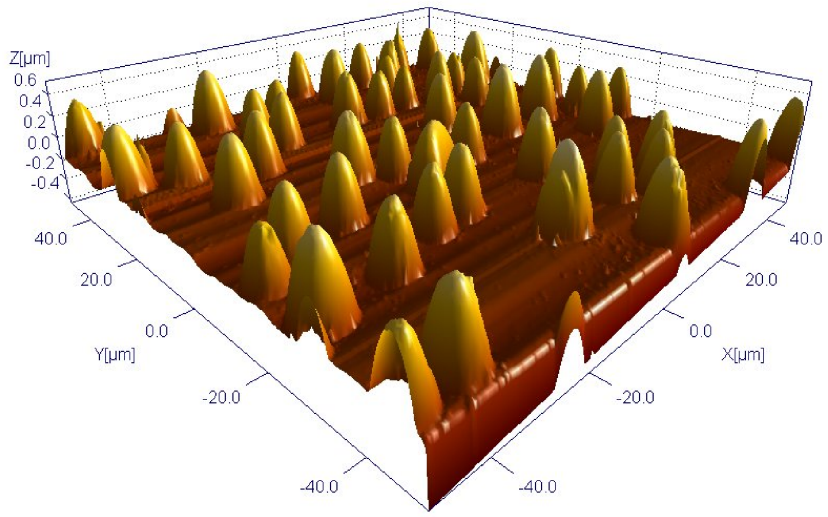

Figure 4.5: 3D representation of a AFM image of the a YSZ single crystal surface after heat treatment with $SrZrO_3$ suspension at 1450° C for 100 hours. A number of ball sectioned features on the surface is seen. Image size is 100x100 µm.

surface and powder interaction at elevated temperatures and not an intrinsic property of the size distribution of the strontium zirconate powder. This thesis is supported by the two equivalent size distributions found after treatment with the powder from Sigma Aldrich and the nanocrystalline powder. These powders have a very different size distribution ranging from the nanometer scale of the synthesized powder up to a quoted maximum diameter of 10 µm of the Sigma Aldrich powder. The diameter found from both AFM and SEM images of approximately 6 µm is hence believed to be a result surface energy minimizations. A strontium zirconate grain on the surface will react with the segregated silicon and/or aluminium and form a stable phase. This grain will then act as a nucleation point for further growth of the particle. Growth of these nuclei will then give conjoining grains and thus a solid structure which will wet the YSZ surface resulting in the bumps observed on the surface.

From analysis of AFM and SEM images the number of bumps on the YSZ surface and the total volume of the bumps can be calculated. Using the mean

Table 4.1: Statistic analysis of the observed bubbles from Figure 4.5. The bumps on the surface are homogeneously distributed across the surface of the crystal.

		Mean	Standard deviation	Median
Diameter	μm	6.90	0.96	6.82
Height	nm	522.4	52.1	520.7

diameter and height found by analysis of the AFM image the mean volume of a bump on the surface can be calculated by the geometrical formula

$$V = \frac{\pi}{6} h_{mean} \left(3a_{mean}^2 + h_{mean}^2\right) \tag{4.4}$$

where h_{mean} is the height of the bump and a_{mean} is the radius. From AFM images of the YSZ surface after treatment the mean diameter (6.90 μm) and height (0.52 μm) of the bumps was extracted. Insertion into Equation 4.4 gives a mean bump volume of $9.80 \cdot 10^{-12}\,\mathrm{cm}^3$. Assuming a homogeneous distribution (cf. Figure 4.4) of bubbles and a coverage of 38 % as found from SEM and AFM images the number of bumps on the surface can be calculated

$$N_{bumps} = \frac{A_{YSZ}}{\pi r_{bump}^2} \cdot \theta \tag{4.5}$$

where the bumps are assumed spherical and θ is the coverage. By insertion of the YSZ surface area, $A_{YSZ} = 5\mathrm{x}5\,\mathrm{mm}^2$, and the mean bump radius of 6.90 μm the number of bumps on the surface is calculated to $2.5 \cdot 10^5$. The total volume of bumps of the surface can hence be determined

$$V_{total} = V_{bump} \cdot N_{bumps} = 2.5 \cdot 10^{-6}\ \mathrm{cm}^3 \tag{4.6}$$

4.3 Composition of ball-sectioned features

XPS was used to characterize the outermost surface layers of the treated samples. Typically a survey spectrum from 1100–0 eV binding energy were acquired followed by detailed scans in regions of interest. To probe into surface structures EDX was used.

XPS spectra were measured after removal from the furnace and transport to the UHV chamber. A XPS spectrum on the surface is shown in Figure 4.6. Several nickel lines are seen in the survey spectrum (inset of Figure 4.6) which is attributed to sample holder used to mount the sample and the low resolution of the XPS equipment. Typically a large carbon signal was detected which is attributed to the exposure to atmosphere and the cleaning by ethanol and acetone. Compared to the spectra of as-received crystals large amounts of strontium, silicon and aluminium was found on the surface. The binding energies of the elements indicated oxidized states. Zirconium, yttrium and oxygen was also found in the spectra suggesting an incomplete layer of the formed phase consistent with SEM and AFM images of the surface after treatment. The binding energies of the Zr 3d and Y 3d doublets also indicated oxidized states after treatment with binding energies matching those from the non-heat treated as-received single crystal.

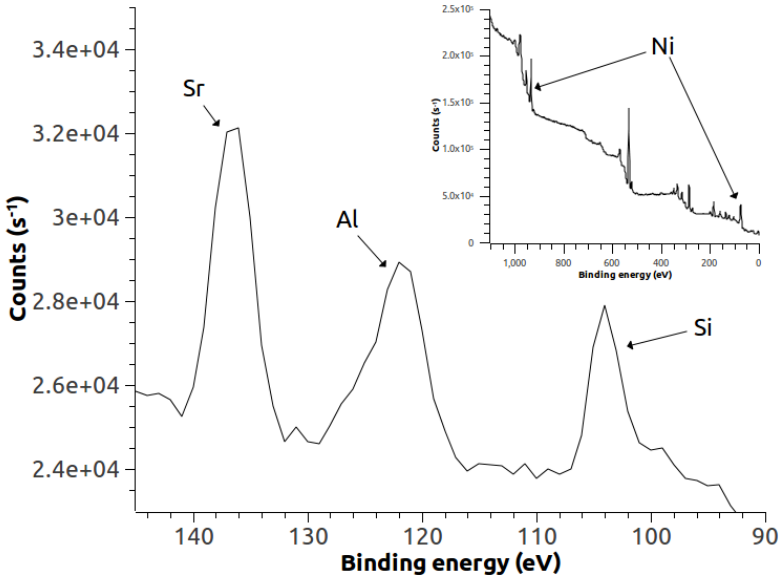

Figure 4.6: XPS spectrum of the YSZ single crystal surface after treatment with strontium zirconate at 1450 °C. A large enrichment of silicon, aluminium and strontium is seen on the surface of the crystal after treatment.

SEM in combination with EDX can be used for quantification of samples. Here the electron beam also used for imaging of the surface is used to ionize core electrons in the atoms. The X-ray fluorescence from electron relaxation in the atom is subsequently record and used to determine the elemental composition of the sample. Typically a 20 keV beam is used for excitation to obtain large elemental range. Simulations of a 20 keV electron beam in CASINO [50] shows that the interaction volume in a YSZ crystal is on the order of 1 μm^3. A signal from the bulk YSZ is hence expected with 20 keV electron beam when probing on top of the bumps which are only 500 nm in height. Areas analyzed by EDX outside bumps can be expected to be an averaging of an 1 μm^3 large volume in the YSZ bulk.

The result from a line scan made across several bubbles is shown in Figure 4.7. From Figure 4.7 a clear enrichment of silicon and aluminum is

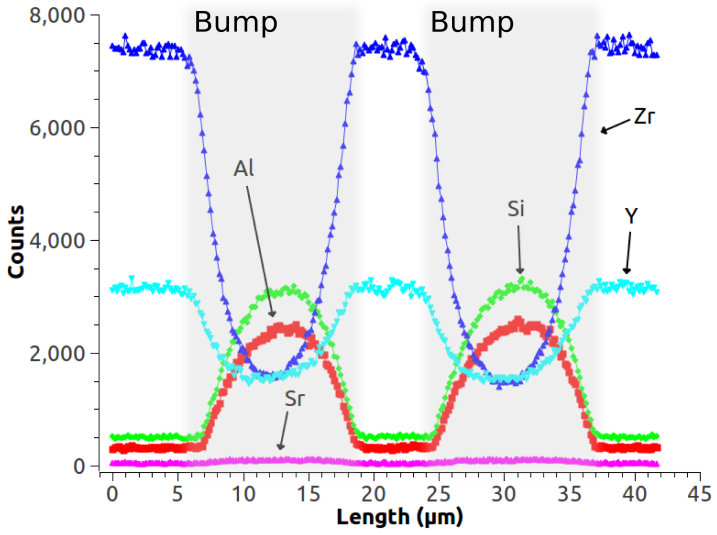

Figure 4.7: Line scan across two bumps on the single crystal surface with 20 kV acceleration voltage. A clear enrichment of silicon and aluminium is observed in the bumps.

seen in the bumps. The signal from both silicon and aluminium is clearly correlated with the position of bumps on the surface. To avoid a signal of both bumps and bulk YSZ crystal at high excitation energies the excitation

voltage was decreased to 5 kV which gave smaller interaction volume of approximately $3 \cdot 10^{-3}\,\mu m^3$ as simulated in CASINO but also smaller elemental range. Compositional analysis on a number of bumps at 5 kV acceleration voltage is presented in Table 4.2.

Table 4.2: Compositions determined from EDX with 5 kV excitation voltage. B(X) denotes on top of bumps while C(X) are outside bumps. Unit is atomic percent (at. %).

	O	Al	Si	Sr	Y	Zr
B(1)	66.5	9.6	11.7	12.2	-	-
B(2)	66.3	9.6	11.7	12.3	-	-
C(1)	67.9	-	-	-	5.9	26.1
C(2)	67.0	-	-	-	6.7	26.3
C(3)	67.3	-	-	-	6.7	26.0

Small amounts of hafnium were detected by EDX (not shown in Table 4.2) in areas outside bumps, C(X). The detection of hafnium is most likely due to the hafnium contamination (1.7 wt.% determined by GDMS, cf. Table 3.1) in the bulk of the as-received single crystal. Hafnium, however, being a typical impurity in YSZ due to the large chemical resemblance with zirconium does typically not segregate to the external surface of YSZ [19, 40]. The hafnium signal is hence expected to originate from the bulk of the single crystal and not as a surface enrichment due to the heat treatment.

Large amounts of strontium, aluminium and silicon was found in the bumps on the surface after heat treatment as shown in Table 4.2. According to the phase diagram of the SrO, SiO_2 and Al_2O_3 phases [51] a strontium feldspar ($SrAl_2Si_2O_2$) phase can be formed at temperatures above 1400 °C. Both the silicon and aluminum recorded from on-top EDS spectra agrees with this phase as the ratio of these components are close to 1:1. The strontium and oxygen content (∼12 at.% and ∼66 at.%, respectively) in the bumps are, however, higher than expected from the strontium feldspar phase.

No trace of either silicon or aluminium was detected by EDX outside the bumps. This is, however, most probably due to the low surface sensitivity of

EDX or that the crystal is clean of silicon and aluminium. If all the impurities have not reacted with strontium zirconate these areas on the YSZ single crystal will most probably be covered by a monolayer of a glassy impurity phase [52].

To compare the amount of silicon and aluminium detected in the bumps by EDX to the silicon and aluminium content in the bulk as-received YSZ single crystals a mass balance calculation is necessary.

The density of the YSZ single crystal is calculated from the lattice parameters found from XRD. The lattice parameter of 9 mol% Y_2O_3 in ZrO_2 with a cubic unit cell is 5.15 Å [53]. The density of the crystal can then be calculated from [54]

$$\rho = \left[\left(\frac{A_{Zr} + 2A_O}{100 + \sum M_k(P_k - 1)}\right) + \left(\frac{\sum P_k M_k + (\Delta A_k + [(P_{Ok}/P_k) - 2]\, A_O)}{100 + \sum M_k(P_k - 1)}\right)\right] \cdot \left(\frac{Z}{10^{-24} N d_0^3}\right) \tag{4.7}$$

which accounts for vacancies introduced in zirconia by the addition of yttria. In the case of the binary zirconia-yttria system direct insertion of the atomic weight of zirconium (91.22), A_{Zr}, the atomic weight of oxygen (15.9994), A_O, and the difference between the atomic weight of yttrium (88.905) and of zirconium, ΔA_k, Avogadro's constant ($6.02 \cdot 10^{23}$), N, the number of atoms pr. unit cell (4), Z, the number of metal ions per molecule of yttria (2), P_k, the number of oxygen ions per molecule of yttria (3), P_{Ok}, the amount of yttria in zirconia (9 mol%), M, and the lattice constant of the YSZ crystal (5.15 Å), d_0, the density of the YSZ single crystal is calculated to 5.91 g/cm^3. The amount of silicon and aluminium in the YSZ single crystal can hence be calculated directly using Table 3.1 and the dimensions of the single crystal (5x5x2 mm^3).

$$m_{Si,YSZ} = \rho_{YSZ} \cdot V_{YSZ} \cdot \gamma_{Si,YSZ} = 5.3 \cdot 10^{-6}\ \text{g} \tag{4.8}$$

where $\gamma_{Si,YSZ}$ is the impurity content determined from GDMS (Table 3.1). The aluminium content in the bulk is determined similarly to the approach

in Equation 4.8 and is calculated to $1.03 \cdot 10^{-6}$ g. These numbers should be compared with the amount of silicon and aluminium found in the bumps on the external surface of the YSZ single crystal after treatment.

Assuming the bumps are strontium aluminosilicate ($SrAl_2Si_2O_8$), which is the most likely phase according to the phase diagram, the density of the bumps is $3.04\,g/cm^3$ [55]. The total mass of bumps on the surface can be calculated by the total volume of bumps found in Equation 4.6

$$m_{bumps} = V_{total} \cdot \rho_{SrAl_2Si_2O_8} = 7.6 \cdot 10^{-6}\ \text{g} \tag{4.9}$$

The total amount of silicon in the bumps is calculated similarly to Equation 4.8

$$m_{Si,bumps} = m_{bumps} \cdot \gamma_{Si,bumps} = 8.9 \cdot 10^{-7}\ \text{g} \tag{4.10}$$

Similarly, the amount of aluminium in the bubbles is calculated to $7.2 \cdot 10^{-7}$ g.

Comparing the amount of silicon in the bulk crystal before treatment, Equation 4.8, with Equation 4.10 the amount of silicon and aluminium in the bumps on the surface is lower than the amount of silicon and aluminium found in the single YSZ crystal by a factor of approximately 6. To obtain crystals free of silicon and aluminium several subsequent treatments is necessary.

4.4 Cross-section analysis of bumps

TEM was used for characterization of YSZ-bump cross sections after treatment to investigate the interface between the bumps on the surface and the YSZ single crystal bulk.

The sample for cross-section analysis by TEM was prepared by focused ion beam (FIB) cutting on a FEI Quanta 3D FEG. A suitable area consisting of three bumps were located on the sample. The bumps on this area were covered with approximately 50 nm of platinum by Ga^+ assisted deposition of an organometallic precursor to protect the structures. After platinum deposition a thin lamella was cut by Ga^+ ion sputtering as shown in Figure 4.8. The lamella was subsequently transferred in-situ to a Cu-grid for later TEM imaging. To obtain adequate electron transparency the lamella was thinned

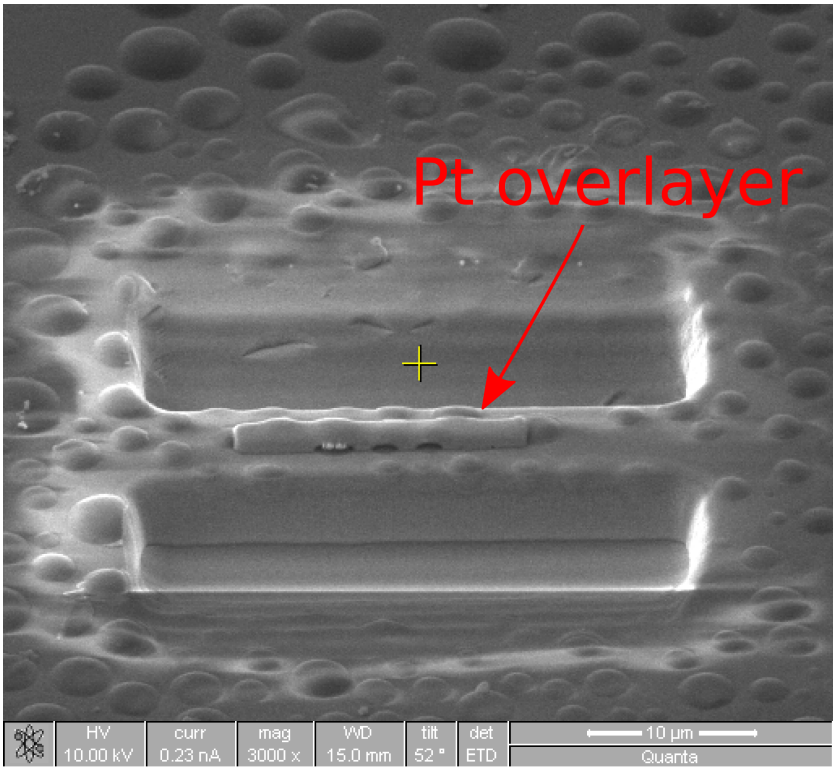

Figure 4.8: SEM image of the lamella cut by FIB containing three bumps. To avoid damage to the structures while sputtering with Ga^+ ions the structures were coated with approximately 50 nm of platinum.

down to approximately 50 nm by continuous Ga^+ ion sputtering. From the SEM the sample was transferred in air to a FEI Tecnai T20 TEM from which TEM images were acquired.

A high angular annular dark field (HAADF) scanning-TEM (STEM) image is shown in Figure 4.9. This image was acquired directly after cutting the lamella in the SEM preparation chamber and subsequent transfer to the TEM. The STEM was used to performed a line scan along the red line shown in Figure 4.10. For the line scan elements silicon, aluminium and strontium were chosen. The line scan showed an enrichment of aluminium, silicon and strontium as expected from EDS data acquired on top of bumps from SEM. Furthermore, these elements showed a large degree of homogeneity of across the bump. A clear enrichment of silicon was found compared to the bulk YSZ

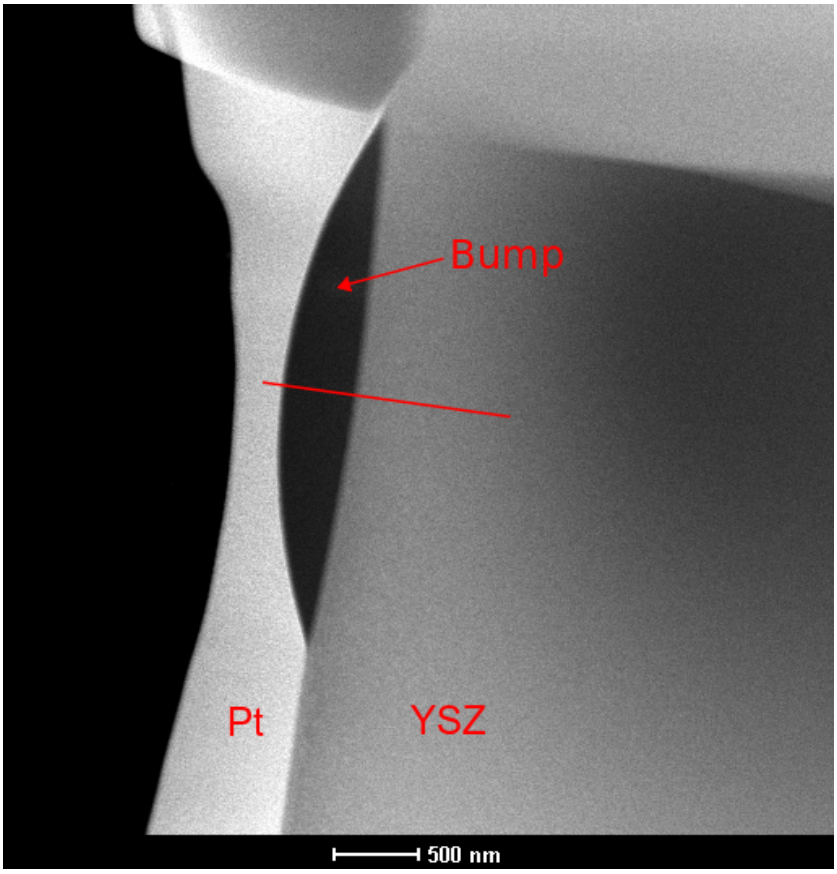

Figure 4.9: HAADF TEM image showing one of the bumps. On the left side the platinum overlayer is seen. The red line indicates the line profile used for EDX.

as shown in Figure 4.10. No trace of strontium was found from the cross-section analysis in the YSZ single crystal suggesting very low solubility of strontium in YSZ under these experimental conditions which is in agreement with other experimental data [56]. Figure 4.9 furthermore supports that the bumps are confined to the external surface of the YSZ crystal. The contrast in the HAADF TEM image indicates two separate phases which was also confirmed by the EDX analysis. The EDX data across one bump suggests homogeneity of silicon, aluminium and strontium. The apparent increased level of silicon and aluminium in the crystal in Figure 4.10 is not attributed to an increased level of silicon and aluminium near the the bump/single crys-

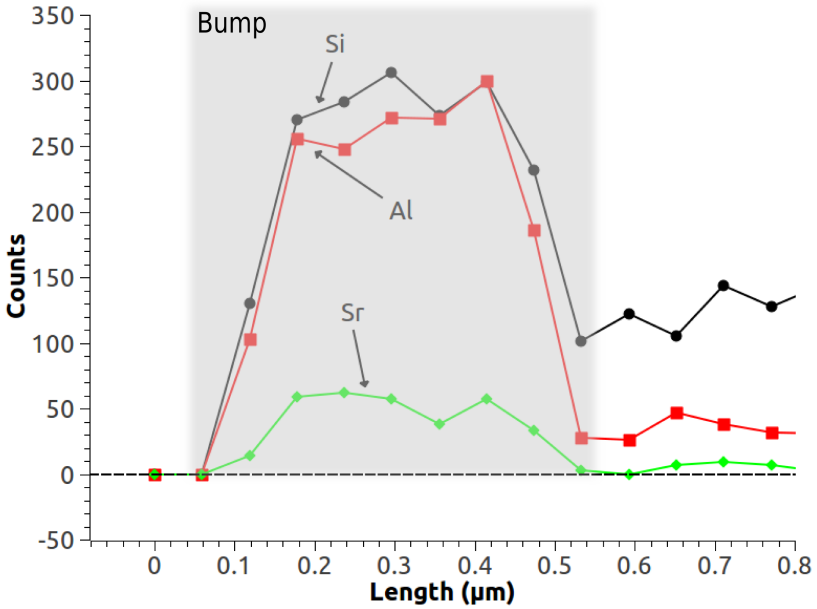

Figure 4.10: The silicon, aluminium and strontium profile recorded by EDS across a single bump. The line profile is shown in Figure 4.9

tal interface but is attributed to the overlap of the Si_K and Al_K lines with Zr_K and Y_K lines which are present when analysis is performed in the YSZ single crystal bulk region.

4.5 Cleaning of YSZ by strontium zirconate

The amount of silicon in the bumps formed on the surface of the YSZ single crystal was approximately 1/6 of the total amount of silicon on the crystal bulk. From this the total cleaning time of the YSZ single crystal can be calculated. The treatment time for the crystals was 100 hours. For preparation of the crystals and powder approximately 5 hours must be used. To remove the bumps by polishing after treatment also around 5 hours is required. The total cleaning time of the YSZ single crystal can be calculated

$$\tau = (100\ \text{h} + 2 \cdot 5\ \text{h}) \cdot 6 = 660\ \text{h} \approx 30\ \text{days} \tag{4.11}$$

Chapter 5

Annealing of YSZ single crystals under controlled atmosphere

Previous studies of impurity segregation in YSZ have been performed after annealing at high temperature of the crystal in air, i.e. in furnaces where limited or no control of atmosphere and pressure is available.

To have absolute control of atmosphere and have impurity free surroundings a UHV chamber dedicated for the study of YSZ crystal surfaces at high temperatures have been built. The preparation chamber which was interfaced to existing UHV equipment allows for studies of impurity segregation where an extreme control of atmosphere and pressure is available.

This study focuses on the impurity enrichment of YSZ surfaces observed after annealing. The crystals have been studied under extremely clean conditions as a function temperature, atmosphere and pressure.

5.1 Preparation of the YSZ single crystals

The 9 mol% YSZ single crystals was heated either in vacuum, oxygen or water containing atmospheres. The total pressure in the preparation chamber was varied by leak valves in the range $4{\cdot}10^{-10}$ mbar to 100 mbar. After annealing in the preparation chamber the crystals were transferred under vacuum by the special designed linear transfers between the preparation chamber and the

analysis chamber were the surface composition of the crystals was determined by XPS.

5.2 Heating of YSZ single crystals

The crystal was heated by a.c. voltage as described in Section 2.1.4.

The temperature ramp (down) after annealing of the crystal was kept higher than 100 °C/min and was chosen to freeze high temperature surface states. The gas atmosphere in which the crystal was annealed was not pumped out of the preparation chamber until the sample had reached room temperature. This was done to avoid any change in surface composition due to atmosphere or pressure change. To reach the equilibrium surface composition at a given temperature, pressure and atmosphere the crystals were annealed for a minimum of 10 hours.

5.2.1 Reduction of YSZ

9 mol% YSZ single crystals is transparent in the visible range (cf. Figure 5.1 and 5.2) due to its large bandgab of 4.23 eV [57].

During ramping of the a.c. voltage and during annealing with approximately 10 V_{rms} across the crystal it was reduced under UHV or at low oxygen or water vapor partial pressure conditions, cf. Figure 5.1, to a dark brown/black color. The blackening of the crystals was examined by UV-VIS spectroscopy. The absorption spectra of an as-received and an annealed crystal is shown in Figure 5.2. After annealing under low partial pressures of oxygen or water vapor the appearance of a broad absorption peak centered at 500 nm is created. The absorption spectrum is very similar to the data from Wachsman et al. [58]. They concluded the broad absorption peak around 500 nm could be assigned to a F-band absorption for a single-electron occupied oxygen vacancy created in the bandgab of YSZ.

The reduction of YSZ at low partial pressures of oxygen is believed to originate from the applied voltage resulting in an electrochemical reduction as seen by other authors [57–62]. While oxygen is present in the preparation

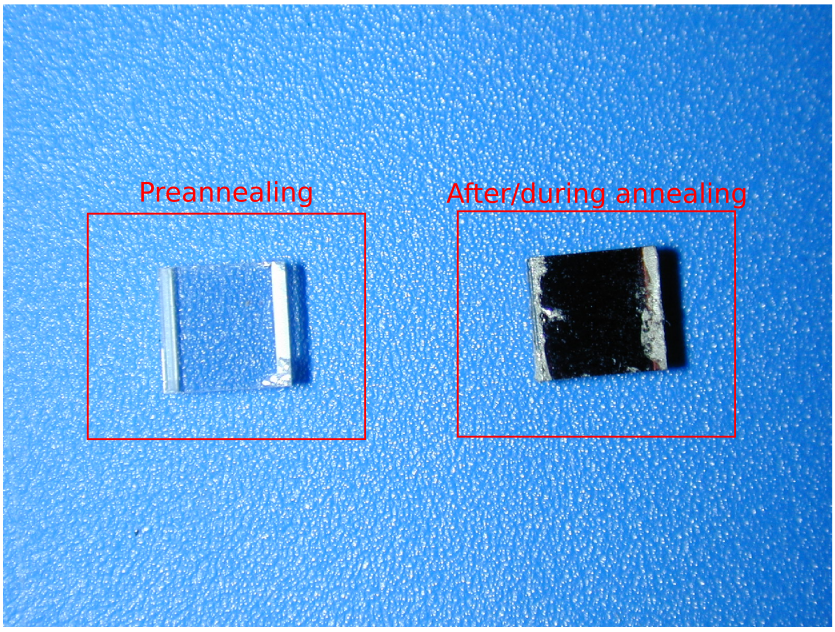

Figure 5.1: Visual comparison of an as-received and an UHV annealed YSZ single crystal. The annealed crystal was heated to approximately 1100 °C for 15 minutes and had after annealing a dark brown/black color. The platinum paste seen on the annealed crystal was not used on other annealed crystals. The platinum electrodes were henceforth pressed in the grooves of the crystal without paste.

chamber or in the crystal the electrode process is

$$O^{2-} \leftrightharpoons \frac{1}{2}O_2 + 2e^- \tag{5.1}$$

oxygen will hence evolve while one electrode is positive while oxygen is reduced on the negative electrode. When no oxygen is present in the preparation chamber zirconia or yttria is partially reduced at one electrode according to

$$ZrO_2 \rightarrow ZrO_{2-\delta} + \frac{\delta}{2}O_2 \tag{5.2}$$

Half a period later, when the a.c. voltage phase changes, the scenario is reversed and zircona is reduced at the other electrode to a non-stoichiometric phase creating a reduction zone starting from the two electrodes progressing towards the center of the crystal [63]. Due to the intense light from

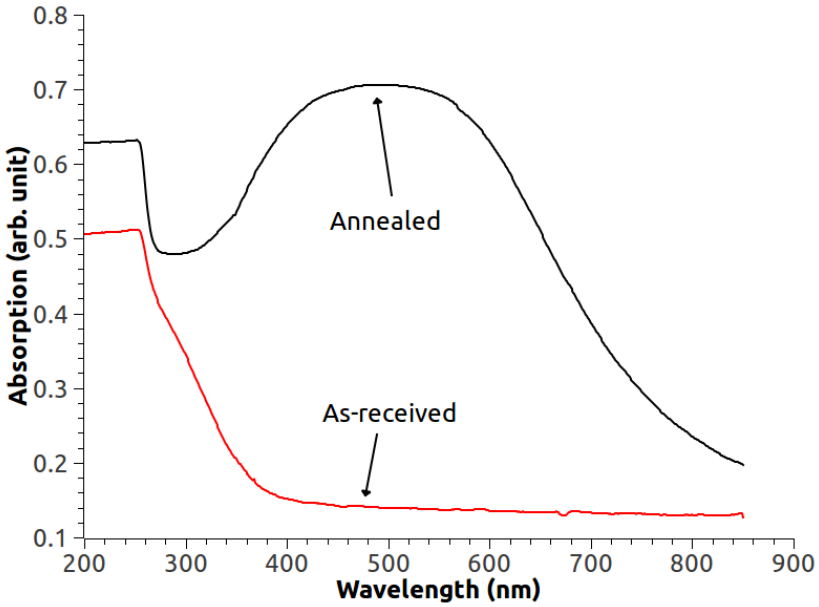

Figure 5.2: Visual and absorption spectra comparison of an as-received and UHV annealed YSZ single crystal. The crystal was annealed for 15 minutes at approximately 700 °C.

the halogen bulb for preheating the YSZ crystal the reaction zone progression from the electrodes towards the center could not be observed. Only complete reduction of the entire crystal was observed. From Equation 5.2 a complete reduction of zirconia and yttria to their metallic states can be imagined. However, no observation of such metallic sites have been observed experimentally [63]. Furthermore, XPS analysis of the fractured surface of a heavily reduced YSZ single crystal (Figure 5.3a) showed oxidized states of zirconium and yttrium in the crystal. The partial reduction of zirconium and yttrium oxide in the bulk is furthermore supported by the conductivity measurements performed by Park and Blumenthal [64] who showed that the electronic conduction through the crystal will be larger than the ionic conductivity in low oxygen partial pressures and temperatures above 1100 °C. If the reduction continued at the electrodes the zirconia and yttria would be reduced to metallic zirconium and yttrium which is not the case as discussed

earlier.

By increasing the oxygen partial pressure above 1 mbar in the preparation chamber while annealing the crystal by a.c. voltage it was reoxidized obtaining its original transparency as observed by eye. By lowering the oxygen partial pressure in the chamber while annealing the crystal it was again reduced. The oxidation and reduction of the crystal could be controlled by the oxygen partial pressure in the chamber and was fully reversible.

5.2.2 Cracking of crystals

Due to the exponential increase in ionic conductivity of the YSZ crystals with temperature a significant danger of current runaway in the circuit is present. A high temperature ramp while initiating heating of the crystal can either result in total fracture of the crystal as shown in Figure 5.3a or cracks across the crystal as shown in Figure 5.3b. To prevent current runaway and

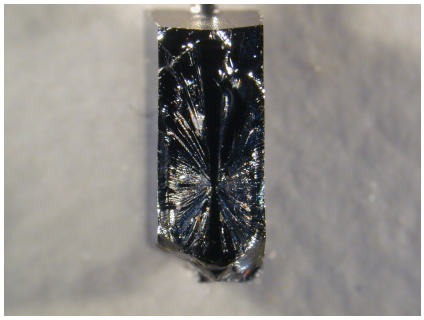

(a) Complete fracture of the YSZ crystal due to a rapid temperature ramp.

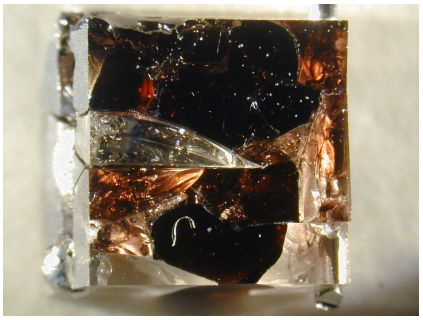

(b) Cracked crystal due to high temperature rate. Only parts of the crystal is reduced.

Figure 5.3: Examples of a.c. heated YSZ crystals cracked after rapid increase in temperature. Depending on the temperature ramp both total fracture and cracks in the crystal have been observed.

to achieve a lower temperature heating ramp a variable resistor was inserted in series with the crystal as shown in Section 2.1.4. The variable resistance acts as a current limiter while increasing the temperature of the crystal.

When the desired temperature of the crystal was reached the resistance of the variable resistor was gradually turned to zero and the current in the circuit was controlled only by the voltage across the crystal.

The cracking of crystals was not only observed during high temperature ramps. Cracking was also observed at stable temperatures when annealing the YSZ single crystal in high pressure ($> 10\,\mathrm{mbar}$) atmospheres. Annealing of the YSZ single crystal by a.c. heating is hence extremely difficult due to the large probability of fracture during annealing.

The fracture or cracking of crystals due high temperature ramps or heating in gases is likely due to the thermal gradient from the center to the surface experienced in gas atmospheres. Here the convective cooling of the crystal surface creates a thermal gradient from the center of the crystal to the surface. Høgh [43] performed stress calculations of a YSZ single crystal heating by a.c. heating. He found that the temperature gradient in the crystal was in the range of $100\,^{\circ}\mathrm{C}$ degrees and suggested this could be the reason for the fracture or crack of the crystals. His conclusion agrees well with the fracture and cracking pattern seen on the YSZ single crystals found in this work where the fracture probability at stable annealing temperatures was increased with increased pressure. However, no regular pattern of cracking of crystals could be identified. The temperature and atmosphere composition resulting in cracking or fracture was different from crystal to crystal.

5.3 Annealing of YSZ single crystals in UHV

To obtain a reference crystal heated by a.c. heating a YSZ single crystal was annealed in air in the preparation chamber. For this the preparation chamber was vented to atmospheric air. After annealing the YSZ single crystal in the preparation chamber is was pumped down. The sample was subsequently transferred under vacuum to the analysis chamber where XPS analysis was performed. From the survey scan of the YSZ single crystal oxygen, zirconium, yttrium, silicon and platinum were detected. The platinum on the surface was not attributed to a platinum enrichment of the surface but is present in the

spectrum due to the low lateral resolution of the XPS equipment meaning part of the electrodes can be seen. A binding energy scan of the silicon 2p peak is shown in Figure 5.4. Here a clear enrichment of silicon on the YSZ surface is observed in air consistent with results from annealing ex-situ in a furnace. After base pressure of the preparation chamber was reached

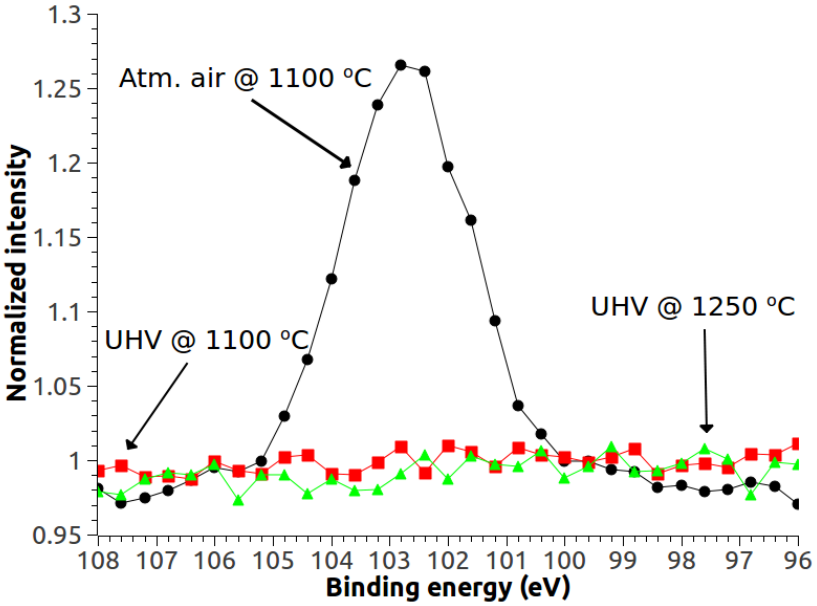

Figure 5.4: Comparison of silicon 2p spectra obtained after annealing in air and UHV, respectively. When annealing under UHV conditions no silicon enrichment was observed on the YSZ surface.

following the vent of the chamber, YSZ single crystals were also annealed under UHV conditions. From the survey spectra of the crystals annealed under UHV conditions oxygen, zirconium, yttrium and platinum was found. XPS results from the binding energy region of 108–96 eV after annealing in UHV at 1100 °C and 1250 °C are shown in Figure 5.4. At both 1100 °C and 1250 °C no silicon was observed on the surface after annealing. Further increasing the annealing time to 48 hours at both 1100 °C and 1250 °C under UHV conditions showed no difference from spectra acquired after shorter annealing times. Furthermore, YSZ single crystals annealed in a furnace

in atmospheric air before being annealed by a.c. heating in the preparation chamber was also silicon free. The silicon on the surface segregated from the bulk during annealing in atmospheric air was hence not visible after annealing under UHV conditions by a.c. heating in the preparation chamber.

Silicon was not observed on surfaces annealed by a.c. voltage under UHV conditions. After annealing a YSZ single crystal by a.c. heating in the preparation chamber under UHV conditions which was previously heated in a furnace in atmospheric air no silicon was detected on the surface. This suggests a desorption or decomposition of silica on the surface of the YSZ single crystal while annealed with a.c. voltage in low partial pressures of oxygen. The decomposition of silica to silicon monoxide and oxygen can be facilitated at high temperatures and low oxygen partial pressures

$$SiO_2(s) \rightleftharpoons SiO(g) + \frac{1}{2}O_2(g) \tag{5.3}$$

where silicon monoxide in the gas phase would be continuously pumped in UHV due to the high vapor pressure of $3.2{\cdot}10^{-2}$ mbar at 1100 °C [65]. From thermodynamical calculations the Gibbs free energy of this reaction is calculated to 450.1 kJ/mol at 1100 °C with an equilibrium constant of $7.5{\cdot}10^{-18}$ [66]. The equilibrium of silicon dioxide decomposition is dependent on the oxygen partial pressure in the preparation chamber where low oxygen partial pressures shift the equilibrium towards silicon monoxide and molecular oxygen formation.

However, in order to account for the silica free surfaces observed by XPS after annealing in UHV the silica decomposition and desorption rate must be equal to or greater than the segregation rate of silica in the YSZ crystal. The segregation rate or time to reach an equilibrium composition of the surface has not been measured explicitly here but data from Hughes [16] who investigated the segregation rate from YSZ single crystals can be used. He found that the silicon surface enrichment equilibrium was reached after 150 min. at 1100 °C. A removal rate of silica in UHV of 1/9000 monolayer/s is hence required at 1100 °C to account for the clean YSZ surfaces observed after annealing. To calculate the desorption rate from the YSZ crystal surface the flux of molecules per surface site surface should be considered. The flux

is related to the partial pressure of a given specie by the following relation [67]

$$r = \frac{F}{N_0} = \frac{p_{SiO}}{N_0\sqrt{2\pi \cdot m \cdot k \cdot T}} \tag{5.4}$$

where r is the rate of desorption (s^{-1}), F is the flux ($s^{-1}{\cdot}m^{-2}$), N_0 is the number of surface sites per square meter (m^{-2}), p_{SiO} is the partial pressure of silicon monoxide (Pa), m is the mass of the silicon monoxide molecule (kg), k is Boltzmann's constant (J/K) and T is temperature (K). The desorption rate is estimated from Hughes [16] as mentioned earlier to 1/9000 monolayer/s. Rearranging the rate equation for the partial pressure of silicon monoxide and insertion of $r = 1/9000$ s^{-1}, $N_0 \approx 1.5 \cdot 10^{19}$ m^{-2} for a (100) surface [67], $m = 7.31 \cdot 10^{-26}$ kg, $k = 1.38 \cdot 10^{-23}$ J/K and $T = 1373.15$ K gives a partial pressure of

$$\begin{aligned} p_{SiO} &= \frac{1}{9000} \cdot 1.5 \cdot 10^{19} \cdot \sqrt{2\pi \cdot 7.31 \cdot 10^{-26} \cdot 1.38 \cdot 10^{-23} \cdot 1373.15} \\ &= 1.6 \cdot 10^{-7} \text{ Pa} = 1.6 \cdot 10^{-9} \text{ mbar} \end{aligned} \tag{5.5}$$

From the equilibrium constant the oxygen partial pressure required to obtain a partial pressure of silicon monoxide of $1.6 \cdot 10^{-9}$ mbar can be calculated

$$K = \frac{p_{SiO} \cdot (p_{O_2})^{\frac{1}{2}}}{[SiO_2]} \tag{5.6}$$

where the equilibrium constant has a value of $7.5{\cdot}10^{-18}$ as stated previously. The partial pressure of oxygen can hence be estimated directly from the equilibrium constant

$$p_{O_2} = \left(\frac{K \cdot [SiO_2]}{p_{SiO}}\right)^2 = \left(\frac{7.5 \cdot 10^{-18} \cdot 1}{1.6 \cdot 10^{-9}}\right)^2 = 2.2 \cdot 10^{-17} \text{ mbar} \tag{5.7}$$

With a base pressure of $4 \cdot 10^{-10}$ mbar in the chamber the oxygen partial pressure is not expected to be in region of $2.9{\cdot}10^{-17}$ mbar and the equilibrium in Equation 5.3 would be shifted towards silica formation. The decomposition rate of silica to silicon monoxide and oxygen is hence to low to account for the silicon free surfaces observed after annealing in UHV due to the oxygen partial pressure in the system. The contribution of silica decomposition to

silicon monoxide due to temperature in the oxygen partial pressure in UHV is consequently expected to be insignificant in this system.

A faster decomposition rate of silica than direct thermal decomposition to silicon monoxide is responsible for the silicon free surfaces observed after annealing in UHV or in low partial pressures of oxygen or water vapor.

Several other routes of silica decomposition has been published in literature. Silica can also evaporate directly from the surface

$$SiO_2(s) \rightleftharpoons SiO_2(g) \tag{5.8}$$

however, this reaction is assumed negligible due to the low vapor pressure of SiO_2 at 1100 °C [68].

Reduction of silicon dioxide by hydrogen has also been studied according to the reaction [69]

$$H_2(g) + SiO_2(s) \rightleftharpoons SiO(g) + H_2O(g) \tag{5.9}$$

This reaction is endothermic and has a Gibbs free energy of 278.2 kJ/mol at 1100 °C [66]. The rate of reduction of silicon dioxide by hydrogen is considered negligible due to the low total amount of hydrogen under UHV conditions and the slow kinetics of the reaction [69].

Decomposition of silicon dioxide to silicon monoxide has also previously been reported on silicon wafers in UHV by several authors [70–72]. Ishizaka and Shiraki [72] have shown that a silicon dioxide overlayer on a silicon substrate can be decomposed within 3 minutes at temperatures down to 830 °C. They suggested a reduction of silicon dioxide by metallic silicon to be dominant according to

$$Si(s) + SiO_2(s) \rightarrow 2SiO(g) \tag{5.10}$$

The reduction of silicon dioxide to silicon monoxide is hence facilitated by the metallic silicon on the surface. However, metallic silicon is not present on the surface or in the bulk of YSZ. A reduction scheme of silicon dioxide to metallic silicon would have to occur through the reduction of silicon dioxide to silicon monoxide which would desorp, as discussed earlier, before a complete

reduction to metallic silicon would be completed. Metallic silicon is therefore not present to decompose silicon dioxide according to the reaction proposed in Equation 5.10 in our system.

None of the above mentioned silica decomposition routes are plausible in the YSZ-silica system annealed in UHV. The decomposition mechanism of silica on the surface is instead believed to occur on the reduced zirconia surface. As discussed earlier the YSZ single crystal is reduced when heated by a.c. voltage in low partial pressures of oxygen. Both partially reduced zirconium and yttrium oxide have large affinities to oxygen. The oxidation of zirconium and yttrium metal is thermodynamically favorable with 840 kJ/mol and 1509 kJ/mol at 1100 °C [66], respectively. The decomposition of silica to silicon monoxide due to the electrochemical reduction and reaction with vacancies in the reduced YSZ crystal is hence believed to be the main contribution to silica decomposition. This thesis is supported by the experimental observation that the crystal blackens at low partial pressure where silica was not observed on the surface of the crystal.

5.4 Annealing YSZ crystals in oxygen atmospheres

Silicon was not observed on the surface of the YSZ single crystals annealed under UHV conditions which was explained by the decomposition of silica on the reduced YSZ surface. Silicon was, however, observed on surfaces when the crystals were annealed in higher pressures of oxygen as shown in Figure 5.5. Here a clear oxygen partial pressure and temperature dependency of silicon enrichment of the YSZ surface was observed. Silicon was observed after annealing in 25 mbar oxygen and 1250 °C or 100 mbar oxygen and 1100 °C. The binding energy of the silicon 2p peak indicated, in both cases, an oxidized state of silicon equivalent to the silicon binding energy observed after annealing in atmospheric air. After annealing at lower pressures and temperatures no silicon was observed on the surface of the YSZ single crystal.

The observation of silicon enrichment on the surface of the YSZ crystal

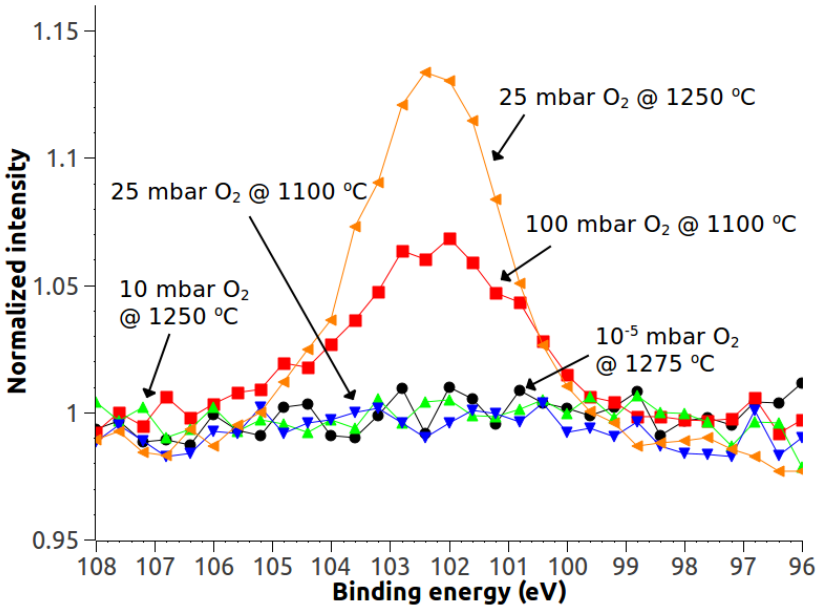

Figure 5.5: XPS spectra of the silicon 2p binding energy as a function of oxygen partial pressure and temperature. Silicon enrichment of the surface of YSZ single crystals is both temperature and oxygen partial pressure dependent.

at high oxygen partial pressures agrees well with hypothesis that silicon is decomposed on the partially reduced zirconia surface. At higher oxygen partial pressures the YSZ single crystal is not reduced which eliminates the sites for silica decomposition to silicon monoxide and oxygen.

5.5 Annealing YSZ crystals in water vapor

For annealing in water vapor a glass bottle containing Millipore water was connected to the preparation chamber. Air was evacuated from the bottle by repetitive cycles of freezing the water by liquid nitrogen and pumping the glass bottle with a turbomolecular pump.

The surface composition after annealing in Millipore water vapor is presented in Figure 5.6. A pronounced silicon peak is seen after annealing in

10 mbar water partial pressure at 1100 °C. After annealing in water vapor silicon was observed at lower total pressure in preparation chamber compared annealing in oxygen atmospheres. The area of the silicon 2p peak after annealing in water vapor is very close to the area found after annealing in 100 mbar oxygen at 1100 °C (12.1 versus 12.2) suggesting a comparable silicon enrichment at lower temperature and vapor pressure of water compared to oxygen. Silicon was not observed on samples treated in water vapor

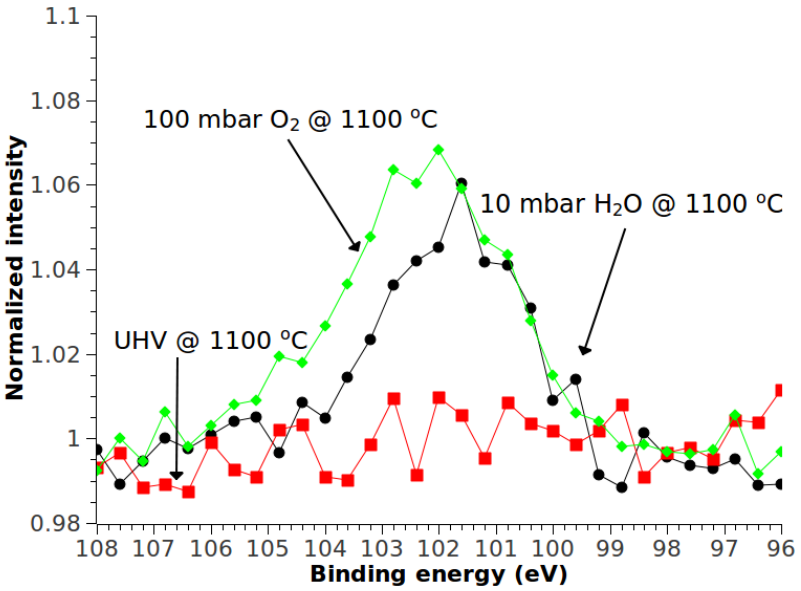

Figure 5.6: Comparison of silicon enrichment after annealing in 10 mbar water vapor, 100 mbar oxygen partial pressure and under UHV at 1100 °C.

pressure below 10 mbar at any temperature.

A comparable silicon enrichment on the surface was observed after annealing single crystals in lower water vapor pressures and temperatures compared to the crystals annealed in oxygen atmospheres. When H_2O and no O_2 is present the H_2O will be reduced to H_2 by the a.c. current. The H_2/H_2O electrode has a higher reaction rate than the oxygen electrode resulting in less reduction of the YSZ crystal surface at lower water vapor partial pressures than oxygen partial pressures. The agrees with the hypothesis that silica

is decomposed on non-stoichiometric zirconia sites which are eliminated at lower water vapor pressures compared to oxygen partial pressures.

The area of the silicon 2p peak after normalization and annealing in water vapor or oxygen gas of 100 mbar and 10 mbar, respectively, was lower than the ratio observed after annealing the crystals in air. This can be explained by the high oxygen and water vapor pressure while heating in atmospheric air. In atmospheric air the oxygen partial pressure is 210 mbar assuming a pressure of 1010 mbar and an oxygen content in air of 20.9 %. Similarly, the water vapor pressure in air is approximately 20 mbar, assuming 25 °C, 1010 mbar atmosphere pressure and a relative humidity of 80 %. The combination of high pressure of both oxygen and water compared to the pressures used in this study is therefore believed to be responsible for the differences in the observed ratios. Silicon enrichment on the surface of YSZ single crystals heated by a.c. voltage is hence highly atmosphere and temperature dependent.

5.6 Desorption of silicon species from the YSZ crystal

The silicon free surfaces observed after annealing in UHV and after annealing in low partial pressures of oxygen or water vapor is believed to be due to a decomposition of the segregated silica on the surface. To measure the species evaporated from the YSZ surface while annealed two different approaches were pursued. A mass spectrometer mounted approximately 2 cm from the YSZ surface (local mass spectrometer) was used to study the gas composition in the preparation chamber as a function of time. A second approach using a gold foil behind the YSZ sample was also employed integrating the desorped species from the hot YSZ crystal over time by acting as a cold finger compared to the hot YSZ crystal.

5.6.1 Analysis of species desorped by mass spectrometer

Initially the global mass spectrometer (cf. top right hand corner of Figure 2.1) was used to monitor the gas composition in the chamber. No silicon species was detected with this mass spectrometer. To increase the sensitivity a second mass spectrometer (local mass spectrometer) was mounted on top of the preparation chamber, i.e. very close to the hot YSZ crystal. The local mass spectrometer was used to determine the gas composition close to the YSZ single crystal surface by logging several masses continuously and performing full range scans (0–100 AMU) with regular intervals. An example of masses recorded as a function of time acquired from the local mass spectrometer, i.e. close to the crystal surface, is shown in Figure 5.7. Here O_2^+ with mass to

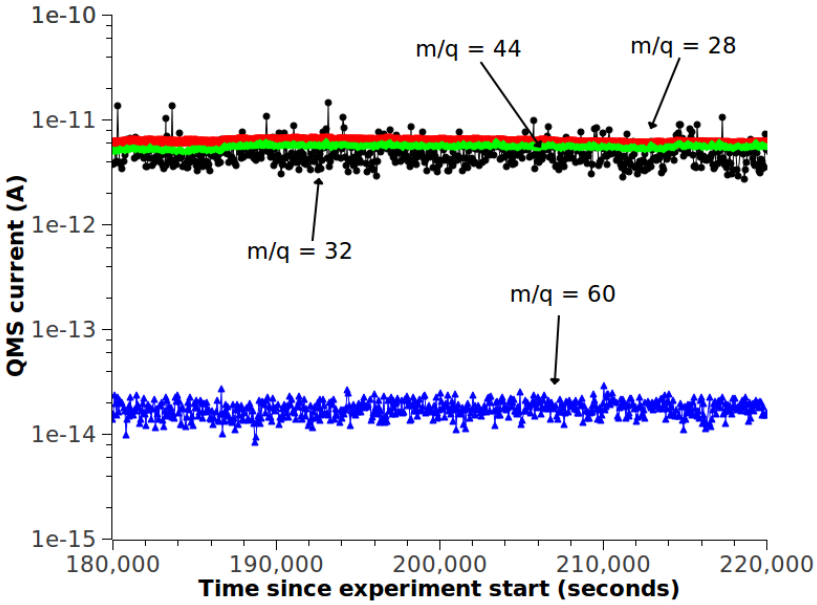

Figure 5.7: Recorded signals from the mass spectrometer as a function of time. Typically m/q=32 (O_2), m/q=28 (CO), m/q=44 (CO_2/SiO and m/q=60 (SiO_2) were logged.

charge ratio of 32, Si^+ and CO^+ with mass to charge ratio of 28, SiO^+ and

CO_2^+ with mass to charge ratio of 44 and SiO_2^+ with mass to charge ratio of 60 was logged.

The mass spectrometer was used to monitor the gas composition in real time while the YSZ single crystals was annealed. It was not possible, however, to observe any signal at mass to charge ratios 28, 44 or 60 which could be attributed to silicon, silicon monoxide or silicon dioxide. For mass to charge ratios of 28 and 44 the signal was difficult to detect due to the overlap with carbon monoxide and carbon dioxide which are typical residue gases in UHV. Furthermore, the solid angle extended by the mass spectrometer, even with the mass spectrometer filament approximately 2 cm from the sample surface, was very small due to the high sticking coefficient of silicon species on surfaces at lower temperatures than the YSZ crystal. Due to the small effective solid angle of the mass spectrometer combined with the expected low species desorption rate, due to the slow rate of silicon segregation in YSZ, it was not possible to observe any silicon species desorption with the mass spectrometer.

5.6.2 Adsorption of silicon species on a gold foil

No silicon species was observed by the mass spectrometer mounted directly above the YSZ single crystal while annealed. This was attributed to the small solid angle extended by the mass spectrometer due to the absorption of silicon species on surfaces at lower temperatures than the YSZ crystal. To enhance the signal from the species desorbed from the YSZ single crystal a gold foil (99.99 % pure) was mounted approximately 1 mm behind the YSZ single crystal on the sample holder as illustrated in Figure 5.8. The gold foil acts as an integrator of any desorbed species from the crystal and can after the YSZ crystal has cooled down be analyzed. The gold fold was after mounting on the sample holder analyzed by AES in the analysis chamber. Here AES was chosen due to the technique's high lateral resolution compared to XPS. Typically an area of 150x150 μm^2 was irradiated with 0.5 μA electron beam current for excitation corresponding to current density of 22 A/m^2.

Before annealing of the YSZ single crystal the gold foil was analyzed by

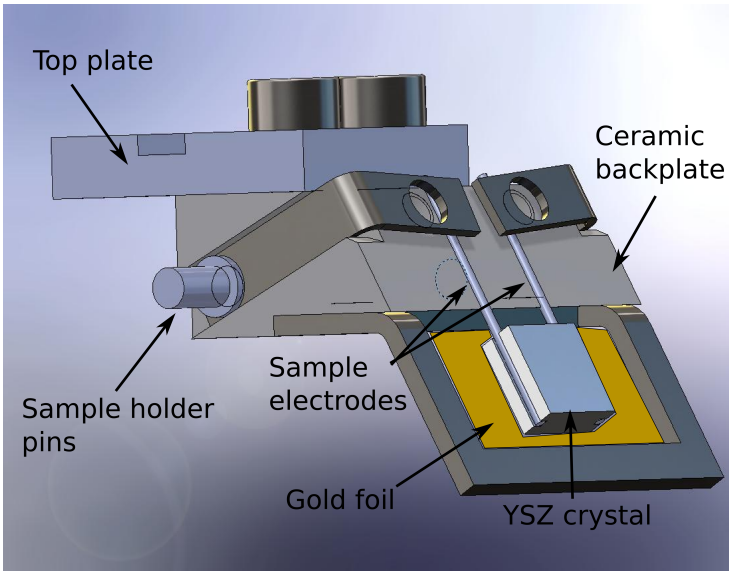

Figure 5.8: Illustration of the sample holder with the gold foil behind the YSZ crystal used for integrating any desorped silicon species from the YSZ crystal while hot. The distance between the foil and crystal was approximately 1 mm.

AES. From the spectra before annealing the YSZ single crystal only gold, carbon, sulfur and oxygen was detected on the surface of the gold foil. The use of a gold foil greatly improved the signal to noise ratio due to the time integration of the evaporated species compared to the time resolved mass spectrometer and the large surface area of the gold foil compared to the YSZ single crystal. After annealing the YSZ single crystal at 1100 °C for 10 hours a clear silicon enrichment on the gold foil was observed as shown in Figure 5.9.

Furthermore, a gradient of silicon enrichment on the gold foil while moving away from the YSZ crystal was observed. This is shown in Figure 5.10. Here spectra were acquired from near the edge of the YSZ single crystal towards the sample holder frame. As the distance from the analysis area to the crystal increased a clear decrease in the silicon to gold ratio was observed (cf. Figure 5.10a). This is consistent with silicon species desorbing from the YSZ crystal has lower probability of hitting the gold foil areas far from the surface of the YSZ crystal compared to gold foil areas very close to the surface of

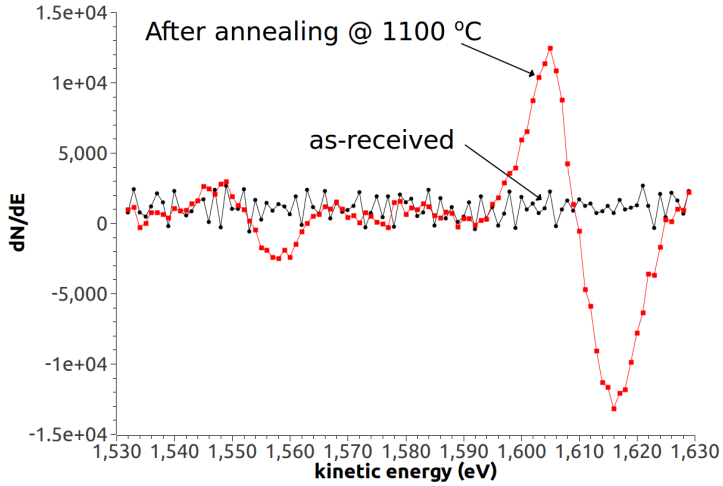

Figure 5.9: AES spectra from the silicon (KLL) kinetic energy region of the gold foil behind the YSZ single crystal taken before and after annealing of the YSZ single crystal, respectively. A clear silicon enrichment of the gold foil is seen after annealing of the YSZ crystal at 1100 °C.

crystal.

A piece of gold foil was also annealed in vacuum at 1100 °C for 10 hours in the preparation chamber without a YSZ single crystal present. The surface composition of the gold foil was after the annealing determined by AES. No silicon was found on the surface of the gold foil after annealed eliminating segregation of silicon from the bulk to the surface of the gold foil to be the cause of the observed silicon enrichment.

5.6.3 Cleaning of YSZ by vacuum annealing

The results shown in the previous sections suggest that silica impurities on the YSZ surface can be decomposed at low oxygen partial pressures by application of an a.c. voltage across the crystal. This was demonstrated by enrichment of silicon on a gold foil acting as a cold finger behind a YSZ crystal while annealed at high temperatures. The decomposition of silica on the surface implies that a finite annealing time will result in a silica free YSZ crystal.

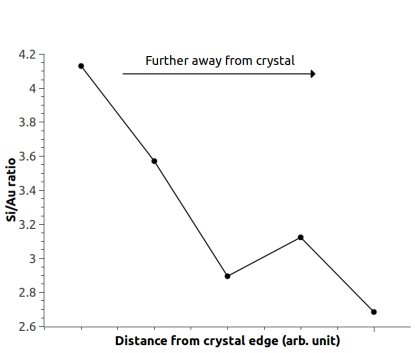

(a) Silicon to gold ratio of spectra on the gold foil after annealing of the YSZ crystal

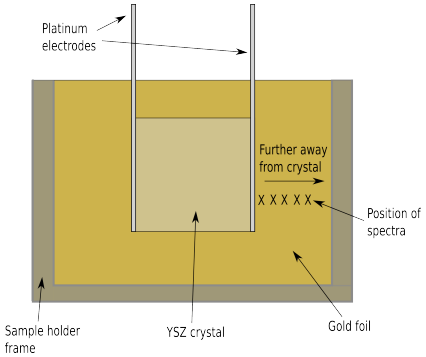

(b) Illustration of the distribution of AES spectra on the gold crystal after annealing

Figure 5.10: The silicon to gold ratio recorded across the surface. Moving further away from the crystal a decrease in the silicon to gold ratio is observed.

In order to estimate the time required for decomposition and subsequent desorption of all the silicon in the YSZ bulk crystal the total amount of silicon (or more important, the number of monolayers contained in the YSZ crystals) have to be calculated.

The molar mass of YSZ is determined by the yttria doping level (9 mol%) of the crystal

$$\begin{aligned} M_{YSZ} =& 0.91 \cdot M_{ZrO_2} + 0.09 \cdot M_{Y_2O_3} \\ =& 0.91 \cdot 123.2 + 0.09 \cdot 225.8 = 132.5 \text{ g/mol} \end{aligned} \tag{5.11}$$

As shown in Chapter 4 the mass of a YSZ crystal of a given size can be calculated from the density of the crystal. The density can be determined from the lattice parameters of the structure acquired by XRD. From the density and the volume of the crystal the mass of a 5x5x2 mm^3 YSZ crystal was found to 0.296 g. From the mass and molar mass of YSZ the amount of substance can be calculated

$$n_{YSZ} = \frac{0.296}{132.5} = 2.25 \cdot 10^{-3} \text{ mol} \tag{5.12}$$

The amount of silicon in the bulk can be calculated from the silicon concentration in the as-received YSZ bulk which was determined by GDMS (cf.

Table 3.1).

$$n_{SiO_2} = \frac{m_{SiO_2}}{M_{SiO_2}} = \frac{m_{YSZ} \cdot \gamma_{SiO_2}}{M_{SiO_2}} = 8.87 \cdot 10^{-8} \text{ mol} \tag{5.13}$$

where γ_{SiO_2} is the silica concentration in the bulk YSZ which was determined to 18 ppm.

The silica layer on the surface after annealing is most likely amorphous. For simplification, however, a pure silica overlayer is considered. The bond length between silicon and oxygen in silicon dioxide is approximately 1.6 Å [73]. Neglecting the atomic radii of oxygen and silicon and assuming a bond angle of 180° the distance between each silicon atom is 3.2 Å. This allows for calculation of the number of silicon atoms on the surface.

$$N_{surface,Si} = \left(\frac{5 \text{ mm}}{3.2 \cdot 10^{-7} \text{ mm}} \right)^2 = 2.44 \cdot 10^{14} \tag{5.14}$$

Which accounts for one side of the crystal. Accounting for both sides of the crystal sides and neglecting edges the total number of silicon atoms in the surfaces is $4.88 \cdot 10^{14}$. From the amount of silicon in the bulk and the Avogadro constant the number of silicon atoms in the YSZ crystal bulk can be calculated.

$$N_{bulk,Si} = n_{SiO_2} \cdot N_{Av} = 8.82 \cdot 10^{-8} \cdot 6.022 \cdot 10^{23} = 5.3 \cdot 10^{16} \tag{5.15}$$

The approximate number of silicon layers in the crystal is hence

$$N_{layers} = \frac{N_{bulk,Si}}{N_{surface,Si}} = \frac{5.3 \cdot 10^{16}}{4.88 \cdot 10^{14}} \approx 110 \text{ layers} \tag{5.16}$$

From [16] the equilibrium segregation time for silicon dioxide was found to 150 min at 1100 °C. Assuming silicon segregation from the bulk to the surface to be the limiting step in silicon removal from YSZ, i.e. the decomposition and desorption of silica from the YSZ surface is assumed to be much faster than segregation of silica from the YSZ bulk to the surface, the cleaning time of YSZ can be calculated as

$$\tau = T_{seg} \cdot N_{layers} = 150 \cdot 109 \approx 10600 \text{ min} \approx 11 \text{ days} \tag{5.17}$$

Removal of the silica impurities in YSZ at an annealing temperature of 1100 °C in UHV by a.c. heating is estimated to approximately 11 days.

The cleaning time by UHV annealing is hence faster and much less work consuming than cleaning by strontium zirconate.

Chapter 6

Electrochemistry of the Ni/YSZ interface

EIS was used to study the Ni/YSZ interface after cleaning the crystals by vacuum annealing. As described in Section 2.3 a bent nickel wire pressed against the YSZ surface was used as working electrode while a platinum mesh adhered to the YSZ single crystal by platinum paste was used as a reference and counter electrode. The impedance spectra were recorded in a rig setup as already described in Chapter 2. For the measurements a two electrode setup was used. A reference electrode is not necessary in this system as shown by [43] simplifying the three electrode setup to a two electrode setup by short-circuiting the counter and reference electrode.

6.1 Nickel electrodes

To study the impurity effects on the Ni/YSZ interface in SOFC anodes it is imperative not only to have an extremely clean YSZ single crystal bulk to avoid segregation of impurities at elevated temperatures but also to use very clean nickel electrodes. The as-received nickel electrodes were prepared by annealing and subsequent electropolishing. The electrodes were before and after annealing and polishing analyzed by AES in the analysis chamber of the UHV setup to determine the surface composition.

6.1.1 Surface structure and composition of nickel electrodes

Nickel wires (99.999 %) were purchased from Goodfellow. The nickel wires were bent to obtain the desired geometry for electrochemical measurements. A SEM image of the electrode before annealing and electropolishing is shown in Figure 6.1 after bending of the wire. After bending the nickel wire a very

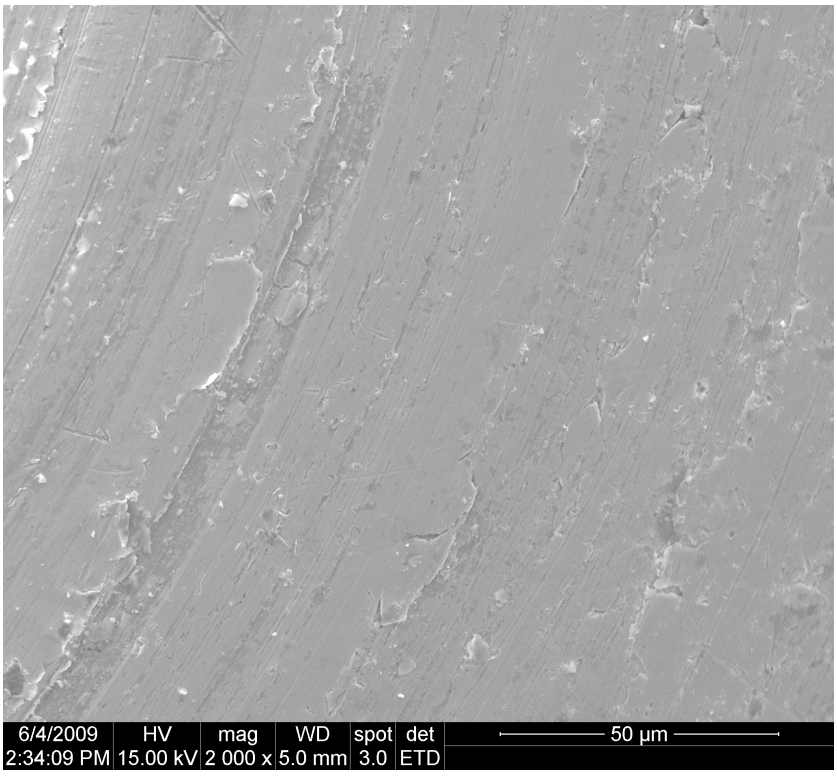

Figure 6.1: SEM image of an as-received bent nickel wire. Severe deformation is seen on the surface.

rough surface with clear deformations is seen. To obtain a smooth surface the as-received nickel wire was heat treated at 1000 °C in a 9 % H_2/N_2 atmosphere for 24 hours to anneal out any cracks in the wires arisen due to stress and strain from bending. The wires were annealed in a hydrogen containing atmosphere to remove sulfur adsorbed on the nickel electrode surface by the formation of hydrogen sulfide on the nickel surface and the hydrogen in the

gas feed following the procedure described by other authors [30, 43].

To obtain a smooth surface the nickel wires were electropolished after the annealing in 9 % H_2/N_2. Electropolishing was done in an A2 polisher (63.1 wt.% ethanol, 9.1 wt.% perchlorid acid, 10.3 wt.% 2-butoxy ethanol, 17.5 wt.% water) held at –4 °C for 4 minutes. A voltage of 10 V was applied across the nickel wire working as an anode and a platinum wire working as a cathode. By applying a potential across the cathode and anode, material is continuously removed from the nickel wire and dissolved into the electrolyte. At the anode the nickel and adsorbates on nickel is continuously reduced by the applied voltage effectively resolving nickel in the electrolyte or creating gaseous species from the adsorbates. At the platinum cathode the protons from the electrolyte and protons formed by the reduction of water is oxidized to hydrogen which desorbs from the platinum wire and bubbles through the electrolyte. The dissolution of nickel metal to nickel ions and subsequent desorption in the electrolyte due to the applied potential could also be observed visually after polishing of the wire by a significant decrease of the wire diameter.

The AES spectrum acquired after annealing and polishing showed small residues of sulfur (0.6 at.%) and chlorine (1.5 at.%). Chlorine is most probably residue from the polishing while the small amount of sulfur could be due to trace amounts of sulfur in the hydrogen used during annealing or sulfur traces on the nickel wire not reacted of the surface. The nickel electrode was furthermore enriched by a large amount of carbon (46.6 at.%) and oxygen (18.0 at.%) both of which can be attributed to the cleaning in ethanol after polishing in the electrolyte and adsorption from atmospheric surroundings. To determine whether sulfur, chlorine, carbon and oxygen was due to a surface contamination the nickel wire was sputter cleaned by Ar^+ ions. A total sputtering time of 10 minutes at 2.25 μA beam current on a 2x2 mm^2 area corresponding to a current density of 0.5 A/m^2 removing approximately 30 monolayers was used. After sputtering the nickel wire the sulfur and chlorine content was determined to 0.5 at.% and 0.4 at.%, respectively. Furthermore the oxygen and carbon content in the surface layers decreased from 46.6 % and 18.0 % to below 3 % in both cases. The decrease of both sulfur, chlo-

rine, carbon and oxygen suggests a surface contamination of the impurities detected by AES.

A SEM image of a wire after annealing and electropolishing is shown in Figure 6.2. By comparison with the as-received wire shown in Figure 6.1 a

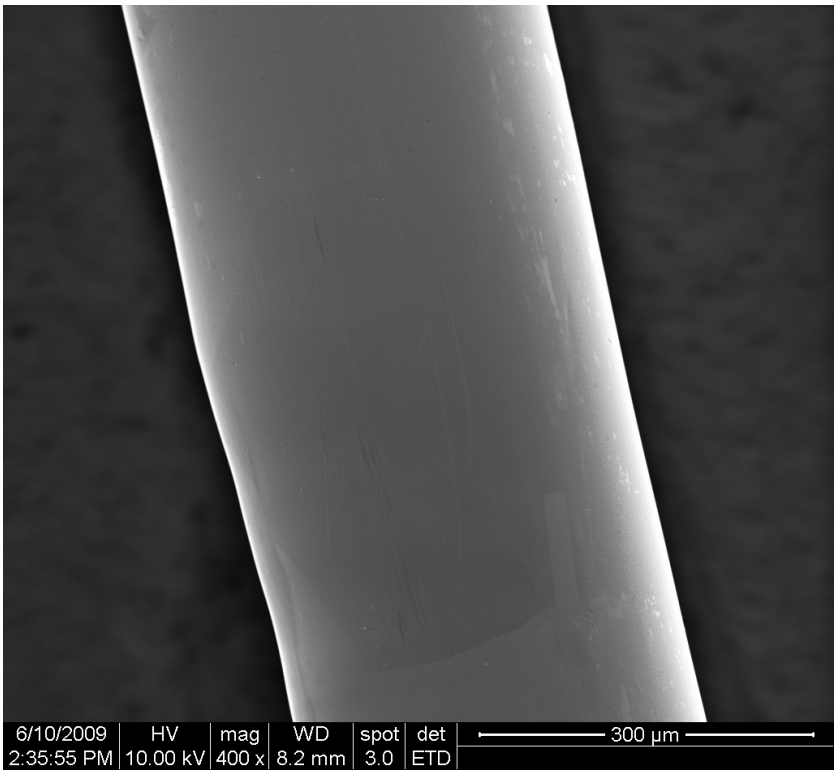

Figure 6.2: SEM image of a nickel electrode after annealing in 9 % H_2/N_2 and subsequent electropolishing. Grain boundaries are visible in the image after the polishing.

much smoother surface is observed. Also, after annealing and electropolishing the surface of the nickel wire appeared more shiny than before polishing. From the SEM images taken of the wire after annealing and polishing grain boundaries were observed as illustrated in Figure 6.2. The visible grain boundaries on the surface of the nickel wire suggests a very smooth surface.

6.2 Electrochemical impedance spectroscopy

EIS was performed in a rig setup as described in Chapter 2. The rig accommodates up to four samples simultaneously. Here two samples was chosen as reference samples while the other two had been attempted cleaned by UHV annealing as described in Chapter 5. The electrochemical measurements was performed at 850 °C in an atmosphere of wet hydrogen (3 % H_2O in H_2) at OCV. The excitation voltage frequency was swept from 54463 Hz to 0.1 Hz with a 30 mV amplitude. The frequency range was determined by both equipment limitations, avoidance of overtones of net frequency and the appearance of a test run before starting the actual measurements. The acquisition time for each individual spectrum was approximately one hour with the parameters used. The experiment start time is defined from when the furnace reached 850 °C. After acquisition of the spectra the series and polarization resistances were extracted.

Four different samples were measured by EIS and subsequently characterized by XPS. Two samples were used as reference. These crystals are denoted reference crystal 1 and 2, respectively. The other two samples on the rig were UHV annealed samples. These are denoted vacuum annealed sample 1 and 2, respectively. Vacuum annealed sample 1 was annealed 180 hours corresponding to approximately 7 days at 1100 °C under UHV. Vacuum annealed sample 2 were annealed at 1100 °C for 350 hours corresponding to approximately 15 days also under UHV.

The series resistance of the crystal is found by the real axis intercept at high frequencies in a Nyquist plot (see Figure 6.3) and is due to ohmic losses in the electrolyte and the electrode. The series resistance will in general depend on the contact area between the nickel electrode and the YSZ surface and the temperature used in the experiments. Any creep of the nickel electrode on the YSZ surface with time resulting in a change of the contact area will hence be reflected in a variation of the series resistance. In the case of YSZ the series resistance will furthermore be temperature dependent due to the strong temperature dependence of the oxygen ion conductivity of YSZ [28].

The polarization resistance is found as the difference between the series resistance (high frequency intercept with the real axis) and the low frequency intercept with the real axis in a Nyquist plot (see Figure 6.3). The polarization resistance or overpotential is related to the electrochemical processes in the interface between working electrode and counter electrode and can hence be used to describe processes and determine their individual overpotentials. For impurity free interfaces the polarization resistance is expected to be much lower than for an interface covered with impurities [10, 13].

6.2.1 Series and polarization resistance

Electrochemical impedance measurements were performed on four samples measured in succession by using a multiplexer in an automated setup. The four YSZ single crystals was contacted by a bent nickel wire working as electrode as described previously. An example of an acquired EIS spectrum is shown in Figure 6.3 while additional spectra is shown in Appendix A. From this type of plot the series resistance can be deducted by direct read off from the Nyquist plot in Figure 6.3.

Compilation of the series resistance, R_s, as a function of experiment start is shown in Figure 6.4. For all of the samples the series resistance tends to drop off fast during the first 15–20 hours of experiment time. After the initial drop the series resistance stabilizes and decreases then only slightly within the next 60 hours. The stabilization of the series resistances after the first 15–20 hours of experiment suggests the final contact area has been reached after this period. Creep of the nickel electrode is hence minimized after this period. The series resistances of the two vacuum annealed samples and reference crystal 2 all have series resistances which are almost identical after the first initial decrease. Only reference crystal 1 has after the initial decrease a consistently lower series resistance of approximately $30\,\Omega$ compared to the three other samples in the rig.

The electrical contact area of the nickel wire can be estimated from the Newman equation [74] which relates the series resistance with the geometrical

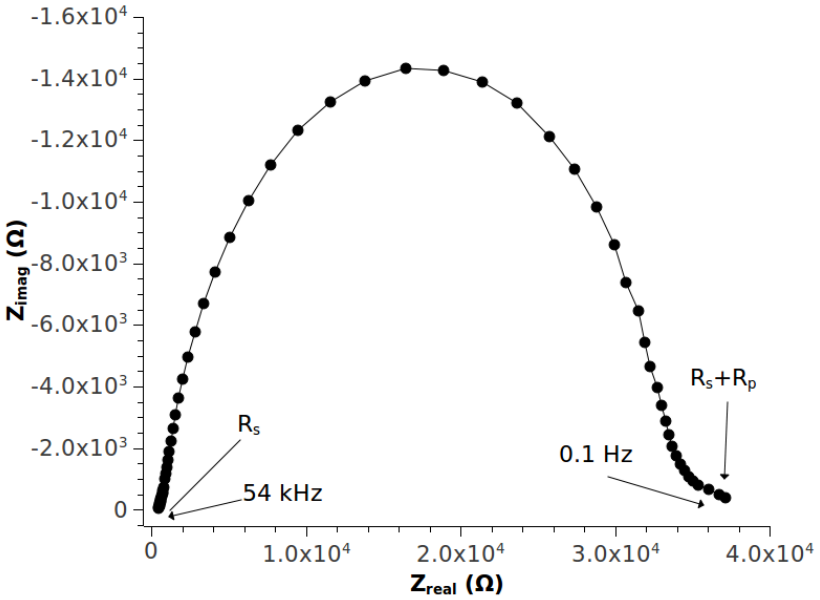

Figure 6.3: Electrochemical impedance spectroscopy data from vacuum annealed sample 2 64 hours after experiment start plotted in a Nyquist plot. From these plots the series and polarization resistance are found.

electrical contact area

$$R_s = \frac{1}{4\sigma r} \tag{6.1}$$

where R_s is the series resistance of the crystal, σ is the conductivity of the electrolyte and r is the radius of the electrical circuit contact area. The Newman equation only accounts for circular areas which is not the case when pressing the bent nickel electrodes against the YSZ electrolyte. Typically the contact area will be elliptical in this case. To account for an elliptical contact area an equivalent diameter is used

$$r_e = \sqrt{\alpha \cdot \beta} \tag{6.2}$$

where α and β are the major and minor diameter of the elliptical contact area, respectively.

Also from the Nyquist plot the polarization resistance can be extracted by determining the low frequency intercept with the real axis. In Figure 6.5

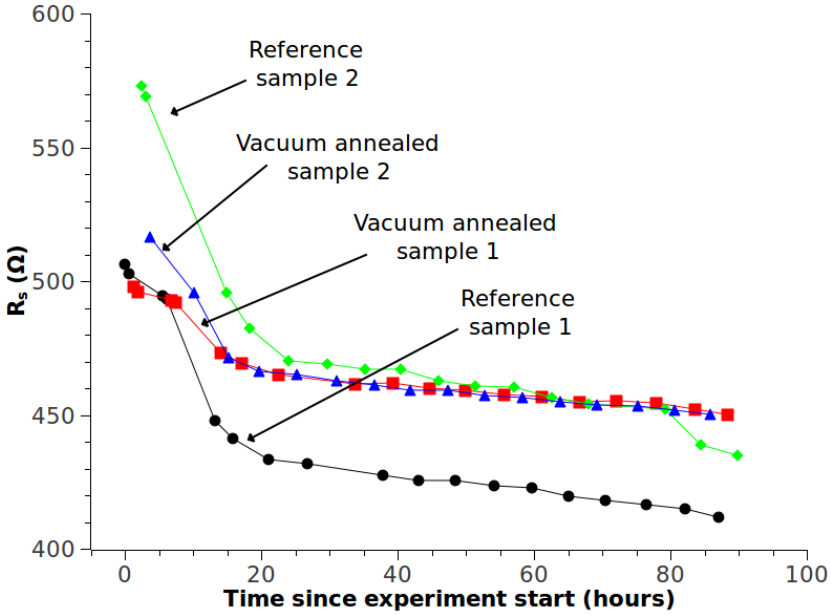

Figure 6.4: The series resistance, R_s, as a function of time since experiment start, i.e. temperature of the furnace had reached 850°C. The series resistances of all of the samples decrease quickly within the first 20 hours after experiment start until reaching a more stable region after the initial decrease.

the polarization resistance as a function of experiment time is plotted. For reference samples 1 and 2 the polarization resistance is in general higher than the polarization of the vacuum annealed samples 1 and 2 at experiment end. Especially reference sample 2 has a high, but also very fluctuating, polarization resistance compared to vacuum annealed sample 2. For reference sample 1 and vacuum annealed sample 1 the polarization resistance has overlapping values for the first 40 hours of experiment time hereafter reference sample 1 seems to increase slightly towards the experiment end. The situation is reversed for vacuum annealed sample 1. Here the polarization value starts off high and steadily decreases towards the experiment end. Vacuum annealed sample 2 has a consistently lower constant polarization resistance than the three other samples throughout the experiment.

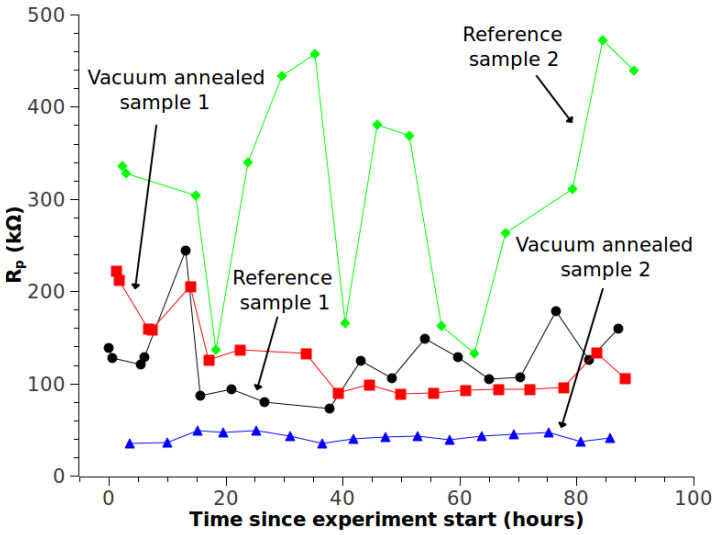

Figure 6.5: Polarization resistance, R_p, as a function of time since experiment start. Reference sample 2 has the largest but also very fluctuating polarization resistance while vacuum annealed sample 2 has the lowest polarization resistance.

6.2.2 Surface characterization of electrolytes after electrochemical experiments

The electrolytes were after the EIS measurements transferred to a UHV chamber were the surface composition of the crystals could be determined.

To picture the contact area a focused X-ray source was used for XPS analysis. This allowed visualization of both the nickel contact area and the impurity distribution on the surface with lateral resolution. For each sample the nickel contact area was found by survey spectra distributed randomly across the surface. After location of the contact area on reference crystal 1 and vacuum annealed sample 1 mappings of aluminium, silicon and nickel was performed. The mapping was performed by acquiring individual narrow XPS spectra of the element region of interest in 100x100 μm matrix elements. A 100x100 μm analysis area was used to increase signal to noise ratio was is very low when using 10x10 μm areas. This allowed for visualization of the

nickel contact area and a rough estimate of the geometrical nickel contact area.

In Figure 6.6 the nickel contact area for reference crystal 1 is plotted. The intensity of the individual matrix elements is proportional to the area of the XPS peak in that matrix element and is hence directly correlated to the amount of the given component on the surface.

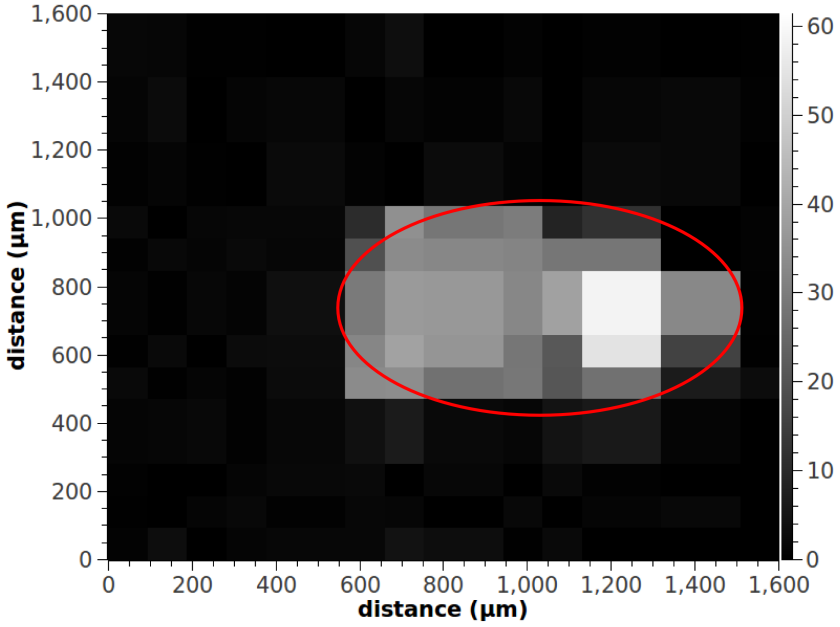

Figure 6.6: Mapping of nickel on the YSZ surface of reference crystal 1 after electrochemical experiments. The nickel map can be used to estimate the contact area between the electrolyte and electrode.

By inspection of Figure 6.6 the major and minor diameter of the ellipse can be found. By simple calculation the area of the ellipse can be calculated

$$A_{r,geo,1} = \frac{1\mu \text{ m}}{2} \cdot \frac{575\mu \text{ m}}{2} \cdot \pi = 0.45 \text{ mm}^2 \tag{6.3}$$

This area can then be compared to the area calculated from the electrical measurements calculated by Equation 6.1.

$$R_s = \frac{1}{4\sigma\sqrt{\alpha \cdot \beta}} \Rightarrow \alpha \cdot \beta = \left(\frac{1}{4\sigma \cdot R_s}\right)^2 \tag{6.4}$$

From Figure 6.4 the series resistance of reference sample 1 at the experiment end is determined to 410 Ω. The conductivity of the YSZ single crystal is determined to 0.08 S/cm by the conductivity measurements performed for temperature calibration (cf. Chapter 2). The area calculated from the electrical data can hence be calculated directly

$$A_{r,el,1} = \frac{\alpha \cdot \beta}{4} \cdot \pi = \frac{\left(\frac{1}{4\sigma \cdot R_s}\right)^2}{4} \cdot \pi = 0.46 \text{ mm}^2 \tag{6.5}$$

Equivalent to the nickel mapping a silicon map was also performed. The silicon map acquired from the reference sample 1 is shown in Figure 6.7. Here a clear silicon enrichment of the surface is seen. This is expected due to the known segregation of silica in YSZ at elevated temperatures (cf. Chapter 3). By visual comparison of Figure 6.6 and Figure 6.7 a clear correlation

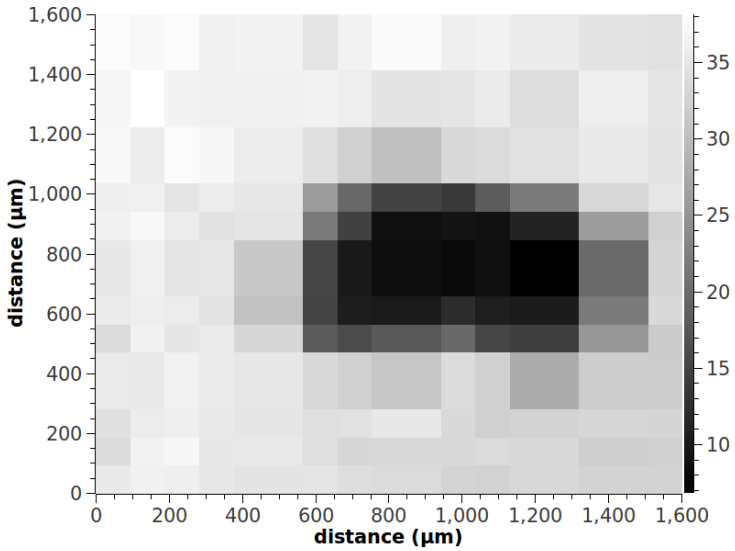

Figure 6.7: The silicon signal around the contact area for a reference sample. The silicon is concentrated around the contact area which can be seen by visual comparison to Figure 6.6.

is seen. In the nickel contact area a silicon poor region is observed whereas the surface outside the contact area is clearly enriched with silicon. Silicon enrichment around the contact area and not in the contact area is consistent

with previous observations of the point contact area after EIS experiment of a Ni/YSZ interface [30, 43, 52]. Furthermore, the XPS spectra from the individual matrix elements after electrochemical experiments all suggest an oxidized phase of silicon which agrees well with the observed oxidized state of silicon dioxide on samples annealed in furnaces at elevated temperatures (cf. Chapter 3).

Additionally, a mapping was also performed by scanning the aluminum binding energy range. In Figure 6.8 the result from mapping of aluminium on the surface of the crystal is shown. Like the silicon mapping of the crystal

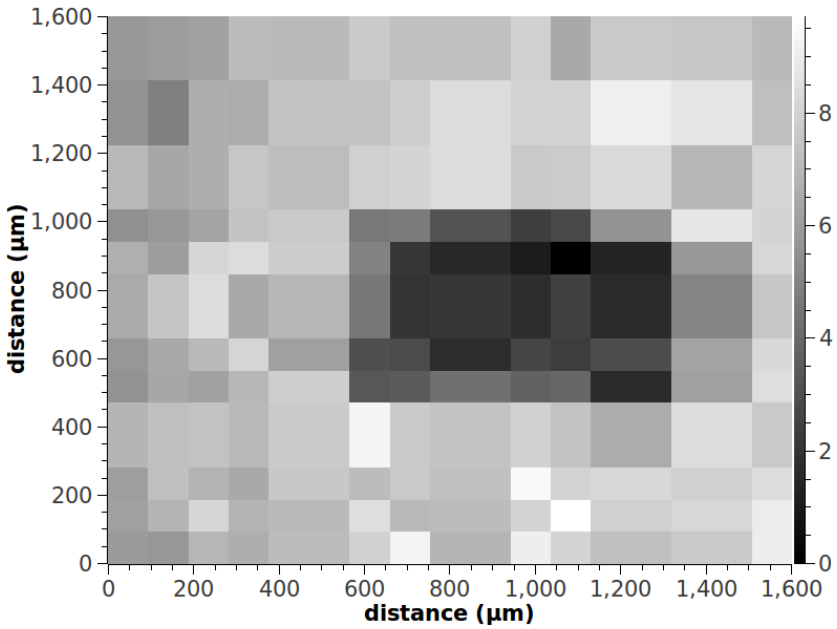

Figure 6.8: Mapping of aluminium of the reference crystal. The aluminum signal is at maximum outside the contact area comparing to Figure 6.6.

after electrochemical experiments the aluminium signal is highest outside the contact area. Outside the contact area the aluminium signal increases indicating a strong tendency of the aluminium the enrich the surface of the YSZ crystal. The aluminium binding energy suggests, as in the case with the silicon mapping, an oxidized state on the surface.

From the survey spectra and the detailed scan also performed inside and

outside from the nickel contact area the composition of the surface layers can be determined. In Figure 6.9 the composition of the surface layers inside and outside the contact area has been determined. As seen from Figure 6.9 the

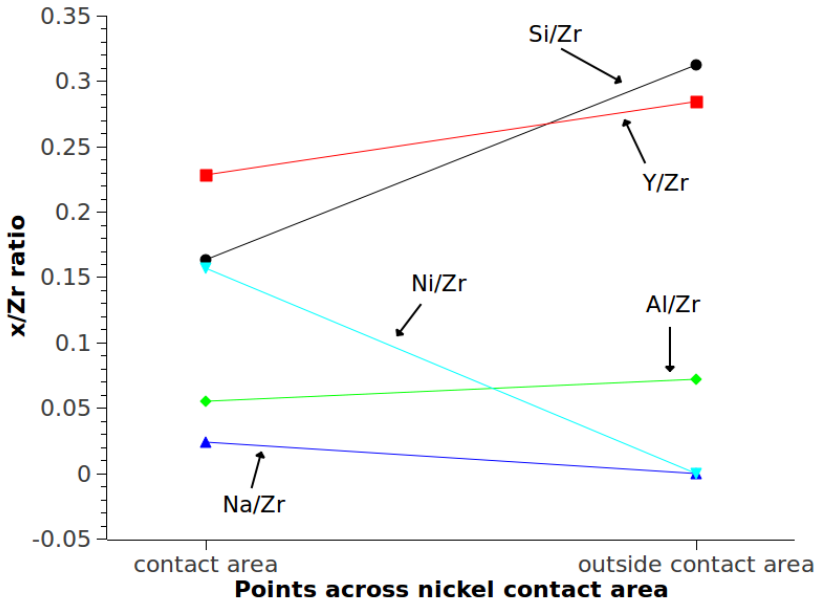

Figure 6.9: Point XPS spectra across the nickel contact area for a reference sample 1.

composition of aluminium and sodium inside and outside is almost equivalent. This suggests a very low enrichment or depletion of aluminium and sodium in the sample. The aluminium contrast difference shown in Figure 6.8 is hence due to a very small difference in composition inside and outside the contact area.

In the contact area a silicon to zirconium ratio of approximately 0.15 was found. From measurements outside the contact area the ratio between silicon and zirconium increased to 0.3 which compares to the amounts found on as-received YSZ single crystals after annealing in air for 10 hours at 1100 °C. The amount of silicon on the surface in the contact layers is hence about half the amount of silicon outside the contact area.

A small increase in the concentration of yttrium outside the contact area

is also found. The yttrium to zirconium ratio increases from approximately 0.23 to 0.28 when comparing compositions in and outside the contact area.

The nickel signal is as expected only observed in the contact area. No nickel was observed outside the contact area.

The reference sample where the mapping of nickel, silicon and aluminium was performed was compared to mapping performed on one of the crystals cleaned by vacuum annealing. As mentioned before the reference samples and the vacuum annealed samples where measured on the same rig and in the same batch, i.e. the reference and vacuum annealed samples experience exactly the same gas mixtures and temperatures.

In Figure 6.10 the nickel mapping on vacuum annealed sample 1 is shown. Equivalent to reference sample 1 the geometrical and electrical contact area

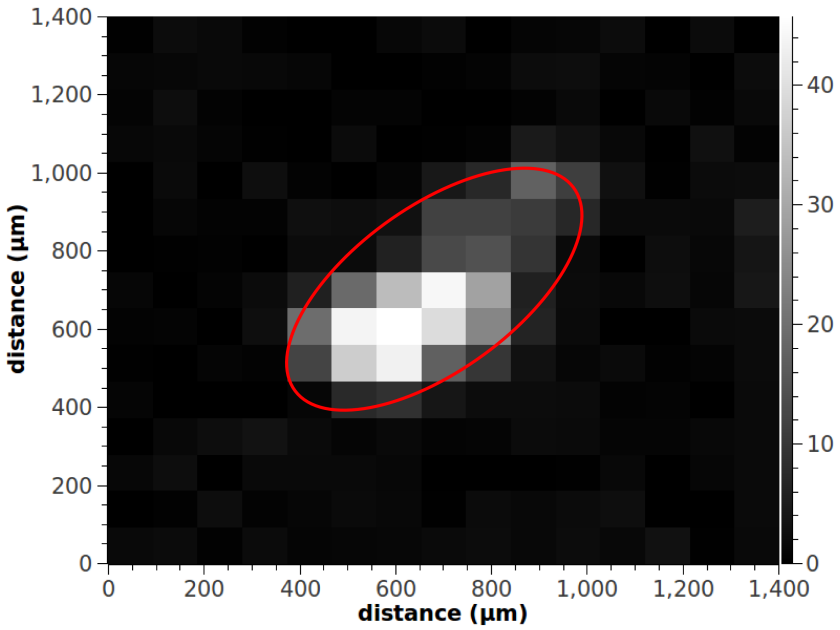

Figure 6.10: The nickel contact area as seen by focused XPS. A ellipsoidal area can be seen from as expected from a point electrode.

can be calculated. From Figure 6.10 the geometrical area can be calculated

$$A_{v,geo,1} = \frac{1.2}{2} \cdot \frac{0.5}{2} \cdot \pi = 0.46 \text{ mm}^2 \tag{6.6}$$

The contact area calculated from the electrical data can also be determined. The series resistance for vacuum annealed sample 1 at the experiment end can be read directly from Figure 6.4 to 460 Ω. Insertion into an expression identical to Equation 6.5 gives

$$A_{v,el,1} = \frac{\left(\frac{1}{4\sigma \cdot R_s}\right)^2}{4} \cdot \pi = 0.36 \text{ mm}^2 \tag{6.7}$$

As for the reference sample a mapping of impurity elements were also performed for comparison between the reference sample 1 and vacuum annealed sample 1. The mapping of silicon on the surface by focused XPS is shown in Figure 6.11. The silicon signal across the surface is again correlated to the

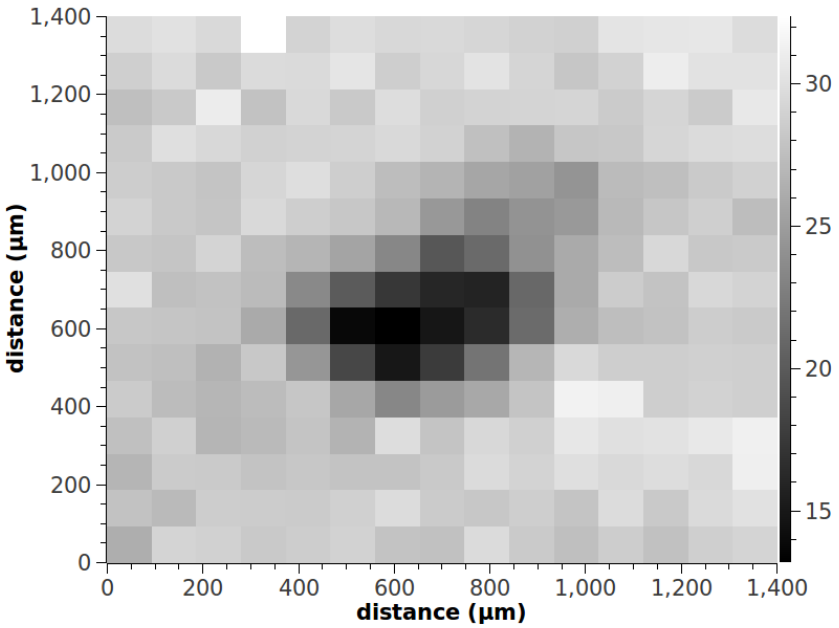

Figure 6.11: The silicon signal across the vacuum annealed YSZ single crystal. As seen for the reference crystal the silicon signal is inversely correlated to the nickel contact area, i.e. the silicon enrichment is primarily on the surface of the YSZ crystal and not in the contact area.

nickel wire contact area resulting in a higher concentration of silicon outside the contact area. Around the nickel contact area a clear silicon segregation

is seen while the silicon signal from the contact area itself is very low. The general appearance of silicon enrichment outside the contact area is similar to the behavior seen on the reference sample 1 as shown in Figure 6.7.

The aluminium mapping of vacuum annealed sample 1 is shown in Figure 6.12. The image is consistent with the image acquired from the mapping of aluminium on reference sample 1 shown in Figure 6.12. Here the alu-

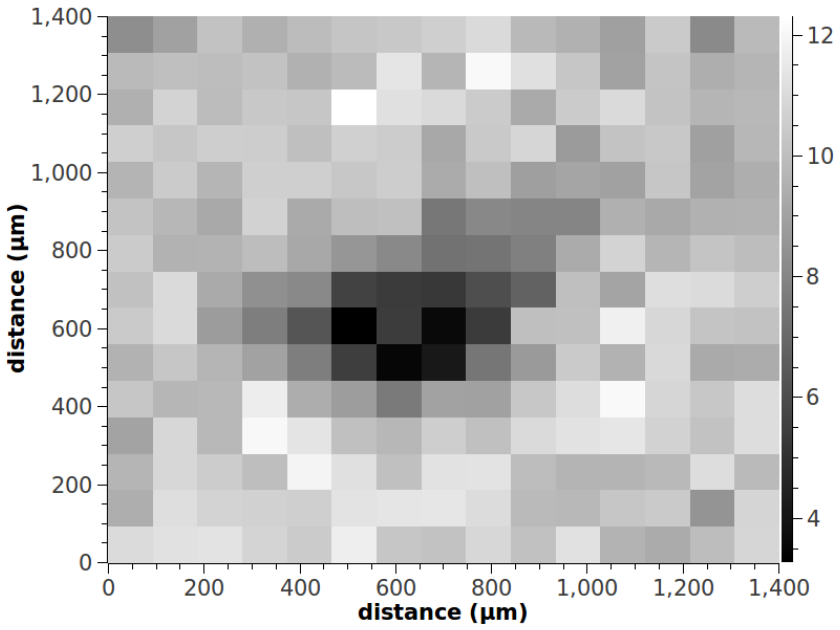

Figure 6.12: Mapping of aluminium on the vacuum annealed YSZ single crystal. As for the silicon mapping the aluminium signal is most pronounced away from the nickel contact area.

minium is concentrated on the surface YSZ crystal compared to inside the contact area of the nickel.

From point spectra acquired in and outside the contact area the concentration of different elements can be determined. In Figure 6.13 the ratio of different elements to zirconium on vacuum annealed sample 2 is shown. Figure 6.13 suggests, just as for the point spectra of the reference sample shown in Figure 6.9, a different element distribution in and outside the contact area. The silicon in and outside the contact area behaves similarly to

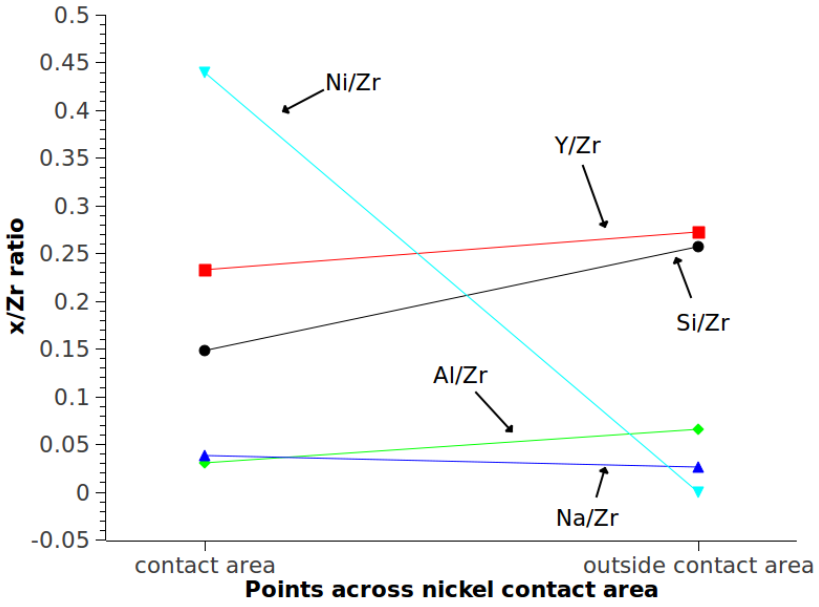

Figure 6.13: Point XPS spectra across the nickel contact area for vacuum annealed sample 2.

the one seen on reference sample 1 in Figure 6.9. The silicon to zirconium ratio in the contact area is approximately 0.1 which is lower than the ratio observed from reference sample where the ratio was found to 0.15. Outside the contact area the silicon to zirconium ratio is 0.24 which is lower than the ratio observed on reference sample 1 which was 0.3.

The aluminium and sodium to zirconium ratio in and outside the contact area has the same trend as the ratio observed from reference sample 1. The aluminium to zirconium ratio is a marginally higher outside the contact area increasing from 0.04 to 0.06. The sodium to zirconium ratio decreases from 0.04 inside the contact area to being not detectable outside the contact area.

The yttrium to zirconium ratio follows the same trend as seen from reference sample 1. From a value of 0.24 inside the contact area the yttrium to zirconium ratio increases to 0.26 outside the contact area which is a smaller increase compared to the ratios on reference sample 1.

The nickel to zirconium ratio is clearly higher in the contact area on the

vacuum annealed sample 1 than on reference crystal 1. Inside the contact area on vacuum annealed sample 1 the nickel to zirconium ratio is 0.44 compared to 0.15 on reference crystal 1.

Several point spectra were also acquired on reference crystal 2 and vacuum annealed sample 2.

In Figure 6.14 the ratio of different elements to zirconium as a function of position on the sample is shown. The point spectra points are denoted $P(X)$ where X goes from 1 to 5. P1 is outside the contact area and is representative of the surface composition outside the contact area. P2 is on the rim of the contact area while P3 is from the center of the contact area. P4 and P5 are the mirrored points of P2 and P1, respectively. P4 is hence a spectrum from the rim opposite to P2 while P5 is a spectrum from the outside the contact area which is on the other side of the contact area from P1.

The trend seen from both reference sample 1 and vacuum annealed sample 1 in Figure 6.9 and 6.13, respectively, is reproduced on reference crystal 2. The silicon to zirconium ratio in the contact area is lower than the ratio observed outside the contact area. The ratio outside the contact area (P1) is 0.32 whereas the ratio in the center of contact area (P3) is 0.28 and then increases on the other side of the contact area (P5) to 0.34. The overall trend of greater silicon enrichment outside the contact area compared to inside the contact seen from the mapping of reference crystal 1 and vacuum annealed sample 2 is hence reproduced by the point spectra acquired from reference crystal 2.

The aluminium to zirconium ratio profile acquired from point spectra across contact area suggests very little difference from outside to inside the contact area. The ratio outside the contact area in P1 is 0.07 and increases slightly towards the center of the contact area (P3) where a ratio of 0.09 is found. The ratio then drops off in the rim point (P4) to 0.05 and finally increases to 0.1 outside the contact area (P5).

The sodium to zirconium ratio outside the contact area (P1) is 0.07 which was also found for aluminium in P1. Unlike the aluminium, however, the sodium decreases towards the contact area center were a ratio of 0.04 is found. Outside the contact area in P5 the sodium to zirconium ratio increases

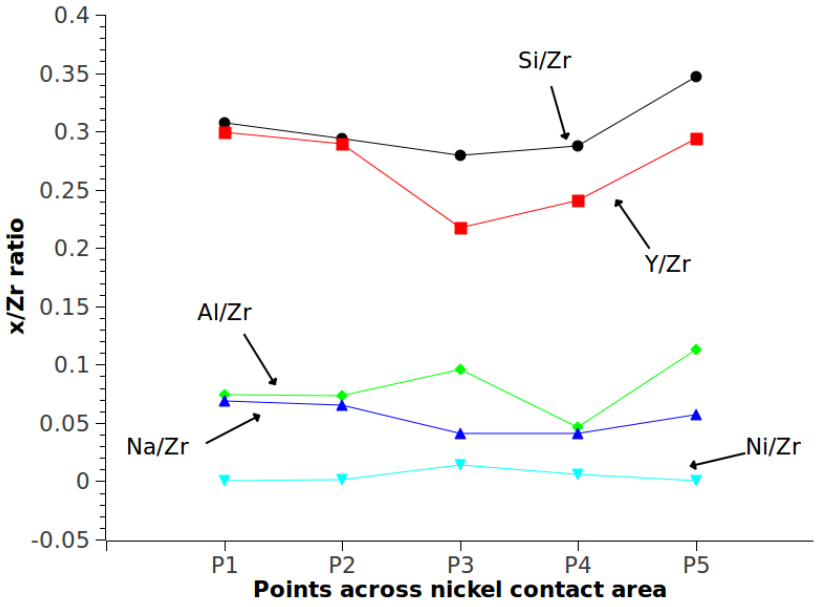

Figure 6.14: Point XPS spectra across the nickel contact area for reference sample 2. P1 and P5 are points outside the contact area, P2 and P4 are on the rim ridge of the contact area while P3 is in the center of the contact area.

slightly from the 0.04 in the center of the contact area to 0.05 outside the contact area.

The yttrium to zirconium ratio is 0.3 in P1 outside the contact area which is higher than the ratios found from reference sample 1 and vacuum annealed sample 1 which was found to 0.28 and 0.26, respectively. In the center of the contact area (P3) the yttrium to zirconium ratio decreases to 0.2 and then increases to 0.28 outside the contact area (P5).

Nickel could not be detected outside the contact area resulting in a ratio of 0 in the points P1 and P5, respectively. A small enrichment of nickel in the surface layers was found in the center of the contact area where a ratio of 0.01 was calculated. The nickel enrichment in the contact area is consistent with the mappings of nickel from reference sample 1 and vacuum annealed sample 1 shown in Figure 6.6 and 6.10, respectively.

The point spectra quantification of vacuum annealed sample 2 is shown

in Figure 6.15. As for reference sample 2 a series of 5 points were acquired across the nickel contact area. The labeling in Figure 6.15 is hence consistent with the one employed in Figure 6.14, i.e. P1 and P5 are outside the contact area, P2 and P4 are on the rim of the contact area and P3 is in the center of the contact area. As for the reference sample 1, vacuum annealed sample

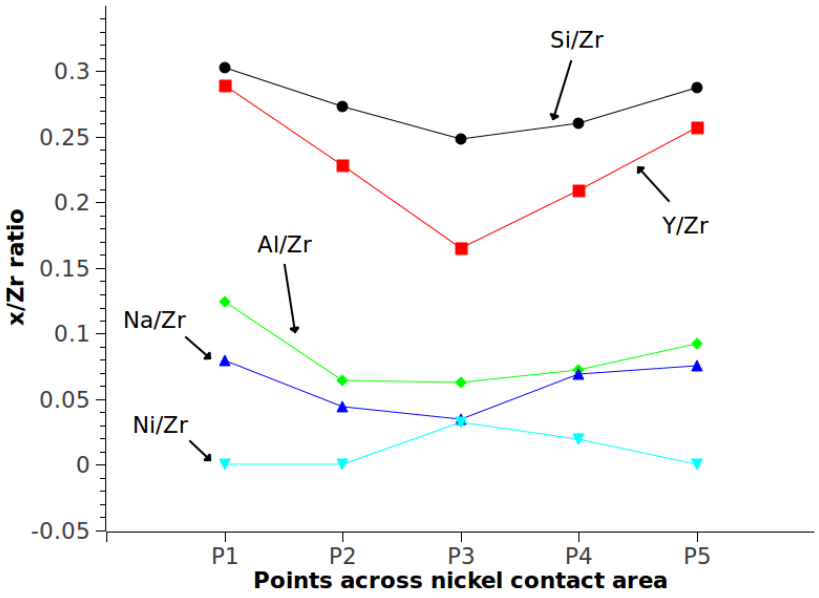

Figure 6.15: Point XPS spectra across the nickel contact area for vacuum annealed sample 2. Notation is the same as used for 6.14.

1 and reference sample 2 silicon and aluminium was observed on the surface of the YSZ single crystal after electrochemical experiments.

The silicon to zirconium ratio outside the contact area (P1) is 0.3 and drops to 0.25 in the center of the contact area (P3). Outside the contact area (P5) the ratio increases to 0.28. The minimum silicon to zirconium ratio observed in the contact area is consistent with point spectra and mapping of silicon acquired from reference crystal 1, vacuum annealed sample 1 and reference crystal 1.

Both the aluminium and sodium to zirconium ratio on vacuum annealed sample 2 showed valley-like appearance as observed for silicon on the same

sample. The aluminium ratio outside the contact area (P1) is 0.13 and decreases to 0.06 in the center of the contact area. On the other side of the contact area the ratio increases again to 0.09 creating the valley-like appearance. The sodium to zirconium ratio is found to 0.08 outside the contact area (P1) and decreases to 0.03 in the center of the contact area (P3). In P5 on the other side of the contact area the ratio increases again to 0.07.

The valley-like composition is even more pronounced for the yttrium to zirconium ratio. Outside the contact area the yttrium to zirconium ratio is 0.28 (P1) which decreases to 0.16 in the center of the contact area (P3). On the other side of the contact area (P5) the yttrium to zirconium increases to 0.25 suggesting yttrium depletion in the contact layer as seen on other samples.

The nickel to yttrium ratio outside the contact area (P1 and P5) is 0 as nickel could not be assigned a peak visible above noise level in the XPS spectra. In the center of the contact area (P3) the nickel to zirconium ratio increases from 0 to 0.03.

The nickel contact areas were measured by focused XPS on reference sample 1 and vacuum annealed sample 1. The contact areas were determined by both geometrical calculations based on the mapping of the contact areas performed by focused XPS and by the recorded series resistances which can be related to the contact area by the Newman formula. In Table 6.1 the determined contact areas for reference sample 1 and vacuum annealed sample 1 is shown. Both electrical calculated contact areas of the two different samples have a value that is close the contact area determined from the focused XPS data. This suggests that the electrical contact area is very close to the geometrical nickel contact area.

The series resistance on all samples tended to decrease with experiment time as shown in Figure 6.4. This is presumably due to the load on the nickel wire from the copper weights pressing the nickel towards the surface and the softening of the nickel wire at high temperatures. Both of these effects will tend to increase the nickel contact area with time decreasing the measured series resistance resulting in the behavior observed in Figure 6.4.

Table 6.1: The measured contact area by XPS and the calculated contact area from the Newman formula.

Sample	A_{geo}	A_{elec}	Dev.
Unit	mm^2	mm^2	%
Reference sample 1	0.45	0.46	2
Vacuum annealed sample 1	0.46	0.36	22

The time evolution of the polarization of reference samples and vacuum annealed samples show very different trends as shown in Figure 6.5. Reference sample 1 shows an initial decrease after the first 30 hours of experiment with a subsequent small increase from 30 hours to experiment end (90 hours). Reference crystal 2 has an initial high polarization resistance of 340 kΩ. Unlike reference crystal 1 there is no initial drop in the polarization resistance. Within the first 60 hours of experiment the polarization resistance fluctuates around the initial 340 kΩ from 130 kΩ to 460 kΩ. From 60 hours and onward a general increase in the polarization resistance is seen ending at 440 kΩ at the experiment end. The vacuum annealed samples have in general a lower polarization resistance than the reference crystals. Vacuum annealed sample 1 has from experiment start a higher polarization resistance than reference crystal 1. As experiment time progresses the polarization value of vacuum annealed sample 1, however, falls below the polarization resistance measured for reference crystal 1. The polarization resistance measured from vacuum annealed sample 2 remains constant at approximately 40 kΩ throughout the measurement period.

To account for the contact area increase due to nickel creep the area specific resistance (ASR) has been calculated for all four reference samples. The resulting plot is shown in Figure 6.16. The contact area was calculated based on the Newman formula and a conductivity of 0.08 S/cm was used. The ASR resistance of the four samples follow the same trend as seen for the polarization resistance suggesting that fluctuations in the polarization

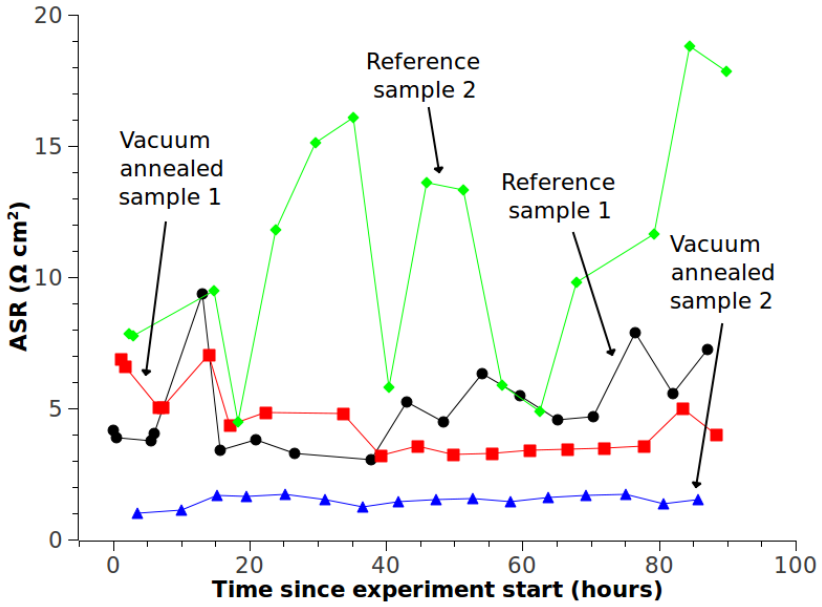

Figure 6.16: Area specific polarization resistance for the reference samples and vacuum annealed samples. Vacuum annealed sample 4 has a consistently lower ASR compared to the reference samples.

resistance for the four samples cannot be attributed to fluctuations in the series resistance.

Generally the polarization resistance of the two reference samples is very fluctuating with especially reference sample 2 showing large fluctuations. Both of the vacuum annealed samples seems to have more stable polarization resistances with time with vacuum annealed sample 2 being especially stable. The large fluctuations in polarization resistance can be assigned to differences in the morphology around the contact area and hence also the amount of impurities present. Following this argument the interface of the vacuum annealed samples should then have smaller changes to the morphology and a more constant amount of impurities with time.

By direct comparison the ASR of reference sample 2 and vacuum annealed sample 2 has approximate values of $15\,\Omega{\cdot}\mathrm{cm}^2$ and $1.5\,\Omega{\cdot}\mathrm{cm}^2$ resulting in a factor of 10 between the best of the vacuum annealed samples and the worst

of the reference samples. From vacuum annealed sample 2, which has the lowest ASR, to reference crystal 1, which has the lowest ASR of the reference crystals, there is approximately a factor of 4.

The composition of the surface layers was determined after electrochemical experiments by XPS. By focused XPS mapping of nickel, silicon and aluminium on reference sample 1 and vacuum annealed sample 1 was performed. Quantification in and outside of the contact area on reference sample 2 was performed by point spectra across the contact area where two points were taken outside the contact area, two points in the rim of the contact area and a point in the center of the contact area. From the mapping images both silicon and aluminium were detected on reference crystal 1 and vacuum annealed sample 1 after electrochemical experiments. For both of the samples the highest concentration of the impurities was found outside the contact area. The silicon enrichment on the surface outside the contact area agrees well the previously reported mapping of the surface after electrochemical experiments [30, 43, 52]. The distribution of aluminium on the surface after electrochemical experiments is also consistent with the mappings observed by other authors [30, 43, 52]. For both reference sample 1 and vacuum annealed sample 1 a larger aluminium signal is observed outside the contact area, cf. Figure 6.8 and 6.12. From the point spectra acquired from reference sample 2 and vacuum annealed sample 2 shown in Figure 6.9 and 6.13 the sodium concentration on the surface is higher outside the contact area than inside the contact area.

The silicon to zirconium ratio in the rim ridge was measured for reference sample 2 and vacuum annealed sample 2. Here the polarization resistance is lower for vacuum annealed sample 2 compared to reference sample 2. Vacuum annealed sample 2 has a lower silicon to zirconium ratio in the rim ridge compared to reference sample 2 (0.27 versus 0.30).

On both vacuum annealed sample 1 and 2 silicon was observed on the surface of the YSZ single crystals after electrochemical experiments. This suggests that these crystals were not free of trace bulk silicon impurities suggesting a too short cleaning time of the crystals. The cleaning time estimate made in Section 5.6.3 was based on surface composition equilibrium time esti-

Table 6.2: The silicon to zirconium ratio of the reference samples (RS) and vacuum annealed samples (VAS) in the contact area (con. area), in the rim ridge and outside the contact area (o. con. area.) after electrochemical experiments compared to the polarization resistance (R_p) and area specific polarization resistance (ASR).

Sample	Si/Zr (con. area)	Si/Zr (rim ridge)	Si/Zr (o. con. area)	ASR (Ω·cm^2)	R_p (kΩ)
RS 1	0.163	-	0.31	8.2	160
VAS 1	0.148	-	0.24	4.6	106
RS 2	0.28	0.30	0.33	20.2	440
VAS 2	0.25	0.27	0.30	1.7	41

mates from Hughes [16]. The segregation rate of silica under UHV conditions could, however, be much slower. Both of the vacuum annealed samples were not annealed in high pressures (>25 mbar) of oxygen atmosphere after the UHV annealing to check for silicon impurities left in the bulk crystal. This was avoided due to the risk of cracking the crystals when annealing in high pressures of gas. The general lower polarization resistance of the vacuum annealed crystals, however, suggest an effect of the applied cleaning.

Chapter 7

Conclusion and Outlook

The chapter preceeding this point have described the experimental work during this Ph.D. project including design and construction of a preparation chamber for studying YSZ single crystals under controlled atmosphere and pressure. Two cleaning strategies of YSZ crystals has been proposed and presented. Furthermore, electrochemical impedance spectroscopy was performed on the surface of YSZ single crystals cleaned by vacuum annealing. The accomplishment and conclusions are the following:

- The segregation of impurities from YSZ single crystals in atmospheric air was studied using ARXPS.
  - ARXPS spectra showed a temperature dependent silicon enrichment of the outermost surface layers of YSZ single crystals after annealing at elevated temperatures.
  - The amount of silicon on the surface increased with temperature in the interval of 500 °C–1100 °C
- A cleaning strategy using strontium zirconate as a getter for silicon and aluminium was presented.
  - The YSZ single crystals were heat treated at 1450 °C with strontium zirconate applied to the external surface of the crystal.

  - After heat treatment the surface of YSZ single crystals showed ball-sectioned features as seen by SEM and AFM.
  - The composition of the features determined by EDS showed large amounts (9–12 at.%) of aluminium and silicium.

- YSZ single crystal was annealed under controlled atmosphere and pressure.
  - A UHV addendum interfaced to existing UHV equipment was built including transfer systems between three UHV chambers and sample holders to interface the YSZ single crystals.
  - The YSZ single crystals were reduced to a dark brown/black color when annealed in UHV. The crystal could be reoxidized by increasing the partial pressure of oxygen in the chamber above 1 mbar.
  - No silicon was found on the samples after annealing in UHV.
  - Silicon was only observed on YSZ single crystals surfaces annealed at high temperatures ($\geq$1100 °C) in high partial pressures of oxygen ($\geq$25 mbar) or water vapor ($\geq$10 mbar).
  - The absence of silicon on the surface after annealing in UHV was attributed to the electrochemical silica decomposition on the surface of the YSZ crystal as shown by enrichment of silicon on a gold foil behind the YSZ crystal while annealed.

- The Ni/YSZ interface was examined by electrochemical impedance spectroscopy.
  - The polarization resistance of especially one vacuum annealed sample showed considerably lower polarization resistance compared to reference samples.
  - Surface characterization after electrochemical experiments by focused XPS showed silicon on the surface of both reference crystals and the crystals attempted cleaned by vacuum annealing.

– The silicon on the YSZ crystals were attributed to too short vacuum annealing times resulting in silicon residues in the bulk of the YSZ crystal after UHV annealing.

7.1 Outlook

Strontium zirconate was used as a getter for silicon and aluminum on the surface of the YSZ single crystals. The strontium zirconate powder can because of this only be applied to the external surface of the crystal. The cleaning of the single crystals by this cleaning method is hence slow and cumbersome. Another more plausible and faster method would be to mix strontium zirconate in YSZ powder and subsequently sinter the powder mix. The strontium zirconate would bind the silicon and aluminium as it segregates from the YSZ crystals in the polycrystal. The experiments performed here could then be used as a starting point of the YSZ to strontium zirconate powder ratio.

Vacuum annealing of YSZ single crystals seem be a fast and efficient way of removing silicon impurities from the bulk YSZ by electrochemical decomposition of silica on the surface of the YSZ crystal. Unfortunately, the desorption of silicon species could not be monitored due to the small solid angle of the mass spectrometer and the low amount of silicon species desorped per time unit. A way to increase the silicon species signal for detection by mass spectrometry is to anneal the YSZ single crystal in a furnace before UHV annealing. A monolayer of silicon segregated during annealing in atmosphere would hence desorp during a.c. annealing. From this experiment a temperature programmed desorption (TPD)-like behavior could be expected. Such an experiment would allow for determination of the desorped species from the YSZ surface.

For further examination of the impurity free Ni/YSZ interface YSZ single crystals will have to be cleaned by vacuum annealed by a.c. voltage. The most straightforward approach to this is to use longer annealing times in vacuum to obtain silicon free YSZ single crystals.

Appendix A

Additional electrochemical impedance spectroscopy spectra

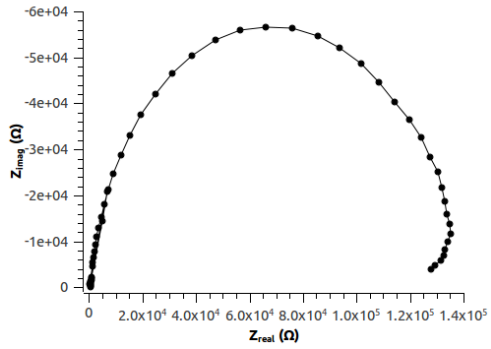

Figure A.1: Reference sample 1 recorded after 0.6 hours

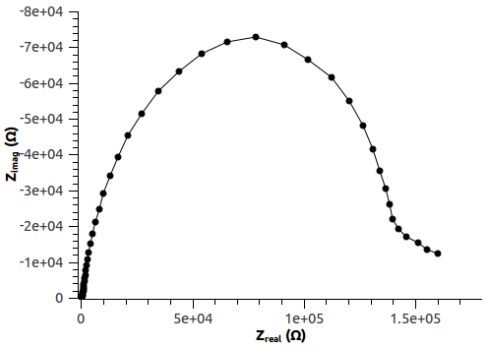

Figure A.2: Reference sample 1 recorded after 87 hours

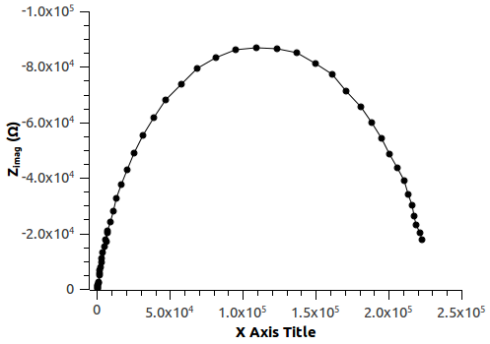

Figure A.3: Vacuum annealed sample 1 recorded after 1 hours

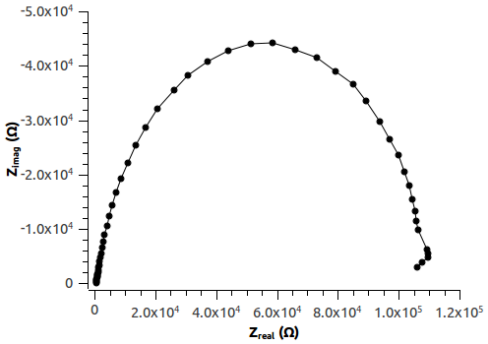

Figure A.4: Vacuum annealed sample 1 recorded after 88 hours

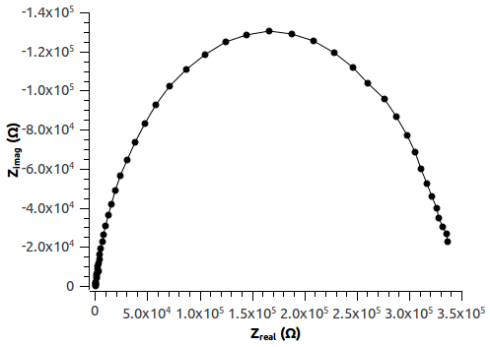

Figure A.5: Reference sample 1 recorded after 2 hours

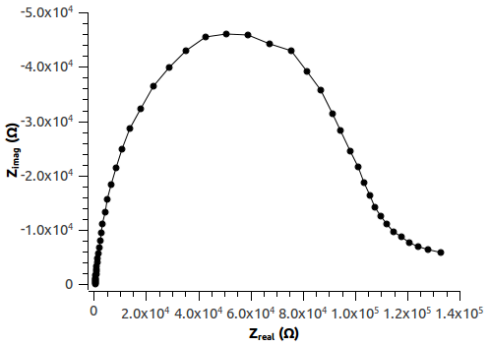

Figure A.6: Reference sample 1 recorded after 90 hours

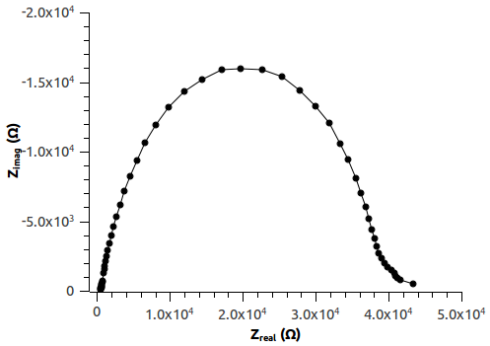

Figure A.7: Vacuum annealed sample 2 recorded after 31 hours

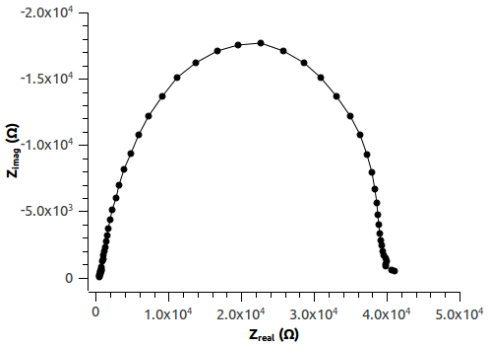

Figure A.8: Vacuum annealed sample 2 recorded after 86 hours

Bibliography

[1] EIA International Energy Statistics, US Energy Information Administration, 2006.

[2] P. Tans, Trends in Carbon Dioxide, NOAA/ESRL, 2011.

[3] W. Grove, Philos. Mag. XIV (1839) 127–130.

[4] D. Oxtoby, Principles of Modern Chemistry, Thomson Brooks/Cole, 5th edition, 2002.

[5] J. Rossmeisl, W. G. Bessler, Solid State Ionics 178 (2008) 1694–1700.

[6] A. Faes, A. Nakajo, A. Hessler-Wyser, D. Dubois, A. Brisse, S. Modena, J. van Herle, J. Power Sources 193 (2009) 55–64.

[7] N. Q. Minh, J. Am. Ceram. Soc. 76 (1993) 563–588.

[8] J. Fergus, J. Power Sources 162 (2006) 30–40.

[9] M. Mogensen, K. Jensen, M. Jørgensen, S. Primdahl, Solid State Ionics 150 (2002) 123–129.

[10] M. Mogensen, J. Høgh, K. V. Hansen, T. Jacobsen, ECS Trans. 7 (2007) 1329–1338.

[11] K. Jensen, S. Primdahl, I. Chorkendorff, M. Mogensen, Solid State Ionics 144 (2001) 197–209.

[12] K. Jensen, R. Wallenberg, I. Chorkendorff, M. Mogensen, Solid State Ionics 160 (2003) 27–37.

[13] K. V. Hansen, K. Norrman, M. Mogensen, J. Electrochem. Soc. 151 (2004) A1436–A1444.

[14] A. Hauch, S. Jensen, J. Bilde-Sørensen, M. Mogensen, J. Electrochem. Soc. 154 (2007) A619–A626.

[15] A. Hauch, S. D. Ebbesen, S. H. Jensen, M. Mogensen, J. Electrochem. Soc. 155 (2008) B1184–B1193.

[16] A. Hughes, J. Am. Ceram. Soc. 78 (1995) 369–378.

[17] A. Bernasik, K. Kowalski, A. Sadowski, J. Phys. Chem. Solids 63 (2002) 233–239.

[18] M. de Ridder, R. van Welzenis, H. Brongersma, S. Wulff, W. Chu, W. Weppner, Nucl. Instrum. Methods Phys. Res., Sect. B 190 (2002) 732–735.

[19] K. Hansen, K. Norrman, M. Mogensen, Surf. Interface Anal. 38 (2006) 911–916.

[20] Y. Liu, S. Primdahl, M. Mogensen, Solid State Ionics 161 (2003) 1–10.

[21] Y. Liu, C. Jiao, Solid State Ionics 176 (5–6) (2005) 435–442.

[22] A. N. Kumar, B. F. Sørensen, J. Am. Ceram. Soc. 83 (2000) 1199–1206.

[23] A. N. Kumar, B. F. Sørensen, Mater. Sci. Eng., A 333 (2002) 380–389.

[24] D. Wood, K. Nassau, Applied Optics 21 (1982) 2978–2981.

[25] B. Savoini, C. Ballesteros, J. E. Muñoz Santiuste, R. González, Y. Chen, Phys. Rev. B 57 (1998) 13439–13447.

[26] S. Badwal, Solid State Ionics 52 (1992) 23–32.

[27] M. Filal, C. Petot, M. Mokchah, C. Chateau, J. Carpentier, Solid State Ionics 80 (1995) 27–35.

[28] A. Madani, A. Cheikh-Amdounia, A. Touati, M. Labidia, H. Boussetta, C. Monty, Sens. Actuators, B 109 (2005) 107–111.

[29] R. Pornprasertsuk, P. Ramanarayanan, C. B. Musgrave, F. B. Prinz, J. Appl. Phys. 98 (2005) 103513–1–103513–8.

[30] M. S. Schmidt, Effects of dopants and trace elements at the Ni/ScYSZ interface, Ph.D. thesis, Risø National Laboratory, 2008.

[31] J. Yates Jr, Experimental Innovations in Surface Science, Springer Verlag New York, Inc., 1998.

[32] H. Lüth, Solid Surfaces, Interfaces and Thin Films, Springer Verlag, 2001.

[33] I. Chorkendorff, J. Niemantsverdriet, Concepts of Modern Catalysis and Kinetics, Wiley-VCH Verlag GmbH & Co, 2003.

[34] D. Woodruf, T. Delchar, Modern Techniques of Surface Science, Cambridge University Press, 2nd edition, 1994.

[35] A. Hughes, S. Badwal, Solid State Ionics 40-1 (1990) 312–315.

[36] S. Badwal, A. E. Hughes, J. Eur. Ceram. Soc. 10 (1992) 115–122.

[37] G. Ingo, G. Padeletti, Surf. Interface Anal. 21 (1994) 450–&.

[38] A. Utz, K. Hansen, K. Norrman, E. Ivers-Tiffée, M. Mogensen, Impurity features in Ni-YSZ-H_2-H_2O electrodes, 2010. Submitted.

[39] M. de Ridder, A. Vervoort, R. van Welzenis, H. Brongersma, Solid State Ionics 156 (2003) 255–262.

[40] M. de Ridder, R. van Welzenis, A. D. van der Gon, H. Brongersma, S. Wulff, W.-F. Chu, W. Weppner, J. Appl. Phys. 92 (2002) 3056–3064.

[41] E. Opila, J. Am. Ceram. Soc. 86 (2003) 1238–1248.

[42] E. Opila, Materials Science Forum 461–464 (2004) 765–774.

[43] J. Høgh, Influence of impurities on the H_2/H_2O/Ni/YSZ electrode, Ph.D. thesis, Risø National Laboratory, 2005.

[44] P. Larsen, M. Mogensen, P. Henriksen, S. Linderoth, M. Chen, International patent WO 2009/027100 A1, 2009.

[45] X. Ye, W. Zhuang, J. Wang, W. Yuan, Z. Qiao, J. Phase Equilib. Diffus. 28 (2007) 362–368.

[46] J. Thomas, H. P. Kumar, R. Pazhani, S. Solomon, R. Jose, J. Koshy, Mater. Lett. 61 (2007) 1592–1595.

[47] T. Ahmad, A. K. Ganguli, Materials Letters 60 (2006) 3660–3663.

[48] K. Martin, R. Sailor, G. McCarthy, ICDD Grant-in-Aid (1992).

[49] A. Patterson, Physical Review 56 (1939) 978–982.

[50] D. Drouin, A. R. Couture, D. Joly, X. Tastet, V. Aimez, R. Gauvin, Scanning 29 (2007) 92–101.

[51] G. Beall, J. Eur. Ceram. Soc. 29 (2009) 1211–1219.

[52] K. Jensen, The Ni-YSZ interface (Structure, composition and electrochemical properties at 1000 °C), Ph.D. thesis, Risø National Laboratory, 2002.

[53] D. Pfoertsch, G. McCarthy, ICDD Grant-in-Aid (1977).

[54] R. Ingel, D. Lewis III, J. Am. Chem. Soc. 69 (1986) 325–332.

[55] P. A. Arifov, M. M. Bulatova, Glass Phys. Chem. 30 (2004) 198–201.

[56] J.-P. Zhang, S.-P. Jiang, J. G. Love, K. Foger, S. P. S. Badwal, J. Mater. Chem. 8 (1998) 2787–2794.

[57] V. R. Paiverneker, A. N. Petelin, F. J. Crowne, D. C. Nagle, Phys. Rev. B: Condens. Matter 40 (1989) 8555–8557.

[58] E. D. Wachsman, N. Jiang, C. W. Frank, D. M. Mason, D. A. Stevenson, Appl. Phys. A 50 (1990) 545–549.

[59] D. I. Torres, S. E. Paje, J. Llopis, G. Morell, R. S. Katiyar, J. Lumin. 72-4 (1997) 724–725.

[60] C. Bonola, P. Camgani, N. Omenetto, G. Samoggia, J. Lumin. 48-9 (1991) 797–799.

[61] D. A. Wright, J. S. Thorp, A. Aypar, H. P. Buckley, J. Mater. Sci. 8 (1973) 876–882.

[62] D. Nagle, V. PaiVerneker, A. Petelin, G. Groff, Mater. Res. Bull. 24 (1989) 619–623.

[63] J. Janek, C. Korte, Solid State Ionics 116 (1999) 181–195.

[64] J.-H. Park, R. Blumenthal, J. Electrochem. Soc. 136 (1989) 2867–2876.

[65] J. A. Nuth, F. T. Ferguson, Astrophysical Journal 649 (2006) 1178–1183.

[66] HSC Chemistry 7 Software, Outotec, 2010.

[67] I. Chorkendorff, Experimental Surface Physics, Technical University of Denmark, 2003.

[68] H. L. Schick, Chem. Rev. 60 (1960) 331–362.

[69] R. A. Gardner, J. Solid State Chem. 9 (1974) 336–344.

[70] J. J. Lander, J. Morrison, J. Appl. Phys. 33 (1962) 2089–&.

[71] J. Tromp, G. Rubloff, P. Balk, F. LeGoues, Phys. Rev. Lett. 55 (1985) 2332–2335.

[72] A. Ishizaka, Y. Shiraki, J. Electrochem. Soc. 133 (1986) 666–671.

[73] A. Wells, Structural Inorganic Chemistry, Oxford Science Publications, 1984.

[74] J. Newman, J. Electrochem. Soc. 113 (1966) 501–503.

List of Symbols

α	Minor diameter
A_{rms}	Root mean square current
β	Line broadening or major diameter
ΔG	Gibbs free energy
ε	Electromotive Force
F	Faraday Constant
γ	Impurity content
I	Current
K	Shape Factor
λ	Wavelength
m	Mass
M	Molar Mass
n	Amount of substance or number of electrons
N	Number
r_e	Equivalent diameter
R_p	Polarization resistance
R_s	Series resistance
ρ	Density
σ	Conductivity
T	Temperature
τ	Cleaning time
θ	Coverage or Bragg angle
V_{rms}	Root mean square voltage

List of Abbreviations

a.c.	Alternating Current
AES	Auger Electron Spectroscopy
AFM	Atomic Force Microscopy
AMU	Atomic Mass Unit
(DP)-CMA	(Double Pass) Cylindrical Mirror Analyzer
EDX	Energy-dispersive X-ray Spectroscopy
EIS	Electrochemical Impedance Spectroscopy
FIB	Focused Ion Beam
GDMS	Glow-Discharge Mass Spectrometry
HAADF	High Annular Dark Field
LEIS	Low-Energy Ion Scattering
LSCF	Lanthanum Strontium Cobalt Ferrite
LSM	Lanthanum Strontium Manganite
OCV	Open Circuit Voltage
QMS	Quadropole Mass Spectrometer
SEM	Scanning Electron Microscopy or Secondary Electron Multiplier
SO(F)C	Solid Oxide (Fuel) Cell
(S)TEM	(Scanning) Transmission Electron Microscopy
TOF-SIMS	Time-of-Flight Secondary Ion Mass Spectrometry
UHV	Ultra High Vacuum
WDX	Wavelength-dispersive X-ray Spectroscopy
(AR)XPS	(Angle Resolved) X-Ray Photoelectron Spectrocopy
XRD	X-ray Diffraction
YSZ	Yttria Stabilized Zirconia

List of papers

Paper 1:

Electrochemical removal of segregated silicon dioxide impurities from yttria stabilized zirconia surfaces at elevated temperatures

T. Andersen, K.V. Hansen, M. Mogensen, I. Chorkendorff

Accepted for publication in Solid State Ionics

Paper 2:

Strontium zirconate as silicon and aluminium scavenger in yttria stabilized zirconia

T. Andersen, K.V. Hansen, I. Chorkendorff, M. Mogensen

Accepted for publication in Solid State Ionics

Electrochemical removal of segregated silicon dioxide impurities from yttria stabilized zirconia surfaces at elevated temperatures

Thomas Andersen[a,*], Karin Vels Hansen[b], Mogens Mogensen[b], Ib Chorkendorff[a]

[a] *Center for Individual Nanoparticle Functionality, Department of Physics, Building 312, Technical University of Denmark, DK-2800 Lyngby, Denmark*
[b] *Fuel Cells and Solid State Chemistry Division, Risø National Laboratory for Sustainable Energy, Technical University of Denmark, DK-4000 Roskilde, Denmark*

Abstract

Here we report on the electrochemical removal of segregated silicon dioxide impurities from Yttria Stabilized Zirconia (YSZ) surfaces at elevated temperatures studied under Ultra High Vacuum (UHV) conditions. YSZ single crystals were heated in vacuum by an applied 18 kHz a.c. voltage using the ionic conductivity of YSZ. The crystals were annealed in vacuum and atmospheres of water or oxygen from 10^{-5} mbar to 100 mbar in the temperature range of 1100 °C to 1275 °C. The surface was after annealing analyzed by X-ray Photoelectron Spectroscopy (XPS) without exposing the crystal to atmosphere between annealing and XPS analysis. Silicon enrichment of the surface was only observed at oxygen and water vapor partial pressures above 25 mbar and 10 mbar, respectively. No silicon was observed on crystals annealed in vacuum and at oxygen and water vapor partial pressures below 10 mbar. The YSZ seems to get partially electrochemically reduced by the a.c. voltage when no oxidation substances are present. The absence of silicon on the surfaces annealed in vacuum or at low oxygen or water vapor partial pressures was attributed to electrochemical reduction of silicon dioxide to volatile silicon monoxide on the YSZ surface. This was demonstrated by silicon enrichment of a gold foil placed behind the YSZ crystal surface while annealed. The results suggest a fast way to clean YSZ for trace silicon dioxide impurities found in the bulk of the cleanest crystals commercially available.

Keywords: yttria stabilized zirconia, silicon dioxide, electrochemical reduction, cleaning

1. Introduction

Yttria Stabilized Zirconia (YSZ) is typically used as electrolyte in Solid Oxide Cells (SOCs) [1, 2] due to its fast ionic transport, chemical inertness and mechanical stability at elevated temperatures. However, as all materials, YSZ invariable contains bulk impurities in trace amounts. Certain intrinsic impurities in the YSZ matrix have a high tendency to segregate to the external surface of single crystals or to grain boundaries of polycrystals through a minimization of the surface free energy of a clean YSZ crystal. The surface free energy of a clean YSZ crystal, which is believed to equal the mechanical energy release rate by fast fracture [3], has been determined to 3.7 J/m^2 for a 8 mol% YSZ crystal [4]. The high surface energy of YSZ creates a potential for segregation of impurities to the surface minimizing the total energy. Segregation of impurities will only happen at elevated temperature where there is sufficient mobility and has been observed at elevated temperatures both in atmospheres of 3 % H_2O in H_2 [5–9] and after annealing in atmospheric air [10–14] when post characterization has been performed with surface sensitive spectroscopies.

The segregation of impurities from the YSZ bulk has been shown to increase the polarization resistance of the anode/electrolyte interface of SOCs. Jensen et al. [6] performed electrochemical electrical impedance spectroscopy measurements of a bent nickel wire pressed against a YSZ electrolyte as a model of the triple phase boundary of a SOC anode. They reported the creation of an impurity ridge around the contact area consisting primarily of silicon dioxide [7]. The accumulated impurity ridge around the contact area between the wire and YSZ surface resulted in a large polarization resistance of the electrochemical reaction [6]. Furthermore, they found a significant lower polarization resistance when using a pure nickel electrode (99.995 %) compared to an impure nickel electrode (99.8 %). Their results suggest that the impurities segregated from the YSZ electrolyte bulk to the surface at elevated temperatures have a significant effect on the polarization resistance of the anode/electrolyte interface in SOCs. Obviously, elimination of these impurities in the

*Corresponding author. Center for Individual Nanoparticle Functionality, Department of Physics, Building 312, Technical University of Denmark, DK-2800 Lyngby, Denmark. Tel.: +45 45253137.
Email address: thomas.andersen@fysik.dtu.dk (Thomas Andersen)

YSZ bulk is mandatory for gaining understanding of the losses associated with using YSZ electrolytes in SOCs.

This study focuses on the silicon enrichment of YSZ surfaces observed after annealing. The crystals have been studied under Ultra High Vacuum (UHV) conditions as a function temperature, atmosphere and pressure. Previous studies of segregation in YSZ have been performed after annealing the crystal in atmospheric air or at high temperatures in hydrogen and water to mimic realistic operating condition of SOCs. None of these studies, however, investigate the segregation of impurities in detail under controlled conditions. Understanding the silicon enrichment of YSZ surfaces can help improve the cleaning procedure of YSZ to eliminate silicon trace impurities in YSZ with the aim of studying extremely clean interfaces of SOCs.

Here we report on atmosphere, temperature and pressure dependent surface enrichment of silicon on YSZ single crystals upon heating in UHV using a.c. current.

2. Experimental

2.1. YSZ single crystals

YSZ single crystals (100) (9 mol.% Y_2O_3), i.e. $Zr_{0.84}Y_{0.16}O_{1.92}$, with dimensions of 5 x 5 x 2 mm^3 with two grooves on each side of the crystal was purchased from MTI Crystals. The grooves on the crystal were 0.5 mm wide and deep and placed on opposing sides of the crystal, cf. Figure 1.

The as-received crystals have from the manufacturer received a RCA (Radio Corporation of America) clean. The RCA cleaning procedure has three major steps used sequentially. First an organic clean with removal of insoluble organic contaminants with a 5:1:1 H_2O:H_2O_2:NH_4OH solution. Next an oxide strip using a diluted 50:1 H_2O:HF solution is performed. Finally an ionic clean using a solution of 6:1:1 H_2O:H_2O_2:HCl.

Nominal purity of the as-received crystal is 99.9 % and was checked by Glow-Discharge Mass Spectrometry (GDMS). The impurity content of selected elements determined from GDMS is shown in Table 1.

X	Con.	X	Con.	X	Con.	X	Con.	X	Con.	X	Con.
Zn	<0.05	K	0.12	Se	<0.5	Cs	<0.5	Lu	0.22	Be	<0.05
Y	Matrix	Ba	0.1	Hf	1.7 wt.%	B	0.01	Cr	1.4	Zr	Matrix
Ta	<5	O	Matrix	Mn	0.27	Nb	<0.5	Ce	1.2	W	0.45
Fe	5.5	Mo	0.31	Pr	10	Re	<0.5	Na	0.72	Co	0.33
Ir	<0.5	F	<0.5	Mg	1.5	Ni	0.18	Rh	<0.5	Sm	0.48
Al	3.5	Cu	0.39	Pd	<5	Eu	3	Pt	<1	**Si**	**18**
Sr	<0.1	Gd	<0.5	Au	<5	P	<0.01	Ga	<0.05	Cd	<200
Hg	<0.5	S	0.12	Ge	<1	In	Binder	Dy	2.9	Tl	<0.1
As	<5	Sn	2.9	Ho	0.55	Pb	<0.05	Ca	12	Br	<0.5
Er	2.1	Bi	<0.05	Cl	0.36	Rb	<0.5	Te	<0.5	Tm	0.06

Table 1: GDMS analysis of selected elements of an as-received YSZ single crystal. X denote element columns while Con. denotes concentration columns. The crystal was grinded to powder and indium was used as a binder to obtain the required dimensions of the sample for GDMS. Unit is ppm by weight.

Two platinum wires of approximately 2 cm in length, used as electrodes, were inserted into the grooves of the crystal. The electrodes were mounted to a sample holder such that the wires could be connected to a suitable a.c. power supply. The sample holder could be parked either in a preparation chamber, where the crystal was heated, or in an analysis chamber where the surface composition was determined by X-Ray Photoelectron Spectroscopy (XPS).

After treatment in the preparation chamber the crystals were transferred under vacuum to the analysis chamber where XPS and Auger electron spectroscopy (AES) are available. The transfer was achieved by two perpendicular special designed linear motions transferring the sample by the groove in the top plate of the sample holder and by the sample pins. By transferring the sample in vacuum from the preparation chamber contamination between annealing and analysis was avoided. A schematic of the UHV setup consisting of the preparation chamber, the analysis chamber and the two perpendicular linear drives used for transfer between the two chambers is shown in Figure 2.

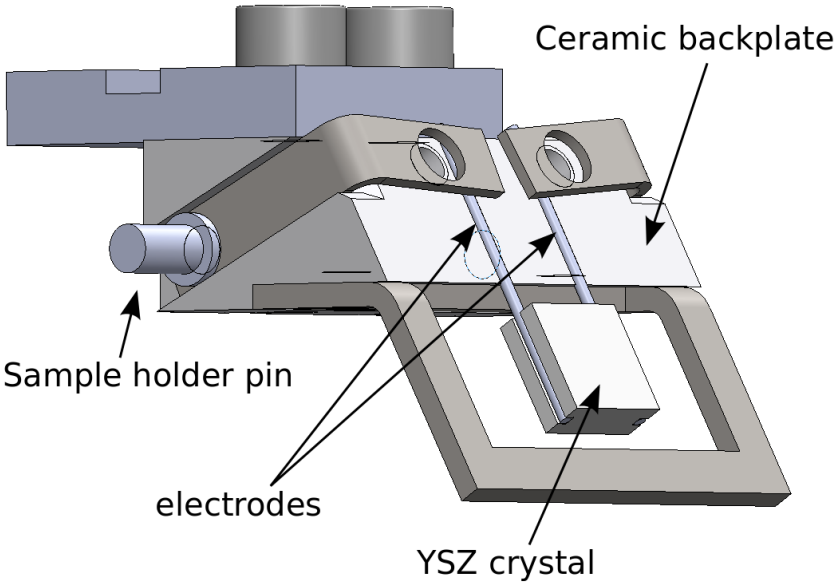

Figure 1: Illustration of the YSZ single crystal mounted in the sample holder. Two platinum electrodes were inserted into grooves of the crystal. Biasing of the sample for heating was performed by biasing the sample holder pins which are connected to feedthroughs when parked in the preparation chamber (color online).

2.2. Heating of YSZ single crystals

Heating of the crystals under UHV was achieved by a 18 kHz a.c. voltage across the crystal supplied from a Topward 8102 function generator and amplified by a LD PA1000 hi-fi amplifier. To obtain an appreciable ionic conductivity and start the heating the YSZ single crystal was preheated by a Philips 6958/10H 250 W halogen lamp operated at 10 A and 22 V which was moved to a distance of 1 mm from the sample surface by a linear drive. While heating the crystal by the halogen lamp the a.c. voltage across the crystal was increased slowly from 0 V_{rms} to approximately 15 V_{rms} as measured by a Tektronix 2012B oscilloscope to prevent current run away. While the voltage was ramped the current through the crystal increased from 0 A_{rms} at room temperature to approximately 1 A_{rms} at 1100 °C. When the current through the crystal exceeded 0.3 A_{rms} the halogen lamp was turned off and retracted using the linear drive. Using this method the crystal temperature could be controlled by the supplied voltage and sustained for several days.

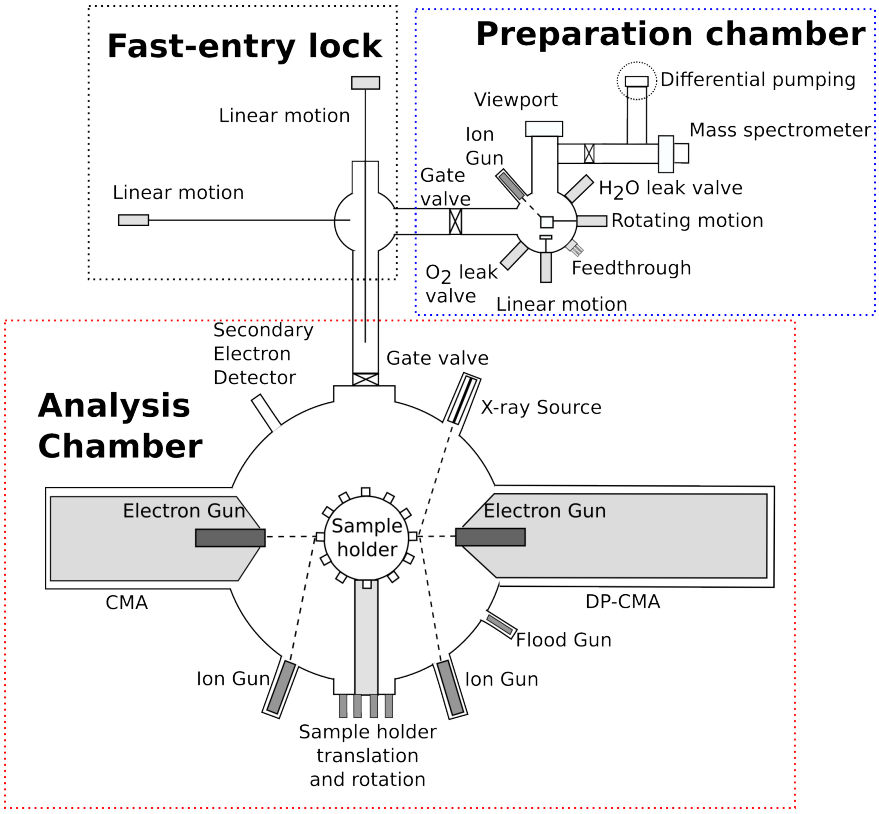

Figure 2: Schematic of the UHV equipment used. The YSZ single crystals were annealed in the preparation chamber under either UHV conditions, in partial pressures of water vapor or in partial pressures of oxygen. After treatment the crystal was transferred in UHV in the sample holder by two perpendicular linear drives to the analysis chamber were either XPS or AES analysis was performed (color online).

The temperature of the crystal was measured by a pyrometer through the viewport of the preparation chamber. The temperature was cross referenced by the temperature calculated from conductivity measurements of a reference YSZ single crystal measured by an ex-situ electrochemical impedance spectroscopy setup and is is highly reproducible.

The crystal was heated either in vacuum, scientific grade oxygen or Millipore water containing atmospheres. To avoid cracking of the crystal due to thermal stress introduced by the convective cooling in gases, heating was initially started under vacuum. If needed, gases were subsequently introduced slowly while the crystal was hot avoiding large thermal gradients across the crystal resulting in fracture. The total pressure in the chamber was varied by leak valves in the range $1{\cdot}10^{-9}$ mbar to 100 mbar. When the pressure in the

chamber was above $1{\cdot}10^{-5}$ mbar the pumping from two turbomolecular pumps were closed by gate valves and the chamber was backfilled with gas until the desired final pressure was reached. All crystals were annealed either in vacuum, oxygen or water containing atmospheres for a minimum of 10 hours. This was done to reach steady state of the surface composition at any given temperature, pressure and atmosphere.

Pressures below $1{\cdot}10^{-5}$ mbar were measured by a standard ion gauge while pressures in the range from 1 mbar to 100 mbar were measured by a Baratron capacitor gauge.

Gases applied during heating was not pumped out until the sample was cooled down and had reached room temperature. This was done to avoid any change in surface composition as a result of atmosphere composition and pressure.

For comparison additional crystals were heated ex-situ in a furnace in atmospheric air. The crystals were heated to temperatures ranging from 500–1100 °C for 10 hours. All the crystals annealed in an ex-situ furnace were protected by a platinum foil during heating to avoid any cross contamination from the furnace. The crystals were after annealing transported in the platinum foil and mounted on a sample holder and inserted into the analysis chamber through a fast-entry lock for XPS analysis.

2.3. XPS characterization

XPS spectra of samples annealed in the preparation chamber were acquired on a PHI Model 25–260 AR analyzer with an aluminum magnesium dual anode setup. The samples were mounted on a sample holder tilted 30° compared to the sample normal. The entire YSZ surface was irradiated with non-monochromatized Al K_α X-rays with a primary energy of 1486.7 eV. The lateral resolution of the analysis is estimated to 5 mm.

Angle Resolved X-ray Photoelectron Spectroscopy (AR-XPS) was used to determine the surface composition of samples annealed ex-situ. The spectra were acquired using a Thermo Scientific Theta Probe instrument. The X-ray source is monochromatized Al K_α (1486.7 eV) and the analyzer entrance accepts electrons emitted between 20° and 80° to the surface normal. For analysis of the YSZ crystals an X-ray beam size of 400 μm was used.

Peak identification, fits and concentration calculations were done in casaXPS using either

the as-implemented Shirley or linear background and sensitivities. All XPS spectra were referred to the adventitious carbon 1s line at 284.6 eV in post processing of the spectra due to charging of the crystal during X-ray irradiation. The charging of the crystal was, however, minimized by using a flood gun during X-ray exposure.

All crystals were analyzed by XPS both before and after treatment. Initially survey spectra were acquired from 1100–0 eV binding energy and with 100 eV pass energy. Any elements of interest detected in the survey scan were examined further by a narrow scan (50 eV pass energy, 0.4 eV step size) in the region of interest. If needed, the as-received crystals were cleaned by sputtering with argon ions prior to any treatment.

2.4. Analysis of species desorped from the YSZ crystal

To measure the species evaporated from the YSZ surface while annealed two different approaches were pursued. A mass spectrometer mounted approximately 2 cm from the YSZ surface was used to study the gas composition in the preparation chamber as a function of time. A second approach using a gold foil behind the YSZ sample was also employed. The gold foil acted as a cold finger compared to the hot YSZ crystal collecting species desorped from the YSZ surface while annealed.

Mass spectra were acquired with a cross beam Balzers QMA125 with QME125 electronics interfaced to a computer with homebuilt electronics. Mass (amu) to charge (coulomb) ratios of 28, 32, 44 and 60 corresponding to silicon, molecular oxygen, silicon monoxide and silicon dioxide were measured while annealing the crystal. Full mass scans from 0–100 mass to charge ratio were also acquired with regular intervals.

AES characterization was performed on the gold foil (99.99 % pure) inserted behind the YSZ single crystal taking advantage of the technique's high lateral resolution. AES was not possible on the YSZ surface due to its insulating nature. The distance between the foil and crystal was approximately 1 mm. The gold foil was inserted as-received, but cleaned with ethanol and acetone, behind the crystal.

AES spectra were acquired on a PHI Model 25–110 analyzer. Electrons for excitation were produced by a lanthanum hexaboride crystal. The acceleration energy during acquisi-

tion was in all cases 5 kV. Typically an area of 150 x 150 μm^2 was irradiated with 0.5 μA corresponding to current density of 22 A/m^2. Survey scans were acquired from 30–2000 eV kinetic energy with a step size of 1 eV.

3. Results

3.1. Annealing of YSZ singles crystals in ex-situ furnace

YSZ single crystals were annealed in a furnace at temperatures from 500 °C to 1100 °C for 10 hours in atmospheric air. This was done to observe silicon enrichment on the outermost surface of as-received YSZ single crystals. The results from ex-situ annealing could then be used as reference for the crystals annealed under controlled atmospheres in the UHV setup.

The data obtained from AR-XPS of reference samples heated in atmospheric air is presented in Figure 3. Data obtained at 20° with respect to the surface normal has the lowest surface sensitivity while data acquired at 80° with respect to the surface normal measurements have the highest surface sensitivity.

As seen from Figure 3 the silicon concentration in the surface layers increased as a function of temperature. At 500 °C a very low silicon to zirconium ratio was found indicating low segregation rate. It is observed that the silicon to zirconium ratio is increased with temperature in the temperature range used. After annealing at 1100 °C the silicon to zirconium ratio is 0.1 at 20°. Furthermore, the angle resolved data show a clear enrichment of silicon in the outermost surface layers of the YSZ single crystal. Here the silicon to zirconium ratio is increased from 0.1 with an analyzer angle of 20° to 0.5 with an analyzer angle of 80° after annealing at 1100 °C. The yttrium to zirconium ratio stays almost constant with temperature with a value of approximately 0.3 which is higher than the expected 0.2 for the stoichiometry of as-received crystals.

3.2. Annealing YSZ single crystals in UHV

YSZ single crystals were also annealed in air in the preparation chamber. For this purpose the preparation chamber was vented to atmospheric air. After annealing the YSZ

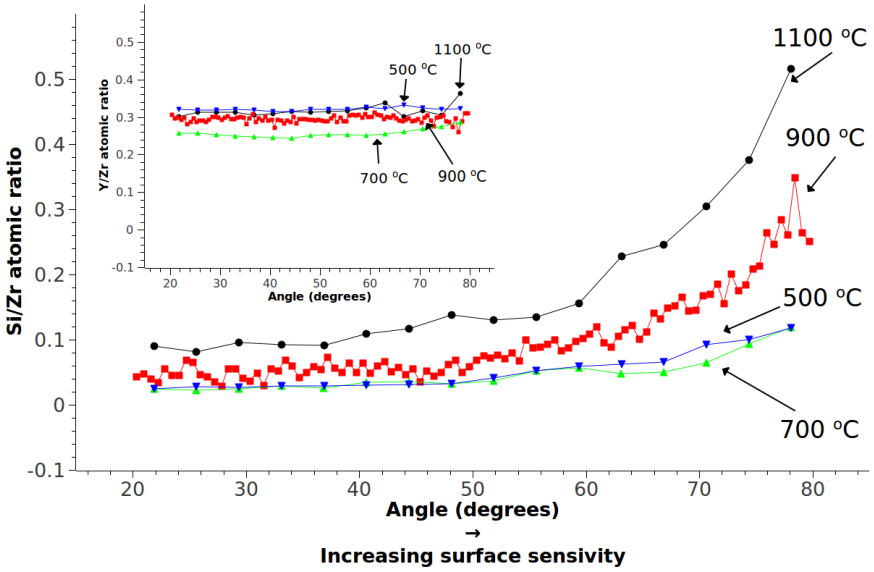

Figure 3: Si/Zr and Y/Zr (inset) ratios determined by AR-XPS of YSZ single crystals annealed in a range of temperatures for 10 hours in air. The angle is defined relative to the surface normal meaning higher surface sensitivity with higher angle. A clear enrichment of silicon in the outermost surface layers is seen for all annealing temperatures (color online).

single crystal in the preparation chamber is was pumped down. The sample was subsequently transferred under vacuum to the analysis chamber where XPS analysis was performed. From the survey scan from the YSZ single crystal oxygen, zirconium, yttrium, silicon and platinum were detected. The platinum on the surface was not attributed to a platinum enrichment of the surface but is present in the spectrum due to the low lateral resolution of the XPS equipment. The binding energy scans of the silicon 2p peak is shown in Figure 4. Here a clear enrichment of silicon on the YSZ surface is observed in air consistent with results from annealing ex-situ in a furnace. After pump down the YSZ single crystals were also annealed in the preparation chamber under UHV conditions. XPS results from the binding energy region of 108 - 98 eV after annealing in UHV at 1100 °C and 1250 °C are also shown in Figure 4 for comparison. At both 1100 °C and 1250 °C no silicon was observed on the surface after annealing. Further increasing the annealing time to 48 hours at both 1100 °C and 1250 °C under UHV conditions showed no difference from spectra acquired after shorter

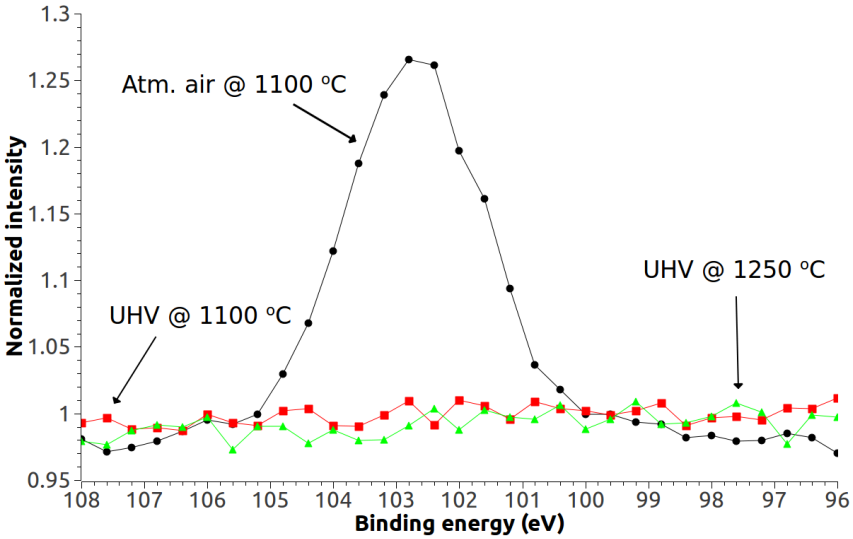

Figure 4: Comparison of silicon 2p spectra obtained after annealing in air and UHV, respectively. When annealing under UHV conditions no silicon enrichment was observed on the YSZ surface (color online).

annealing times.

3.3. Annealing in oxygen atmospheres

A clear oxygen partial pressure and temperature dependency of silicon enrichment of the YSZ surface was observed as shown in Figure 5. Silicon was observed after annealing in 25 mbar oxygen and 1250 °C or 100 mbar oxygen and 1100 °C. The binding energy of the silicon 2p peak indicated, in both cases, an oxidized state of silicon. After annealing at lower pressures and temperatures no silicon was observed on the surface of the YSZ single crystal.

3.4. Annealing in water vapor

The surface composition after annealing in water vapor is presented in Figure 6. A pronounced silicon peak is seen after annealing in 10 mbar water partial pressure at 1100 °C. The area of the silicon 2p peak after annealing in water vapor is very close to the area found after annealing in 100 mbar oxygen at 1100 °C (12.1 versus 12.2) suggesting a comparable silicon enrichment at lower temperature and vapor pressure of water compared

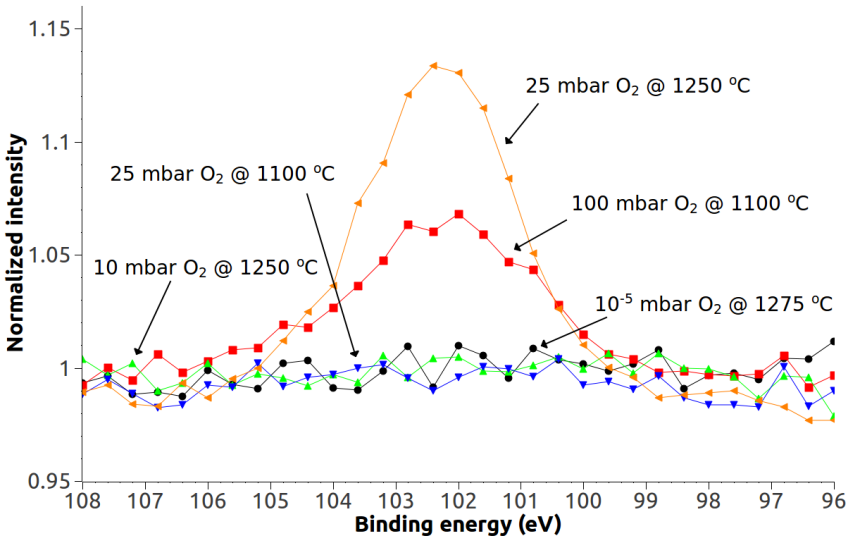

Figure 5: XPS spectra of the silicon 2p binding energy as a function of oxygen partial pressure and temperature. Silicon enrichment of the surface of YSZ single crystals is both temperature and oxygen partial pressure dependent (color online).

to oxygen. Silicon was not observed on samples treated in water vapor pressure below 10 mbar at any temperature.

3.5. Desorption from the YSZ crystal

The quadropole mass spectrometer was used to monitor the gas composition in real time while the YSZ single crystals was annealed. It was not possible, however, to observe any signal at masses 28, 44 or 60 which could be attributed to silicon, silicon monoxide or silicon dioxide. For masses 28 and 44 the signal was difficult to detect due to the overlap with carbon monoxide and carbon dioxide which are typical residue gases in UHV. Furthermore, the solid angle subtended by the mass spectrometer, even with the mass spectrometer filament approximately 2 cm from the sample surface, was very small due to the high sticking coefficient of silicon species on surfaces at lower temperatures than the YSZ crystal. The overlap of masses and the small solid angle of the mass spectrometer combined with the expected low species desorption rate, due to the slow rate of silicon segregation in YSZ, it was not possible to observe any silicon species with the mass spectrometer.

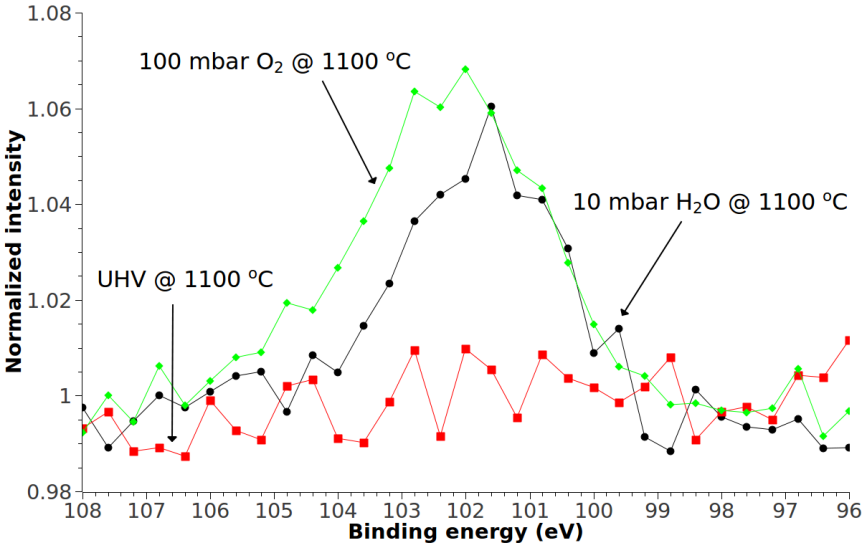

Figure 6: Comparison of silicon enrichment after annealing in 10 mbar water vapor, 100 mbar oxygen partial pressure and under UHV at 1100 °C (color online).

Instead a gold foil was inserted behind the YSZ single crystal before annealing in UHV. The use of a gold foil greatly improved the signal to noise ratio due to the time integration of the evaporated species compared to the time resolved mass spectrometer and the large surface area of the gold foil compared to the YSZ single crystal.

The foil was analyzed by AES before heating the crystal. The only impurities found on the crystal was carbon and sulphur. After annealing the YSZ single crystal a clear silicon enrichment on the gold foil was observed as shown in Figure 7. Here the high kinetic energy AES transition (KLL) of silicon was chosen to avoid overlap with gold Auger lines at lower kinetic energies. The profile of the silicon observed on the surface is characteristic of oxidized silicon.

3.6. Blackening of the YSZ crystal

During ramping of the a.c. voltage across the crystal to initiate heating it was reduced to a dark brown/black color while in UHV or at low oxygen or water vapor partial pressures. By increasing the oxygen partial pressure above 1 mbar while annealing the crystal it was reoxidized obtaining its original transparency as observed by eye. By lowering the oxygen

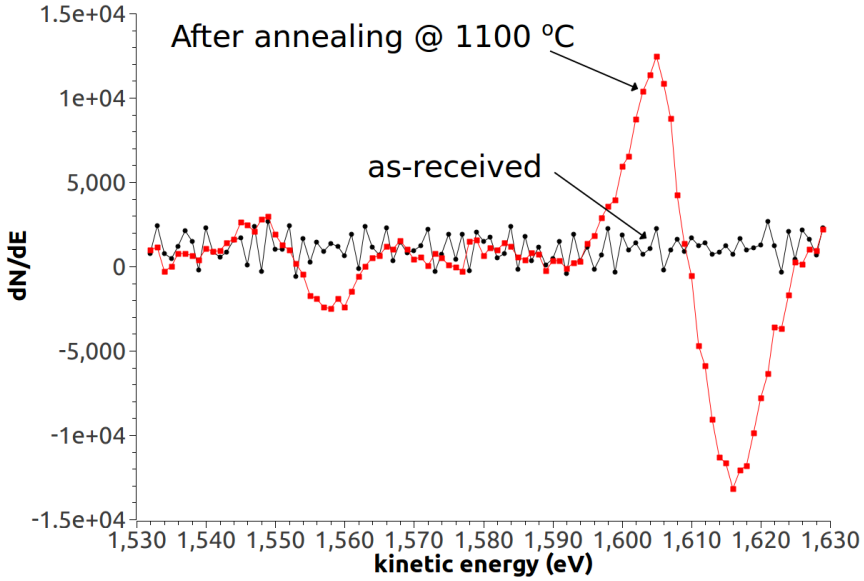

Figure 7: AES spectra from the silicon (KLL) kinetic energy region of the gold foil behind the YSZ single crystal taken before and after annealing of the YSZ single crystal, respectively. A clear silicon enrichment of the gold foil is seen after annealing of the YSZ crystal at 1100 °C (color online).

partial pressure in the chamber while annealing the crystal it was again reduced. The oxidation and reduction of the crystal could be controlled by the oxygen partial pressure in the chamber and was fully reversible.

4. Discussion

The AR-XPS results of the as-received single crystals annealed ex-situ in air showed an increase of the silicon to zirconium ratio on the surface of the YSZ single crystal. The silicon enrichment on the surface of the YSZ crystal was increasing with temperature from 500 °C to 1100 °C. The segregation of silicon and the silicon to zirconium ratio on the surface after annealing agree well with data obtained by Hughes [11]. He found a silicon to zirconium ratio of approximately 0.25 after 200 minutes annealing at 1100 °C using an analyzer entrance angle of 70° with respect to the surface normal. In the present study the ratio was 0.28 at 70°. This result demonstrates segregation of silicon from the YSZ bulk to the surface as expected due to minimization of the surface free energy. The high yttrium

to zirconium ratio of 0.3 observed by AR-XPS is much higher than the expected 0.2 from the stoichiometry of the as-received crystal. The yttrium to zirconium ratio is furthermore constant as a function as angle in the AR-XPS spectra, c.f. Figure 3. This is in contrast to the ratios obtained by Hughes [10] where an enrichment of yttrium was found in the surface layers after annealing. The general high yttrium to zirconium ratio can be attributed to a preannealing from the manufacturer causing yttrium segregation. Yttrium segregation at elevated temperatures has also been observed experimentally by other authors [11, 13, 15] to near surface layers. The AR-XPS results presented here, however, suggest constant yttrium content as a function of depth on the length scale observed by AR-XPS. Presumably this is caused by the treatment from the manufacturer. Both yttrium oxide and silicon dioxide has segregated to the surface or near surface layers during the annealing from the manufacturer. However, silicon dioxide has after this annealing been removed by the hydrofluoric etch during the RCA clean.

Atmosphere	Pressure (mbar)	Temperature (°C)	Si/Zr	Y/Zr
Air (nominal, no annealing)	1010	25	0	0.20
Air (ex-situ)	1010	1100	0.39	0.32
Air (UHV setup)	1010	1100	0.22	0.38
UHV	$<10^{-9}$	1100	0	0.29
UHV	$<10^{-9}$	1250	0	0.32
O_2	$1{\cdot}10^{-5}$	1275	0	0.28
O_2	10	1250	0	0.29
O_2	25	1100	0	0.30
O_2	25	1250	0.12	0.34
O_2	100	1100	0.05	0.33
H_2O	10	1100	0.06	0.31

Table 2: Silicon and yttrium to zirconium ratios as determined by XPS in various atmospheres. If annealed, the annealing time was 10 hours.

In Table 2 the results from the XPS analyses of YSZ single crystals are compiled. From

these data a clear atmosphere, temperature and pressure dependency of silicon enrichment of the YSZ single crystal surface is seen. Silicon was never observed on the surface of YSZ single crystals annealed in UHV nor after annealing in pressures below $1{\cdot}10^{-5}$ mbar of either water vapor or molecular oxygen in the temperature range of 1100 °C to 1250 °C.

The clean YSZ surface after annealing in UHV or pressures below $1{\cdot}10^{-5}$ mbar of either water vapor or molecular oxygen might be explained by two different scenarios. Either silicon does not segregate at low oxygen or water vapor pressures or the silicon in the form of silicon dioxide, silicon monoxide or metallic silicon is desorped continuously, as it segregates to the surface and is subsequently pumped away. The latter hypothesis was tested by both a mass spectrometer and by adsorption of species desorped from the YSZ surface on a gold foil. Using AES analysis of the gold foil placed behind the YSZ crystal while annealed a silicon enrichment of the gold foil was demonstrated as shown in Figure 7. This result suggests that the clean YSZ surfaces observed after annealing in UHV or at low oxygen or water vapor partial pressures is due to desorption of silicon species from the surface YSZ during annealing. The silicon desorption from the YSZ single crystal can follow various routes.

Silicon dioxide can desorp directly from the solid state form into gas phase

$$SiO_2(s) \rightleftharpoons SiO_2(g) \tag{1}$$

however, this reaction is assumed negligible due to low vapor pressure of SiO_2 at 1100 °C [16].

Reduction of silicon dioxide by hydrogen has also been studied according to the reaction

$$H_2 + SiO_2 \rightleftharpoons SiO(g) + H_2O \tag{2}$$

This reaction is endothermic and has a Gibbs free energy of 278.2 kJ/mol at 1100 °C. The rate of reduction of silicon dioxide by hydrogen is considered negligible due to the low total amount of hydrogen under UHV conditions and the positive Gibbs free energy.

Silicon dioxide can also be decomposed directly to silicon monoxide and oxygen

$$SiO_2 \rightleftharpoons SiO(g) + \frac{1}{2}O_2(g) \tag{3}$$

where silicon monoxide is in the gas phase and continuously pumped away in UHV due to the high vapor pressure of $3.2{\cdot}10^{-2}$ mbar at 1100 °C [17]. From thermodynamical calculations the Gibbs free energy of this reaction is calculated to 450.1 kJ/mol at 1100 °C with an equilibrium constant of $7.5{\cdot}10^{-18}$. The equilibrium of silicon dioxide decomposition is dependent on the oxygen partial pressure in the preparation chamber where low oxygen partial pressures shift the equilibrium towards silicon monoxide and molecular oxygen formation. However, in order to account for the silicon dioxide free surfaces observed by XPS the silicon dioxide decomposition rate must be equal to or greater than the segregation rate from the YSZ crystal. The segregation rate or time to reach an equilibrium composition of the surface has not been measured explicitly here but data from Hughes [11] who investigated the segregation rate from YSZ single crystals can instead be used. He found that the silicon surface enrichment equilibrium was reached after 150 min. at 1100 °C where monolayer coverage was reached. A removal rate of silicon dioxide in UHV of 1/9000 monolayer/s is hence required at 1100 °C to account for the clean YSZ surfaces observed after annealing. To calculate the removal rate from the YSZ crystal surface the flux of molecules per surface site surface should be considered. The flux is related to the partial pressure of a given specie by the following relation

$$r = \frac{F}{N_0} = \frac{p_{SiO}}{N_0\sqrt{2\pi \cdot m \cdot k \cdot T}} \tag{4}$$

where r is the rate of desorption (s^{-1}), F is the flux ($s^{-1}{\cdot}m^{-2}$), N_0 is the number of surface sites per square meter (m^{-2}), p_{SiO} is the partial pressure of silicon monoxide (Pa), m is the mass of the silicon monoxide molecule (kg), k is Boltzmann's constant (J/K) and T is temperature (K). The desorption rate is estimated from Hughes [11] as mentioned earlier to 1/9000 monolayer/s. Rearranging the rate equation for the partial pressure of silicon monoxide and insertion of $r = 1/9000$ s^{-1}, $N_0 = 1.5 \cdot 10^{19}$ m^{-2} for a (100) surface, $m = 7.31 \cdot 10^{-26}$ kg, $k = 1.38 \cdot 10^{-23}$ J/K and $T = 1373.15$ K gives a partial pressure of

$$\begin{aligned} p_{SiO} &= \frac{1}{9000} \cdot 1.5 \cdot 10^{19}\sqrt{2\pi \cdot 7.31 \cdot 10^{-26} \cdot 1.38 \cdot 10^{-23} \cdot 1373.15} \\ &= 1.6 \cdot 10^{-7} \text{ Pa} = 1.6 \cdot 10^{-9} \text{ mbar} \end{aligned} \tag{5}$$

From the equilibrium constant the oxygen partial pressure required to obtain this partial

pressure of silicon monoxide can be calculated

$$K = \frac{p_{SiO} \cdot (p_{O_2})^{\frac{1}{2}}}{[SiO_2]} \tag{6}$$

where the equilibrium constant has a value of $7.5{\cdot}10^{-18}$ as stated previously. The partial pressure of oxygen can hence be estimated directly from the equilibrium constant

$$p_{O_2} = \left(\frac{K \cdot [SiO_2]}{p_{SiO}}\right)^2 = \left(\frac{7.5 \cdot 10^{-18} \cdot 1}{1.6 \cdot 10^{-9}}\right)^2 = 2.2 \cdot 10^{-17} \text{ mbar} \tag{7}$$

With a base pressure of $1 \cdot 10^{-9}$ mbar in the chamber the oxygen partial pressure is not expected to be in region of $2.9{\cdot}10^{-17}$ mbar and the equilibrium in (3) would be shifted towards silicon dioxide formation. The decomposition rate of silicon dioxide to silicon monoxide is hence to low to account for the silicon free surfaces observed after annealing in UHV or in low oxygen or water vapor partial pressures. The contribution from thermal decomposition of silicon dioxide is consequently expected to be insignificant in this system.

The decomposition of silicon dioxide to silicon monoxide has previously been reported on silicon wafers in UHV by several authors [18–20]. Ishizaka and Shiraki [20] have shown that a silicon dioxide overlayer on a silicon substrate can be decomposed within 3 minutes at temperatures down to 830 °C. They suggested a reduction of silicon dioxide by metallic silicon to be dominant according to

$$Si(s) + SiO_2(s) \rightarrow 2SiO(g) \tag{8}$$

The reduction of silicon dioxide to silicon monoxide is hence facilitated by the metallic silicon on the surface. Metallic silicon is not present on the surface or in the bulk of YSZ. A reduction scheme of silicon dioxide to metallic silicon would have to occur through the reduction of silicon dioxide to silicon monoxide which would desorp, as discussed earlier, before a complete reduction to metallic silicon would be completed. Metallic silicon is therefore not present to decompose silicon dioxide according to the reaction proposed in (8) in our system.

A faster decomposition rate of silicon dioxide than direct thermal decomposition is responsible for the silicon free surfaces observed after annealing in UHV or in low partial

pressures of oxygen or water vapor. It was observed that the single crystals were, while heated using the a.c. voltage, reduced to a dark brown/black color. This is believed to be due to an electrochemical reduction rather than a thermochemical reduction. During ramping of temperature and hence a.c. voltage across the crystal it was blackened. While annealed the crystal has approximately 10 V_{rms} across it. Despite the high frequency of 18 kHz employed for heating a reduction of the crystal in partial pressures of oxygen below 1 mbar occurs. While oxygen is still present the electrode process is

$$O^{2-} \leftrightharpoons \frac{1}{2}O_2 + 2e^- \tag{9}$$

Oxygen will hence evolve while one electrode is positive, and oxygen is reduced on the other that is negative. At low oxygen partial pressures oxygen cannot be reduced and zirconium oxide or yttrium oxide is partially reduced at one electrode according to

$$ZrO_2 \rightarrow ZrO_{2-\delta} + \frac{\delta}{2}O_2 \tag{10}$$

Half a period later this scenario is reversed and zirconium oxide is reduced at the other electrode creating a reduction zone starting from the two electrodes progressing towards the center of the crystal [21]. In this respect a complete reduction of zirconium oxide to their metallic states can be imagined. However, no observation of such metallic sites have been observed experimentally [21] which agrees with the XPS spectra of blackened crystals without exposure to air which showed oxidized states of zirconium and yttrium. The partial reduction of zirconium and yttrium oxide in the bulk is furthermore supported by the conductivity measurements performed by Park and Blumenthal [22]. At oxygen partial pressures below 10^{-22} mbar and temperatures above 1100 °C the electronic conduction through the crystal will be larger than the ionic conductivity. If reactions continued at the electrodes the zirconium and yttrium oxide would be reduced to metallic zirconium and yttrium which is not the case as discussed earlier. The silicon dioxide is decomposed on the partially reduced zirconium or yttrium oxide which both have large affinities to oxygen. The oxidation of zirconium and yttrium metal is thermodynamically favorable with 840 kJ/mol and 1509 kJ/mol at 1100 °C, respectively. The decomposition of silicon dioxide to silicon

monoxide due to the electrochemical reduction and reaction with vacancies in the YSZ matrix is hence believed to be the main contribution to silicon dioxide decomposition. This thesis is furthermore supported by the experimental observation that the crystal blackens at low partial pressure and silicon dioxide was not observed on surfaces subjected to conditions where the crystal was blackened. To restore the original transparency of the crystal the oxygen or water vapor pressure had to be above 1 mbar. By supplying a reservoir of oxygen or water vapor in the chamber, i.e. raising their partial pressure, the zirconium or yttrium oxide is oxidized to stoichiometry, and at this oxygen potential silicon dioxide is stable. This agrees with the observation of silicon dioxide on the surface when annealing in partial pressures above 25 mbar of oxygen and 10 mbar of water vapor.

A comparable silicon enrichment of the surface was observed after annealing single crystals in lower water vapor pressures and temperature compared to the crystals annealed in oxygen atmospheres. When H_2O and no O_2 is present the H_2O will be reduced to H_2 by the a.c. current. The H_2/H_2O electrode has a higher reaction rate than the oxygen electrode resulting in less reduction of the YSZ crystal surface at lower water vapor partial pressures than oxygen partial pressures. The Si/Zr ratio on the surface after annealing in water vapor or oxygen gas of 100 mbar and 10 mbar, respectively, was lower than the ratio observed after annealing the crystals in air (0.06 and 0.05 compared to 0.22). This can be explained by the high oxygen and water vapor pressure while heating in atmospheric air. In atmospheric air the oxygen partial pressure is 210 mbar assuming a pressure of 1010 mbar and an oxygen content in air of 20.9 %. Similarly, the water vapor pressure in air is approximately 20 mbar, assuming 25 °C, 1010 mbar atmosphere pressure and a relative humidity of 80 %. The combination of high pressure of both oxygen and water compared to the pressures used in this study is therefore believed to be responsible for the differences in the observed ratios.

5. Conclusion

Experiments demonstrate a pressure, temperature and atmosphere dependency of silicon enrichment on yttria-stabilized zirconia surfaces after annealing by an a.c. voltage at temperatures above 1100 °C. After annealing in UHV at 1100 °C and above no silicon en-

richment was observed on the surface. Only at oxygen partial pressures above 25 mbar and at temperatures above 1100 °C silicon was observed on the surface of the crystals. Silicon enrichment of the surface from bulk segregation was observed at lower water vapor pressures (10 mbar) at 1100 °C than oxygen suggesting higher reaction rate of water vapor with YSZ than oxygen. The absence of silicon on the surface of YSZ single crystals annealed in vacuum was explained by the decomposition of silicon dioxide to silicon monoxide on the YSZ surface as demonstrated by AES analysis of a gold foil inserted behind the single crystal while held at elevated temperatures. The YSZ single crystal and the silicon dioxide were electrochemically reduced by an applied a.c. voltage of 10 V_{rms} and 18 kHz at temperatures of 1100 °C and above in UHV.

Acknowledgements

This work was supported financially by The Programme Commission on Sustainable Energy and Environment, The Danish Council for Strategic Research, via the Strategic Electrochemistry Research Center (SERC) (www.serc.dk), contract no. 2104-06-00.

CINF is funded by the Danish National Research Foundation.

References

[1] N. Q. Minh, J. Am. Ceram. Soc. 76 (1993) 563–588.

[2] J. W. Fergus, J. Power Sources 162 (2006) 30–40.

[3] M. Mogensen, J. Høgh, K. V. Hansen, T. Jacobsen, ECS Trans. 7 (2007) 1329–1338.

[4] A. N. Kumar, B. F. Sorensen, J. Am. Ceram. Soc. 83 (2000) 1199–1206.

[5] K. Jensen, S. Primdahl, I. Chorkendorff, M. Mogensen, Solid State Ionics 144 (2001) 197–209.

[6] K. V. Jensen, R. Wallenberg, I. Chorkendorff, M. Mogensen, Solid State Ionics 160 (2003) 27–37.

[7] K. V. Hansen, K. Norrman, M. Mogensen, J. Electrochem. Soc. 151 (2004) A1436–A1444.

[8] J. Høgh, Influence of impurities on the H_2/H_2O/Ni/YSZ electrode, Ph.D. thesis, Risø National Laboratory, 2005.

[9] A. Hauch, S. D. Ebbesen, S. H. Jensen, M. Mogensen, J. Electrochem. Soc. 155 (2008) B1184–B1193.

[10] A. E. Hughes, S. P. S. Badwal, Solid State Ionics 40-1 (1990) 312–315.

[11] A. E. Hughes, J. Am. Ceram. Soc. 78 (1995) 369–378.

[12] A. Bernasik, K. Kowalski, A. Sadowski, J. Phys. Chem. Solids 63 (2002) 233–239.

[13] J. Nowotny, C. Sorrell, T. Bak, Surf. Interface Anal. 37 (2005) 316–324.

[14] K. V. Hansen, K. Norrman, M. Mogensen, Surf. Interface Anal. 38 (2006) 911–916.

[15] M. de Ridder, R. G. van Welzenis, A. W. D. van der Gon, H. H. Brongersma, S. Wulff, W.-F. Chu, W. Weppner, J. Appl. Phys. 92 (2002) 3056–3064.

[16] H. L. Schick, Chem. Rev. 60 (1960) 331–362.

[17] J. A. Nuth, F. T. Ferguson, Astrophysical Journal 649 (2006) 1178–1183.

[18] J. J. Lander, J. Morrison, J. Appl. Phys. 33 (1962) 2089–2092.

[19] J. Tromp, G. Rubloff, P. Balk, F. LeGoues, Phys. Rev. Lett. 55 (1985) 2332–2335.

[20] A. Ishizaka, Y. Shiraki, J. Electrochem. Soc. 133 (1986) 666–671.

[21] J. Janek, C. Korte, Solid State Ionics 116 (1999) 181–195.

[22] J.-H. Park, R. Blumenthal, J. Electrochem. Soc. 136 (1989) 2867–2876.

Strontium zirconate as silicon and aluminium scavenger in yttria stabilized zirconia

Thomas Andersen[a,*], Karin Vels Hansen[b], Ib Chorkendorff[a], Mogens Mogensen[b]

[a] *Center for Individual Nanoparticle Functionality, Department of Physics, Building 312, Technical University of Denmark, DK-2800 Lyngby, Denmark*

[b] *Fuel Cells and Solid State Chemistry Division, Risø National Laboratory for Sustainable Energy, Technical University of Denmark, DK-4000 Roskilde, Denmark*

Abstract

Here we report on strontium zirconate as a getter for silicon dioxide and aluminium oxide in yttria stabilized zirconia (YSZ) single crystals for cleaning purposes. YSZ single crystals were covered with strontium zirconate powder and heat treated at 1450 °C in water vapor. After treatment the YSZ single crystals showed homogeneously distributed ball-sectioned features (bumps) across the external surface of the crystal. The composition as quantified by energy-dispersive X-ray spectroscopy (EDS) showed a large enrichment of silicon and aluminium in the bumps. From cross-section analysis by transmission electron microscopy (TEM) the interface region between bump and YSZ single crystal bulk was examined. EDS showed a homogeneous distribution of silicon and aluminium through the cross section of a bump. The results suggest strontium zirconate as a good getter for silicon and aluminium from bulk materials at elevated temperatures and proves a route to remove trace bulk impurities in YSZ.

Keywords: strontium zirconate, yttria stabilized zirconia, cleaning, impurities

1. Introduction

Control and characterization of extremely clean surfaces are important to gain fundamental understanding of processes on surfaces. All surfaces are under atmospheric conditions covered with impurity adsorbates. These adsorbates are usually mainly water and organic molecules which lowers the surface free energy of the sample. Heating of materials to elevated temperatures can,

*Corresponding author. Center for Individual Nanoparticle Functionality, Department of Physics, Building 312, Technical University of Denmark, DK-2800 Lyngby, Denmark. Tel.: +45 45253137.

Email address: thomas.andersen@fysik.dtu.dk (Thomas Andersen)

however, induce segregation of impurities from the bulk material to the surface. Here we report the cleaning of segregated impurities upon heating in single crystal yttria stabilized zirconia (YSZ).

YSZ has been chosen as starting material due to its versatile technological applications and known segregation of impurities at elevated temperatures [1–4]. This ceramic material have been used for a number of applications, including thermal barrier coating [5], gas sensor [6], as support in heterogeneous catalysis [7] and as electrolyte in solid oxide cells (SOCs) [8, 9].

Segregation of impurities from the YSZ bulk phase to the external surface is especially detrimental for performance of SOCs. Bulk impurities, such as silicon dioxide (silica) and aluminium oxide (alumina) typically found in ppm levels in the cleanest YSZ materials commercially available, have a high tendency to segregate to the external surface of YSZ at SOC operating temperatures. The segregated impurities change the external surface composition and block the triple-phase boundary (TPB) of SOCs [4, 10]. The impurities are believed to be responsible for poor electrode performance in SOCs and has been shown to increase the resistivity of the TPB [4, 10, 11]. Removal of the impurities in YSZ can hence help to gain fundamental understanding of the TPB kinetics and decrease resistivity of the TPB significantly.

From thermodynamic equilibrium segregation calculations it is estimated that a bulk concentration of impurities below 10 ppm in the YSZ bulk is needed to avoid full coverage of impurities of the YSZ surface at elevated temperatures [12]. Presently, no commercial YSZ single crystal or powder is available with this purity and the surface is hence covered with impurities at elevated temperatures.

In this work a surface cleaning method of silica and alumina in YSZ by a getter is investigated.

Silica and alumina that have segregated to the external surface reacts with a getter that is brought into contact with the YSZ surface. The scavenged silica and alumina can after treatment be removed by e.g. polishing of the external crystal surface.

Strontium zirconate has been proposed as getter for silica in YSZ [13]. Calculations of Gibbs free energies of the reaction between silica and strontium zirconate in a wide temperature window (500 - 1500 ^{O}C) suggest the formation of strontium silicate and zirconium oxide (ZrO_2) to be energetically favorable at elevated temperatures.

2. Experimental

YSZ single crystals (9 mol.% Y_2O_3), i.e. $Zr_{0.84}Y_{0.17}O_{1.92}$, was purchased from MTI Corp. Nominal purity is 99.99% excluding hafnium and neodymium and was checked by glow discharge mass spectrometry (GDMS).

Table 1: Concentration of silicon, aluminium and sodium in the as-received crystal and used powder, respectively. Units are ppm by weight.

	Si	Al	Na
YSZ	18	3.5	0.72
$SrZrO_3$	620	57	210

Silicon and aluminium are present in 18 and 3.5 ppm by weight, respectively, as seen in Table 1. The surface roughness of the single crystals are according to specifications typically below 5 Å.

2.1. Heat treatment of samples

Strontium zirconate ($SrZrO_3$) powder purchased from Sigma Aldrich was suspended in ethanol to achieve the most homogeneous coverage before applying the powder to the external surface of crystals. Typically the crystals were covered with 0.01 g strontium zirconate corresponding to a coverage of 0.04 g/cm^2. After application of the suspension to the YSZ single crystals they were placed in a clean dense alumina tube furnace where controlled heating could be applied. All crystals were placed on a 99.99 % pure platinum foil to avoid contamination from the furnace tube. The temperature in the furnace was kept constant at 1450 °C in a water vapor saturated air flow of 3 l/h. Annealing time was varied between 100-440 hours. Heating ramps (up/down) were held constant at 3 °C/min. After heat treatment the samples were removed from the furnace and transported in a plastic beaker for analysis.

Experiments without water vapor at 1450 °C was also conducted. Treatment time for these crystals were 100 hours.

YSZ single crystals with no applied powder were also heat treated in a furnace in dry air at 1100 °C for 10 hours. Temperature and annealing time were chosen such that the surface had reached equilibrium [2]. This was done to investigate the segregation from as-received crystals.

2.2. Characterization of samples

After heat treatment of the single crystals they were characterized by both microscopies for visualizing the surface and by spectroscopies for elemental analysis.

XPS was used to characterize the outermost surface layers of the treated samples. Energy dispersive X-ray spectroscopy (EDS) in combination with a scanning electron microscope (SEM) was used to obtain additional compositional information with high lateral resolution. Transmission electron microscopy (TEM) was used for characterization of YSZ-bump cross section after treatment. Topography information was obtained by atomic force microscopy (AFM). Larger scale overview imaging of the surface was performed by SEM.

XPS spectra were acquired on a PHI Model 550 analyzer with an aluminium magnesium dual anode setup in a UHV chamber with a base pressure of $2{\cdot}10^{-10}$ mbar. The surface was irradiated with non-monochromatized Al K_α X-rays with a primary energy of 1486.6 eV and a constant power of 350 W. Peak identification, fits and concentration calculations were done in casaXPS using the as-implemented Shirley background and sensitivities. All XPS spectra were referred to the adventitious carbon 1s line at 284.6 eV in post processing of the spectra due to charging of the crystal during X-ray exposure.

SEM images were acquired on a FEI Inspect S equipped with a tungsten filament. To avoid charging the crystals were coated with approximately 7 nm carbon.

AFM images were acquired on a Veeco diCaliber Scanning Probe Microscope with a tip diameter of approximately 10 nm. The crystals were adhered to the sample holder by double-sided tape. Images were recorded in tapping mode with a typical scan rate of 20 μm/s.

EDS data were collected by an Oxford Instruments INCAPentaFET-x3 with a typical energy resolution of 100 eV. The excitation voltage was varied between 5 kV and 20 kV.

The sample for cross-section analysis by TEM was prepared by focused ion beam (FIB) cutting on a FEI Quanta 3D FEG. A suitable area consisting of three bumps were located on the sample. The bumps on this area were covered with approximately 50 nm of platinum by Ga^+ assisted deposition to protect the structures. After platinum deposition a thin lamella was cut by Ga^+ ion sputtering and was subsequently transferred in-situ to a Cu-grid. The lamella was thinned down to approximately 50 nm by continuous Ga^+ ion sputtering. From the SEM the sample was transferred in air to a FEI Tecnai T20 TEM from which TEM images were acquired.

3. Results

3.1. Surface composition

After heat treatment of a YSZ single crystal in dry air (1100 °C, 10 hrs.) XPS spectra was acquired. The spectra showed silicon on the surface, as shown in Figure 1, which suggests silicon segregation from the as-received crystal at elevated temperatures as expected.

Prior to treatment with strontium zirconate the surface composition of the as-received single crystals was examined by XPS. No trace of silicon or aluminium was detected on these crystals as seen in Figure 1. The yttrium/zirconium ratio (0.20) was as expected from the doping of the crystal. The only impurities detected were sodium and carbon where carbon was attributed to atmosphere exposure. Sodium was attributed to a low temperature annealing from the manufacturer. Sputtering of the as-received crystal by argon ions verified that carbon and sodium was in the outermost surface layers.

Figure 1 (color online) (Fig1_XPS_strontium_heated_color.tiff)

XPS spectra were measured again directly after removal from the furnace. Ethanol and acetone cleaning were used prior to insertion in the UHV chamber to remove residue powder left on the external surface of the crystal. The powder residue left on the external surface of the YSZ single crystal after heat treatment could, however, not be removed by either ethanol or acetone in a ultrasonic bath and was hence inserted into vacuum with powder residue on the external surface of the single crystal. A large carbon signal was detected in the XPS spectra which was attributed to the exposure to atmosphere and the attempted cleaning by ethanol and acetone. The binding energies of the Zr 3d and Y 3d doublets indicated oxidized states after treatment suggesting little change from the non-heat treated as-received single crystal. The peak areas (after correction by sensitivity factors) of yttrium to zirconium of the heat treated crystal was 0.24 which is higher than the expected ratio (0.20). Peaks from both silicon, aluminium and strontium were also detected as seen in Figure 1. The binding energies of these elements at 102.3 eV, 119.8 eV and 134.1 eV. respectively, suggest oxidized states of these elements.

3.2. Surface topography

A SEM image taken directly after removal of the powder residue by swiping an ethanol soaked cloth across the surface is shown in Figure 2.

Figure 2 (Fig2_YSZ_SrZrO4.tiff)

The external surface of the YSZ single crystal showed regularly distributed ball-sectioned features (bumps) covering 38 % of the total surface area which was calculated from 42 bubbles on a 50x50 μm^2 AFM image. This coverage was verified by analysis of a larger view SEM image, see Figure 2. A mean diameter of 6.90 μm $\pm$ 0.96 μm and a mean height of 0.52 μm $\pm$ 0.05 μm of the observed bubbles was found by analyzing the images.

3.3. Composition of surface bumps

Compositional analysis of the bumps was performed by EDS.

Initial EDS spectra were taken with a 20 kV acceleration voltage to obtain large elemental range. Quantification of the spectra yielded carbon, oxygen, silicon, aluminium, strontium, hafnium, zirconium and yttrium as the only elements in the sample.

Table 2: Compositions determined from EDS with 5 kV excitation voltage. B_x denotes on top of bumps while C_x are areas away from bumps. Units are atomic percent (at.%).

	O	Al	Si	Sr	Y	Zr
B_1	66.5	9.6	11.7	12.2	-	-
B_2	66.3	9.6	11.7	12.3	-	-
C_1	67.9	-	-	-	5.9	26.1
C_2	67.0	-	-	-	6.7	26.3
C_3	67.3	-	-	-	6.7	26.0

After identification of elements with 20 kV the excitation voltage was decreased to 5 kV to decrease the interaction volume of the exciting electrons to approximately $3 \cdot 10^{-3}$ μm^3. This was done to avoid a mixed signal from the bumps and the bulk crystal. Fitting and quantifying the EDS data yields the results shown in Table 2. The EDS data from bumps, B_x shows a large enrichment of silicon, aluminium and strontium compared to areas away from bumps, C_x, where none of these elements could be detected. The high concentration of silicon and aluminium is not observed upon heating a YSZ single crystal without strontium zirconate powder nor are the bumps formed on the surface.

An Y/Zr ratio of 0.24 in bump free areas, C_x, is higher than the ratio from as-received single crystals (0.20). This can be explained by yttria segregation in YSZ single crystals which has been

observed by other authors [14, 15].

3.4. Cross-section analysis of bumps

A lamella from a strontium zirconate treated sample was prepared using FIB. A high angular annular dark field (HAADF) scanning-TEM (STEM) image of a bump on this lamella is shown in Figure 3.

Figure 3 (color online) (Fig3_HAADF_TEM_color.tiff)

The EDS aluminium and silicon line scans showed an enrichment of silicon and aluminium in the bumps compared to the YSZ and showed homogeneity of these elements across the bump.

A clear enrichment of silicon was found compared to the bulk YSZ as shown in Figure 4.

Figure 4 (color online) (Fig4_TEM_EDX_Si_Al_Sr_color.tiff)

No sign of strontium from EDS was found in the bulk crystal suggesting a very low solubility of strontium in YSZ at the applied conditions.

3.5. Annealing time and temperature

The formation of bumps did not change with annealing time for samples treated at 100-400 hours at 1450 °C, respectively. At both 100 hours and 400 hours treatment time the same size distribution and composition was found on treated samples.

Figure 5 (Fig5_SrZrO3_YSZ_1450C.tiff)

YSZ single crystals heat treated with strontium zirconate without water vapor at 1450 °C did also show the characteristic bumps on the surface. However, the homogeneity of these was not as evident as crystals heat treated in air containing water vapor as shown in Figure 5. The water vapor hence increases the mobility of species at elevated temperatures.

4. Discussion

Small amounts of hafnium were detected by EDS (not shown in Table 1) in areas away from bumps, C_x. This is most likely due to the hafnium contamination (0.13 wt.% determined by GDMS) in the bulk of the as-received single crystal. Hafnium, however, being a typical impurity

in YSZ due to the large chemical resemblance with zirconium does typically not segregate to the external surface of YSZ [16, 17]. The hafnium signal is hence expected to originate from the bulk of the single crystal and not as a result of surface enrichment.

The bumps formed on the surface are homogeneously distributed and has a narrow size distribution. This is believed to be a property of the YSZ surface and powder interaction at elevated temperatures and not an intrinsic property of the size distribution of the strontium zirconate powder. The powder has a wide size distribution ranging from the nanometer range up to a quoted maximum diameter of 10 μm. The diameter found both from AFM and SEM images of approximately 6 μm is hence believed to be a result of surface energy equilibria. A strontium zirconate grain on the surface will react with the segregated silicon and/or aluminium and form a stable phase. This grain will then act as a nucleation point for further growth and give conjoining grains and thus a solid structure, which will wet the YSZ surface resulting in the bumps observed on the surface.

According to the phase diagram of the SrO, SiO_2 and Al_2O_3 phases [18] a strontium feldspar ($SrAl_2Si_2O_2$) phase can be formed at temperatures above 1400 °C. Both the silicon and aluminum recorded from on-top EDS spectra agrees with this phase as the ratio of these components are close to 1:1. The strontium and oxygen content (∼12 at.% and ∼66.5 at.%, respectively) in the bumps are, however, higher than expected from the strontium feldspar phase. The excess of oxygen and strontium could be a result of a strontium zirconate surplus compared to the total amount of silica and alumina in the YSZ single crystal. Once all silica and alumina have segregated from the bulk and the crystal is clean the strontium zirconate powder surface is expected to be stable and hence result in a strontium enrichment of the bumps.

To compare the amount of silicon and aluminium detected in the bumps by EDS to the silicon and aluminium content in the bulk as-received YSZ single crystal a mass balance calculation is necessary.

The density of the YSZ single crystal is calculated from the lattice parameters found from X-ray diffraction (XRD). The lattice parameter of 9 mol% fully stabilized YSZ with a cubic unit cell is 5.15187 Å. The density of the crystal can then be calculated from [19]

$$\rho = \left[\left(\frac{A_{Zr} + 2A_O}{100 + \sum M_k(P_k - 1)}\right) + \left(\frac{\sum P_k M_k + (\Delta A_k + [(P_{Ok}/P_k) - 2]\, A_O)}{100 + \sum M_k(P_k - 1)}\right)\right] \left(\frac{Z}{10^{-24} N d_0^3}\right) \quad (1)$$

which accounts for vacancies introduced in ZrO_2 by the addition of yttria. In the case of the binary

zirconia-yttria system direct insertion of the atomic weight of zirconium (91.22), A_{Zr}, the atomic weight of oxygen (15.9994), A_O, and the difference between the atomic weight of yttrium (88.905) and of zirconium, ΔA_k, Avogadro's constant ($6.02 \cdot 10^{23}$), N, the number of atoms pr. unit cell (4), Z, the number of metal ions per molecule of yttria (2), P_k, the number of oxygen ions per molecule of yttria (3), P_{Ok}, the amount of yttria in zirconia (9 mol%), M, and the lattice constant of the YSZ crystal found from XRD (5.15187 Å), d_0, the density of the YSZ single crystal is calculated to 5.91 g/cm^3. The amount of silicon and aluminium in the YSZ single crystal can hence be calculated directly using Table 1 and the dimensions of the single crystal (5 x 5 x 2 mm^3).

$$m_{Si,YSZ} = \rho_{YSZ} \cdot V_{YSZ} \cdot \gamma_{Si,YSZ} = 5.3 \cdot 10^{-6} \text{ g} \tag{2}$$

where $\gamma_{Si,YSZ}$ is the impurity content determined from GDMS (Table 1). The aluminium content in the bulk is determined similarly to the approach in Equation 2 and is calculated to $1.03 \cdot 10^{-6}$ g. These numbers should be compared with the amount of silicon and aluminium found in the bumps on the external surface of the YSZ single crystal after treatment.

The mean volume of a bump on the surface can be calculated by

$$V = \frac{\pi}{6} h_{mean} \left(3a_{mean}^2 + h_{mean}^2\right) \tag{3}$$

where h_{mean} is the height of the bump and a_{mean} is the radius. From AFM images of the YSZ surface after treatment the mean diameter (6.90 μm) and height (0.52 μm) of the bumps was extracted. Insertion into Equation 3 gives a mean bump volume of $9.80 \cdot 10^{-12}$ cm^3. Assuming a homogeneous distribution (cf. Figure 2) of bubbles and a coverage of 38% as found from SEM images the number of bumps on the surface can be calculated

$$N_{bumps} = \frac{A_{YSZ}}{\pi r_{bump}^2} \cdot \theta \tag{4}$$

where the bumps are assumed spherical and θ is the coverage. By insertion of the YSZ surface area, A_{YSZ} = 5 x 5 mm^2, and the mean bump radius of 6.90 μm the number of bumps on the surface is calculated to $2.5 \cdot 10^5$. The total volume of bumps of the surface can hence be determined as

$$V_{total} = V_{bump} \cdot N_{bumps} = 2.5 \cdot 10^{-6} \text{ cm}^3 \tag{5}$$

Assuming the bumps are strontium aluminosilicate ($SrAl_2Si_2O_8$), which is the most likely phase according to the phase diagram, the density of the bumps is 3.04 g/cm^3. The total mass of bumps

on the surface is hence given as

$$m_{bumps} = V_{total} \cdot \rho_{SrAl_2Si_2O_8} = 7.6 \cdot 10^{-6} \text{ g} \quad (6)$$

The total amount of silicon in the bumps is calculated similarly to Equation 2

$$m_{Si,bumps} = m_{bumps} \cdot \gamma_{Si,bumps} = 8.9 \cdot 10^{-7} \text{ g} \quad (7)$$

Similarly, the amount of aluminium in the bubbles is calculated to $7.2 \cdot 10^{-7}$ g.

Comparing the amount of silicon in the bulk crystal before treatment, Equation 2, with Equation 7 the amount of silicon and aluminium in the bumps on the surface is lower than the amount of silicon and aluminium found in the single YSZ crystal. To obtain crystals free of silicon and aluminium several subsequent treatments may hence prove necessary.

To minimize the number of cleaning cycles and treatment time the thickness of the crystal is important. Shortening the segregation distance of impurities from the bulk to the external surface of the crystal by decreasing the thickness decreases both treatment time and the number of treatments required.

The bumps on the surface must consist of silicon and aluminium segregated from the bulk crystal as the external surface of the YSZ single crystal is the only interface where silicon or aluminium is in contact with the applied strontium zirconate powder. If the silicon originates from the powder (where it is bound as strontium silicate since this is thermodynamically more stable than strontium zirconate) a very different (and much less homogeneous) height distribution of the bumps would be expected as illustrated by the SEM image of the heated strontium zirconate powder in Figure 6.

Figure 5 (Fig6_SrZrO3_1450C.tiff)

No trace of either silicon or aluminium was detected by EDS in areas away from bumps. This may either be due to the low surface sensitivity of EDS or that the crystal is clean of silicon and aluminium. If all the impurities from the YSZ bulk have not reacted with strontium zirconate these areas on the YSZ single crystal will most probably be covered by a monolayer of a glassy impurity phase [20, 21].

TEM was also used to study the interface region between bumps and bulk YSZ. No trace of strontium was found from the cross-section analysis of the YSZ single crystal suggesting very low

solubility of strontium in YSZ under these experimental conditions which is in agreement with other experimental data [22]. Figure 3 furthermore supports that the bumps are confined to the external surface of the YSZ crystal. The contrast in the HAADF TEM image indicates two separate phases which was also confirmed by the EDS analysis. The EDS data taken across one bump suggested homogeneity of silicon, aluminium and strontium. The apparent increased level of silicon and aluminium in the crystal (from .55 μm and above in Figure 4) is not attributed to an increased level of silicon and aluminium near the the bump/single crystal interface. The apparent increased levels are attributed to the overlap of the Si_K and Al_K EDS lines with the Zr_K and Y_K EDS lines in the YSZ single crystal bulk region.

The addition of water vapor to the heat treatment ensures larger mobility of reaction species. This is concluded from the larger homogeneity of bumps upon addition of water vapor compared to dry air experiments as shown in Figure 5.

5. Conclusion

Experiments demonstrate the use of strontium zirconate to scavenge silica and alumina segregated from a bulk YSZ single crystal. Upon heat treatment at 1450 °C and application of a strontium zirconate suspension to the external surface of a single crystal YSZ surface ball-sectioned features (bumps) with a high content (9–12 at.%) of silicon and aluminium were formed. These structures were confined to the external surface of the single crystal as verified by SEM and TEM in combination with EDS. The results suggest strontium zirconate as a scavenger for typical segregating trace bulk impurities (silica and alumina) in YSZ at elevated temperatures and may be used to obtain YSZ crystals free of silicon and aluminium.

Acknowledgements

This work was supported financially by The Programme Commission on Sustainable Energy and Environment, The Danish Council for Strategic Research, via the Strategic Electrochemistry Research Center (SERC) (www.serc.dk), contract no. 2104-06-0011.

CINF is funded by the Danish National Research Foundation.

References

[1] A. Bernasik, K. Kowalski, A. Sadowski, J. Phys. Chem. Solids 63 (2002) 233–239.

[2] A. E. Hughes, J. Am. Ceram. Soc. 78 (1995) 369–378.
[3] A. E. Hughes, S. P. S. Badwal, Solid State Ionics 40-1 (1990) 312–315.
[4] K. Jensen, R. Wallenberg, I. Chorkendorff, M. Mogensen, Solid State Ionics 160 (2003) 27–37.
[5] N. P. Padture, M. Gell, E. H. Jordan, Science 296 (2002) 280–284.
[6] Z. Y. Can, H. Narita, J. Mizusaki, H. Tagawa, Solid State Ionics 79 (1995) 344–348.
[7] P. Panagiotopoulou, D. I. Kondarides, Catal. Today 112 (2006) 49–52.
[8] N. Q. Minh, J. Am. Ceram. Soc. 76 (1993) 563–588.
[9] J. W. Fergus, J. Power Sources 162 (2006) 30–40.
[10] K. V. Jensen, R. Wallenberg, I. Chorkendorff, M. Mogensen, Solid State Ionics 160 (2003) 27–37.
[11] A. Hauch, S. D. Ebbesen, S. H. Jensen, M. Mogensen, J. Electrochem. Soc. 155 (2008) B1184–B1193.
[12] M. de Ridder, A. G. J. Vervoort, R. G. van Welzenis, H. H. Brongersma, Solid State Ionics 156 (2003) 255–262.
[13] P. Larsen, M. Mogensen, P. Henriksen, S. Linderoth, M. Chen, International patent WO 2009/027100 A1, 2009.
[14] A. Hughes, X-ray photoelectron spectroscopy study of segregation phenomena in yttria-zirconia solid electrolytes, Ph.D. thesis, Royal Melbourne Institute of Technology, Australia, 1990.
[15] M. de Ridder, R. van Welzenis, H. Brongersma, U. Kreissig, Solid State Ionics 158 (2003) 67–77.
[16] K. V. Hansen, K. Norrman, M. Mogensen, Surf. Interface Anal. 38 (2006) 911–916.
[17] M. de Ridder, R. G. van Welzenis, A. W. D. van der Gon, H. H. Brongersma, S. Wulff, W.-F. Chu, W. Weppner, J. Appl. Phys. 92 (2002) 3056–3064.
[18] G. Beall, J. Eur. Ceram. Soc. 29 (2009) 1211–1219.
[19] R. Ingel, D. Lewis III, J. Am. Chem. Soc. 69 (1986) 325–332.
[20] K. V. Jensen, The Ni-YSZ interface (Structure, composition and electrochemical properties at 1000 °C), Ph.D. thesis, Risø National Laboratory, Roskilde, Denmark, 2002.
[21] J. Nowotny, C. Sorrell, T. Bak, Surf. Interface Anal. 37 (2005) 316–324.
[22] J.-P. Zhang, S.-P. Jiang, J. G. Love, K. Foger, S. P. S. Badwal, J. Mater. Chem. 8 (1998) 2787–2794.

List of Tables

List of Figures

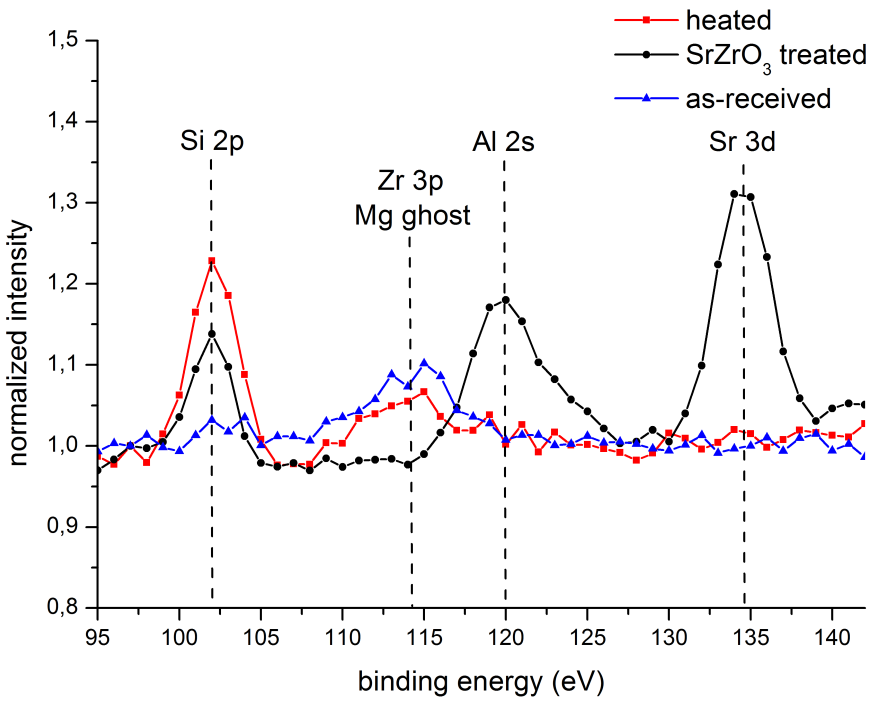

Figure 1: XPS spectra comparing an YSZ single crystal heated in a furnace to a $SrZrO_3$ treated crystal. A clear enrichment of both aluminium and strontium is seen on the surface compared to as-received crystals.

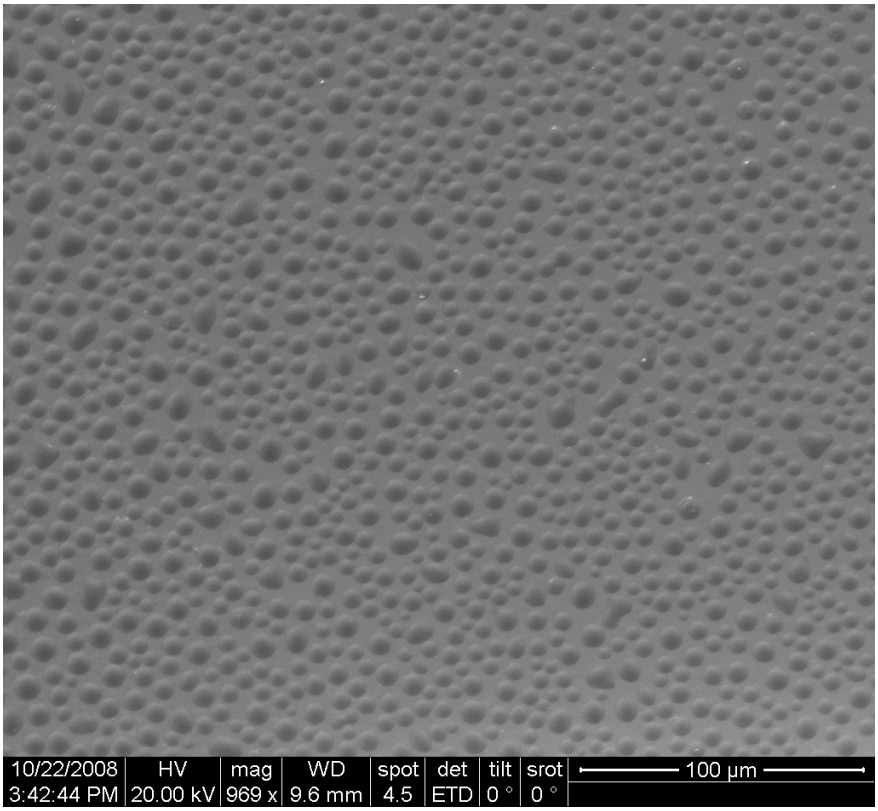

Figure 2: Low magnification SEM image acquired by secondary electrons showing bumps over a large area. The bumps are homogeneous in both size and height and covers 38 % of the total surface area.

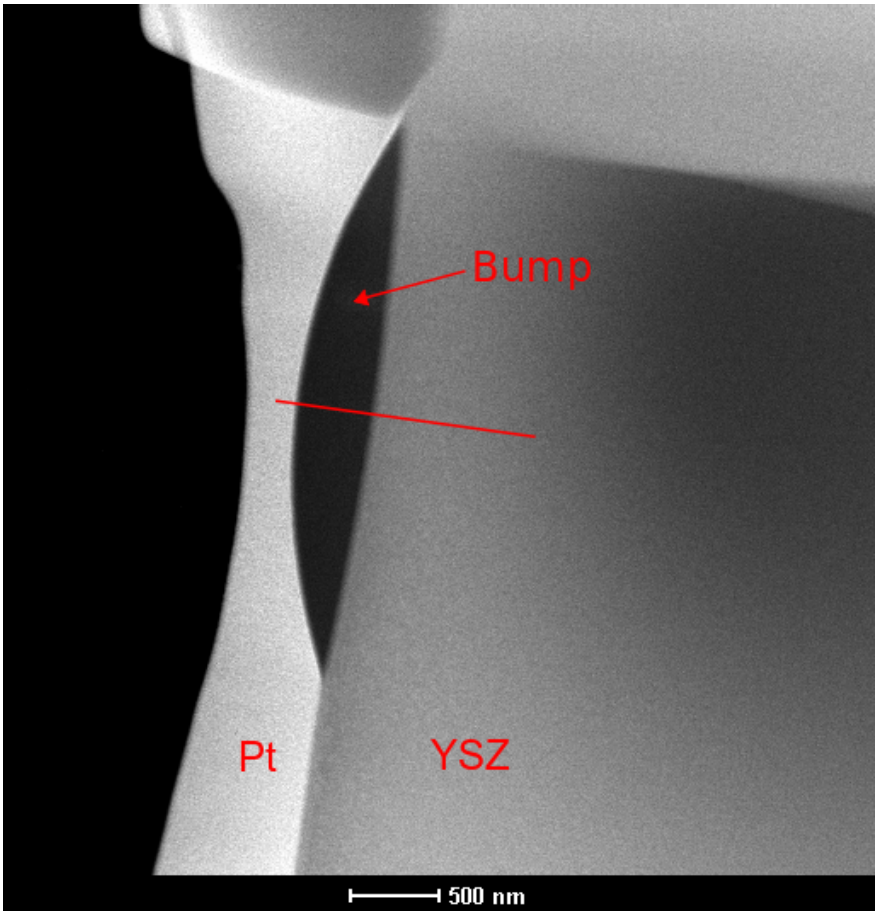

Figure 3: HAADF TEM image showing one of the bumps. On the left side the platinum overlayer is seen. The red line indicates the line profile used for EDS.

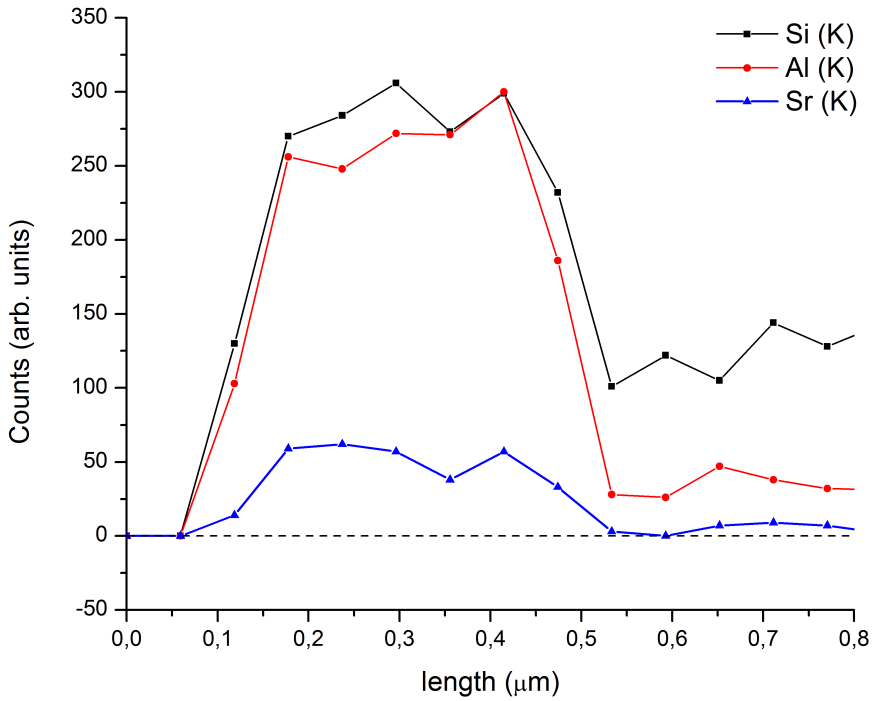

Figure 4: The silicon, aluminium and strontium profile recorded by EDS across a single bump. The line profile is shown in Figure 3.

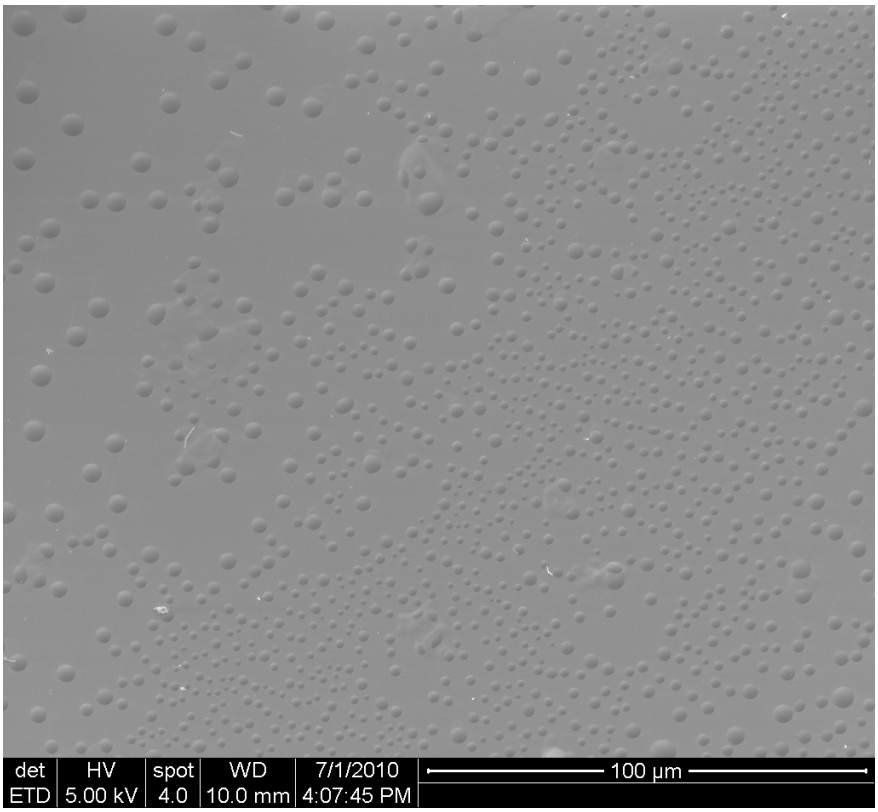

Figure 5: Low magnification SEM image acquired by secondary electrons after treatment with $SrZrO_3$ in dry air. The bumps are much less homogeneous in size and distribution compared to crystals treated in water vapor, cf. Figure 2.

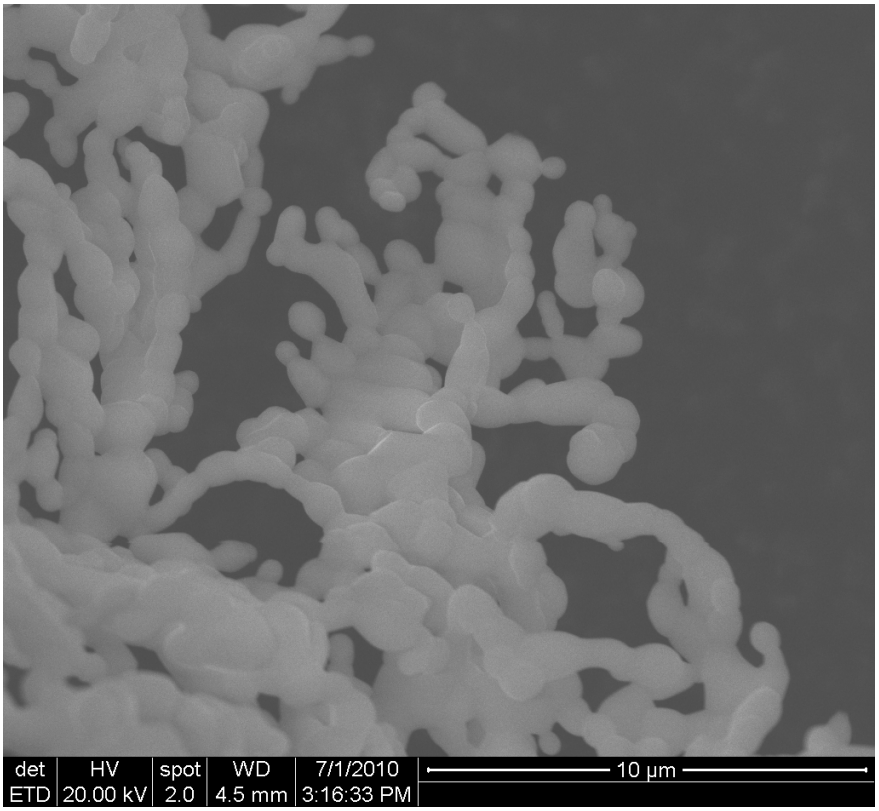

Figure 6: SEM image of heat treated $SrZrO_3$ powder at 1450 °C for 100 hours in water vapor.